



Title	Plasmon-induced photoelectrochemical biosensors using gold nanostructured titanium dioxide photoelectrodes
Author(s)	郭, 景春
Citation	北海道大学. 博士(情報科学) 甲第12943号
Issue Date	2017-12-25
DOI	10.14943/doctoral.k12943
Doc URL	http://hdl.handle.net/2115/68112
Type	theses (doctoral)
File Information	Guo_Jingchun.pdf



[Instructions for use](#)

Plasmon-Induced Photoelectrochemical Biosensors Using Gold
Nanostructured Titanium Dioxide Photoelectrodes

Thesis by

Jingchun Guo

In Partial Fulfillment of the Requirements

for the Degree of

Doctor of Philosophy



DIVISION OF BIOENGINEERING AND BIOINFORMATICS

GRADUATE SCHOOL OF INFORMATION SCIENCE AND

TECHNOLOGY

HOKKAIDO UNIVERSITY

SAPPORO, JAPAN

2017

Dedication

This PhD thesis is dedicated to beloved my family, for their
unwavering faith in my ability to not screw up

Table of Contents

Thesis Abstract	iv
Chapter 1.....	1
Introduction	1
1.1 Background of localized surface plasmon resonance biosensor	1
1.2 Optical properties of localized surface plasmon resonance	11
1.2.1 Far-field spectral properties.....	14
1.2.1.1 Individual metallic nanoparticles	15
1.2.1.2 Coupled plasmonic systems	16
1.2.2 Near-field spectral properties	23
1.2.2.1 Scanning near-field optical microscopy	23
1.2.2.2 Cathodoluminescence and electron energy-loss spectroscopy.....	24
1.2.2.3 Photoemission electron microscopy	25
1.3 Plasmonic photoelectrochemical biosensors	26
1.4 Aim and outline of this thesis.....	30
1.5 References	31
Chapter 2.....	45
Near-field spectrum measurement of strongly coupled waveguide-plasmon modes by photoelectrochemistry	45
2.1 Introduction	45
2.2 Experimental details	57
2.2.1 Preparation of periodic gold nanogratings patterned titanium dioxide photoelectrode	57
2.2.2 Photoelectrochemical measurements.....	58
2.3 Results and discussions	59
2.3.1 Structural geometries of periodic gold nanogratings patterned titanium dioxide photoelectrode	59

2.3.2 Experimental extinction properties of periodic gold nanogratings patterned titanium dioxide photoelectrode	60
2.3.3 Finite-difference time-domain simulation results	61
2.3.4 Experimental and calculated hybrid dispersion curves	66
2.3.5 Near-field and internal quantum efficiency spectra of periodic gold nanogratings patterned titanium dioxide photoelectrode	67
2.4 Conclusions	73
2.5 References	74
Chapter 3.....	89
<i>In situ</i> real-time measurement of biotin-streptavidin binding kinetics by photoelectrochemistry	89
3.1 Introduction	89
3.2 Experimental details	90
3.2.1 Gold film preparation and modifications	90
3.2.2 Preparation of gold nanoislands decorated titanium dioxide photoelectrode and biomodifications	91
3.2.3 Photoelectrochemical measurements.....	93
3.3 Results and discussions	93
3.3.1 Nonspecific adsorptions	93
3.3.2 Structural geometries of gold nanoislands decorated titanium dioxide photoelectrode	95
3.3.3 Optical properties of gold nanoislands decorated titanium dioxide photoelectrode and streptavidin-modified gold nanoparticles	95
3.3.4 Verification of the plasmon-induced photocurrent generation.....	96
3.3.5 Optical and photoelectrochemical measurements before and after biomolecular modifications.....	97
3.3.5.1 Streptavidin modification	97
3.3.5.2 Streptavidin-modified gold nanoparticles modification.....	98

3.3.6 <i>In situ</i> real-time measurement of streptavidin-modified gold nanoparticles	99
3.3.7 Proposed mechanism	100
3.3.8 Binding kinetics analysis	103
3.3.9 Interparticle coupling and near-field enhancement	106
3.4 Conclusions	109
3.5 References	110
Chapter 4.....	112
Summary and Future Perspectives	112
4.1 Summary	112
4.2 Future Perspectives.....	113
Acknowledgements	115
List of Publications.....	117

Thesis Abstract

Metallic nanoparticles (NPs) such as gold (Au) and silver exhibit very intense color which is derived from localized surface plasmon resonances (LSPRs). LSPRs are collective oscillations of conduction electrons, which induce large local electromagnetic (EM) field enhancements. EM field enhancement effects are known to induce various optical effects such as surface-enhanced Raman scattering (SERS) and fluorescence enhancement which make it possible to detect small number of molecules. Therefore, SERS and fluorescence enhancement have been applied to highly sensitive biosensors. As the other biosensor using the principle of LSPRs, there is a method which detect a small spectrum shift due to the refractive index change of surrounding medium based on the adsorption of bioanalytes to the surface of AuNPs, which is known as a LSPR biosensor. Although SERS is extremely sensitive and LSPR biosensor is simple, they require relatively large equipment such as laser and spectrometer, and development of small and compact sensor is also demanded. On the basis of the background of biosensors using a principle of LSPRs, a photoelectrochemical (PEC) biosensor in which electronic circuits and detectors can be integrated is proposed in this study by using Au nanostructured titanium dioxide (TiO_2) photoelectrodes. Because the PEC biosensor studied previously relies on the spectrum change of LSPRs based on the refractive index change of surrounding medium, the sensitivity is not expected as similar to LSPR biosensor. In the present study, I proposed the improvement of sensitivity on the PEC biosensor based on the EM field enhancement due to near-field coupling between Au nanostructures on TiO_2 and AuNPs by connecting using an antigen-antibody reaction of biotin and streptavidin.

To elucidate the influence of near-field coupling between LSPR of Au nanostructures on TiO_2 photoelectrode and the other optical modes on the PEC responses, I explored the internal quantum efficiency (IQE) of plasmon-induced photocurrent generations as a function of incident wavelength. Namely, the near-field coupling between LSPR and the other optical modes reflects the PEC response if the IQE spectrum reproduces the

near-field spectrum. On the basis of the hypothesis, I employed TiO₂ photoelectrodes supporting Au nanogratings (AuNGs) because AuNGs/TiO₂ substrate shows complicated near-field spectra due to the strong coupling between waveguide modes induced by AuNGs and LSPR of AuNGs for the demonstration of performance. Periodic AuNGs were fabricated on TiO₂ photoelectrodes using electron beam lithography and lift-off processes. Plasmon-induced photocurrent generation was pursued by a conventional PEC measurement using a three-electrode system. It was clearly elucidated that IQE spectrum has successfully reproduced the near-field spectrum predicted by EM simulations based on the finite-difference time-domain (FDTD) method under the coupling conditions. This paves a new approach to indirectly measure the near-field spectra of coupled plasmonic systems and proves that the near-field coupling reflects the plasmon-induced photocurrent generation. (Chapter 2).

The photocurrent enhancement by the near-field coupling was studied as a sensitive biosensor for measuring the biotin-streptavidin binding kinetics. In this study, Au nanoislands (AuNIs) loaded single crystal TiO₂ substrate was used as a photoelectrode. The photoelectrode was then processed by self-assembled thiol-terminated biotin (TTB) molecules. The self-assembled TTB molecules bound on an AuNIs/TiO₂ photoelectrode successfully detected different concentrations of streptavidin-modified AuNPs solutions based on the PEC measurement owing to the near-field coupling between AuNIs and AuNPs with biomolecules. Furthermore, the real-time monitoring of biotin-streptavidin binding affinities and kinetics by analyzing the PEC sensing characteristics has been also successfully demonstrated. This PEC biosensor could provide a new approach for the specific electrical detection and real-time kinetic measurements for clinical diagnostics and drug development (Chapter 3).

In conclusion, the plasmon-induced photocurrent generation was proved as a useful tool for detecting the biomolecular binding affinity and kinetics. It was clearly confirmed that the near-field coupling between LSPR and the other optical modes reflects the PEC response, which can be utilized for the highly sensitive detection of bioanalytes. The biosensor for pursuing biotin-streptavidin binding kinetics based on

the plasmon-induced photocurrent generation have been successfully improved by the near-field coupling between AuNIs and biomodified AuNPs. These findings provide a powerful tool to detect and determine the binding affinity and kinetics of biomolecular interactions as a compact plasmonic PEC biosensor.

Keywords: Localized surface plasmon resonance, Photoelectrochemical biosensing, Titanium dioxide, Au nanoislands, Au nanogratings, Near-field coupling, Strongly coupled waveguide-plasmon modes, Biotin-streptavidin association, Binding kinetics.

Chapter 1

Introduction

1.1 Background of localized surface plasmon resonance biosensor

What is a biosensor? “Biosensor” is short for “biological sensor.” A biosensor is an analytical device incorporating a biological sensing element either intimately connected to or integrated within a transducer.^[1,2] Biosensor can be traced back to 1962, Clark, L. C. and Lyons, C. invented the first enzyme electrode based on glucose oxidase (GOD) for detecting dissolved oxygen by amperometric method.^[3] While Updike, S.J. and Hicks, G.P. improved the enzyme transducer by immobilizing enzyme GOD over the oxygen electrode to achieve a more effective strategy.^[4] The biosensor market has been increasing year by year and incoming large industry of more than 15 billion USD in 2016 as shown in Figure 1.1.

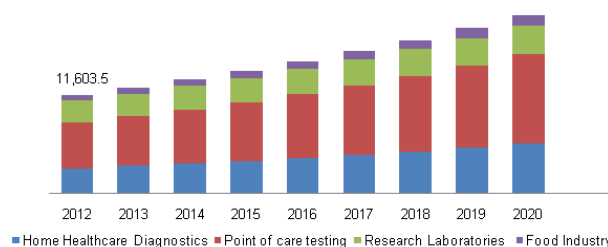


Figure 1.1 Global biosensor market (USD Million).

<http://www.grandviewresearch.com/industry-analysis/biosensors-market>.

Until now, there are many different kinds of biosensors that have been utilized in different fields. Among all kinds of biosensors, surface plasmon resonance (SPR) sensors are extensively developed in recent years and have been realized for commercialized production (e.g. Biacore SPR Systems, GE Healthcare Life Sciences). Three types of most commonly used SPR biosensors are shown in Figure 1.2.^[5,6] The SPR biosensors have extremely high bulk dielectric sensitivity, therefore, they can

detect minor signal change induced by biomolecular interactions at very low concentrations. In addition, the SPR biosensor allows real time quantitative analysis of specific binding kinetics and affinities without labels and the requirements of removing spurious signals due to non-specific binding. However, several drawbacks also limit the applications of SPR biosensor including temperature-sensitive, high-throughput analyses, complex and high cost instrumentations and so on.

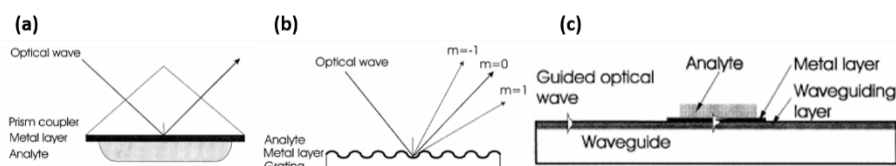


Figure 1.2 Most widely used three types of SPR sensors: (a) prism coupler-based SPR system (attenuated total reflectance (ATR) method); (b) grating coupler-based SPR system; (c) optical waveguide-based SPR system.^[5]

When light is incident on sub-wavelength-sized metallic nanoparticles, the excited collective oscillations of conduction electrons in the metallic nanoparticles form localized SPR (LSPR).^[7-10] To date, the LSPR has been extensively applied in many fields especially in Surface-enhanced Raman scattering (SERS) and biosensing. Jeanmaire and Van Duyne demonstrated that the Raman scattering signal can be greatly enhanced when the molecule is placed on or near a roughened noble-metal substrate in 1977.^[11] SERS is an ultrasensitive technique to detect molecules on or near the surface of metallic nanostructures. To date, the correct nature of the huge enhancement in Raman intensity found in the SERS is still controversial even though a great deal of researches have been carried out. However, near-field enhancement and electron transfer are generally accepted to explain the mechanism of SERS enhancement. The near-field enhancement is based on the electric field enhancement provided by the metallic film or nanoparticles. However, the near-field enhancement sometimes cannot fully explain the magnitude of the enhancement observed in many systems. The electron transfer, a different enhancement mechanism can explain the

enhancement involving charge transfer between the chemisorbed species and the metal surface. Now, most researchers believe that the total SERS enhancement is the cooperation of both these two enhancement mechanisms. It has been twenty years ago, single-molecule detection was successfully realized due to the Raman scattering intensity can be enhanced up to 10^{14} to 10^{15} fold for molecules adsorbed on the surfaces of noble metal.^[12-14] This brings extensive applications of SERS such as, corrosion, catalysis, advanced materials, diagnostics, biomedical applications, biological process, and biosensing. The SERS can be used to investigate antibiotic-induced chemical changes in bacterial cell wall, rapid detection of bacteria, target specific DNA and RNA sequences, pathogen detection, detection of arsenate and arsenite ions in aqueous solutions, glucose detection in human blood and so on. The SERS based biosensors have extremely high sensitivity but the SERS signal is highly dependent on the distance between molecule and metallic nanoparticles. Quantitative measurement is a challenge.

There is another conventional optical LSPR biosensor based on the measurement of LSPR peak shifts.^[15-20] How LSPR can be utilized as biosensor? Just like the propagating SPPs, the LSPR is also sensitive to the surrounding refractive index (RI) change. The relationship between LSPR peak wavelength of a spherical particle and the surrounding RI has been calculated by Mie theory^[19]:

$$\lambda_{\max} = \lambda_p \sqrt{2n_m^2 + 1} \quad (1.1)$$

where λ_{\max} and λ_p are the wavelengths of maximum LSPR peak and plasma frequency of the bulk metal, respectively. n_m is the RI of surrounding medium. It is easy to verify that the LSPR peak ought to have linear red shift with increase of RI of surrounding medium as shown in Figure 1.3 based on Equation 1.1 with $\lambda_p = 300$ nm over a reasonable range of n_m . Note that both of the LSPR peak and energy have approximately linear relationships with surrounding RI change.

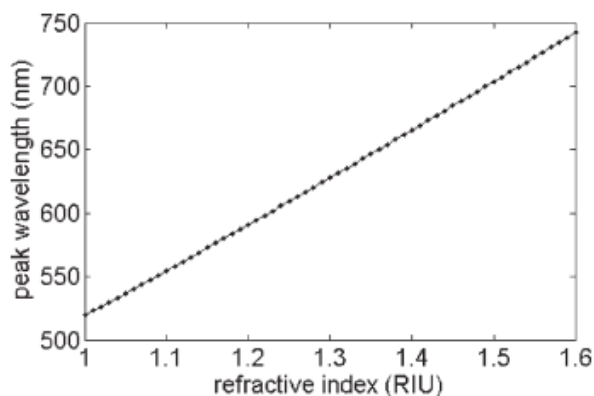


Figure 1.3 A theoretical results between the LSPR peak and the surrounding RI.^[19]

LSPR biosensors are commonly utilized to detect biomolecular interactions through an optical response, such as LSPR spectral peak shifts^[21,22] or change in extinction values.^[23,24] Like the SPR biosensor, the immobilized receptors on the metal nanoparticles that exhibit LSPR is necessary to be used to detect the specific biomolecular interactions. Until now, lots of molecular interactions have been realized by utilizing LSPR biosensor. Biotin-streptavidin interaction has extremely strong binding affinity ($K_a \sim 10^{13} \text{ M}^{-1}$). Biotin, a kind of vitamin with small molecular weight, can be easily conjugated to the metallic nanostructures. Streptavidin, a kind of protein with extremely large molecular weight of about 53000, has four subunits for binding biotin, generating one of the strongest non-covalent interactions known in nature. This strong interaction leads to not only biosensing but also lots of other research applications such as immunological and diagnostic applications. The biotin-streptavidin interaction has been successfully utilized to realize LSPR sensor.^[21,23,25-33] Figure 1.4 (1) shows a representative LSPR peak shift of a biotin-functionalized triangular silver nanostructure biosensor to different concentrations of streptavidin solutions. The triangular silver nanoparticles were fabricated by nanosphere lithography and then a subsequent 24 h biotinylation was processed totally. These biotinylated triangular nanoparticles were used to detect the signal change to different concentrations of streptavidin solutions. Moreover, the surface-confined thermodynamic affinity constant of biotin-streptavidin interaction can be estimated by Langmuir isotherm with a value

$K_{a, \text{surf}} = 10^{11} \text{ M}^{-1}$. The low limit of detection (LOD) can reach 1 pM. While the LSPR based biotin-streptavidin biosensors have much smaller binding affinity values in comparison with the solution-based binding affinity constant (normally $K_a = 10^{14} - 10^{15} \text{ M}^{-1}$) due to the restricted movement of biotin molecules on the sensor surface reduces the affinity for binding to streptavidin.^[27] The steric hindrance that the bottom attached biotin binding sites are retarded by the top attached biotin binding sites.

One advantage of the SPR biosensor is the real time measurement and detection of the molecular interactions. The LSPR biosensor can also realize the real time measurement and detection of the molecular interactions as shown in Figure 1.4 (2). A biotinfunctionalized gold colloid monolayer is used to bind streptavidin and anti-biotin mAb, respectively. The absorbance intensity was detected real time at LSPR peak. Both of 10 $\mu\text{g/mL}$ streptavidin and 50 $\mu\text{g/mL}$ anti-biotin mAb showed the binding rising phase due to the specific interactions. However, 10 $\mu\text{g/mL}$ Bovine Serum Albumin, 50 $\mu\text{g/mL}$ human immunoglobulin G, or streptavidin (30 $\mu\text{g/mL}$) preincubated with 1.0 mM biotin did not show such binding rising phase due to nonspecific interactions. After the bindings reaching saturations, incubation of the protein-ligand complex on the surface with 1 mM biotin in solution will cause decrease in signal due to dissociation of biotin-mAb complex. However, there was no obvious change in the case of biotin-streptavidin associations. This is due to the much stronger binding affinity of biotin-streptavidin than the biotin-anti-biotin interaction.

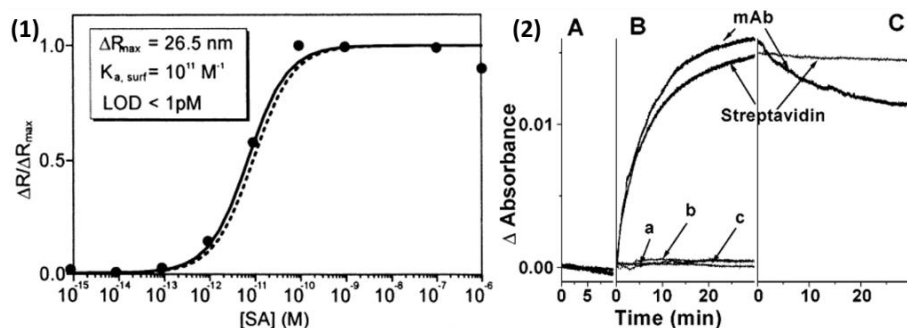


Figure 1.4 (1) The normalized LSPR shift response to different concentrations of streptavidin of a biotin-functionalized Ag nanotriangles biosensor (SA means

streptavidin).^[21] (2) The absorbance intensity change at LSPR peak wavelength when using biotinfunctionalized gold colloid monolayer to bind streptavidin and anti-biotin mAb (A) Baseline (B) Incubation of the streptavidin (10 $\mu\text{g/mL}$), anti-biotin mAb (50 $\mu\text{g/mL}$), Bovine Serum Albumin (10 $\mu\text{g/mL}$) (a), human immunoglobulin G (50 $\mu\text{g/mL}$) (b), or streptavidin (30 $\mu\text{g/mL}$) preincubated with 1.0 mM biotin (c). (C) Dissociations of biotin-mAb (obvious) and biotin-streptavidin complex (almost no change).^[23]

Lots of other biomolecular interaction measurements have been successfully realized by LSPR biosensing technique. Among them, the antibody-antigen interaction is extensively studied until now.^[34-63] Figure 1.5 (A) displays the LSPR wavelength shifts of a nanobiosensor consisting of silver nanotriangle for the detection of different concentrations of ADDL, a marker for Alzheimer's disease. Figure 1.5 (B) shows the experimental data of enhanced LSPR shift for the binding of the second anti-ADDL antibody. Meanwhile, the surface-confined thermodynamic affinity constant can also be determined. More importantly, kinetics analysis of antibody-antigen binding can be realized using LSPR biosensor. Figure 1.5 (C) demonstrates the real time binding kinetics of antibody-antigen binding by gold nanorod array, which is shown on the top panel of Figure 1.5 (C). From the fitting data, the binding equilibrium constants (k_{on} , k_{off} , k_{eq}) for an antigen-antibody interaction can be calculated for the first time by LSPR biosensor. Figure 1.5 (D) demonstrates the specificity of such LSPR biosensor. At step e, the nonspecific binding induced an extremely weak affect to the LSPR signal change. However, at step g, the specific binding significantly induced red shift of the LSPR peak.

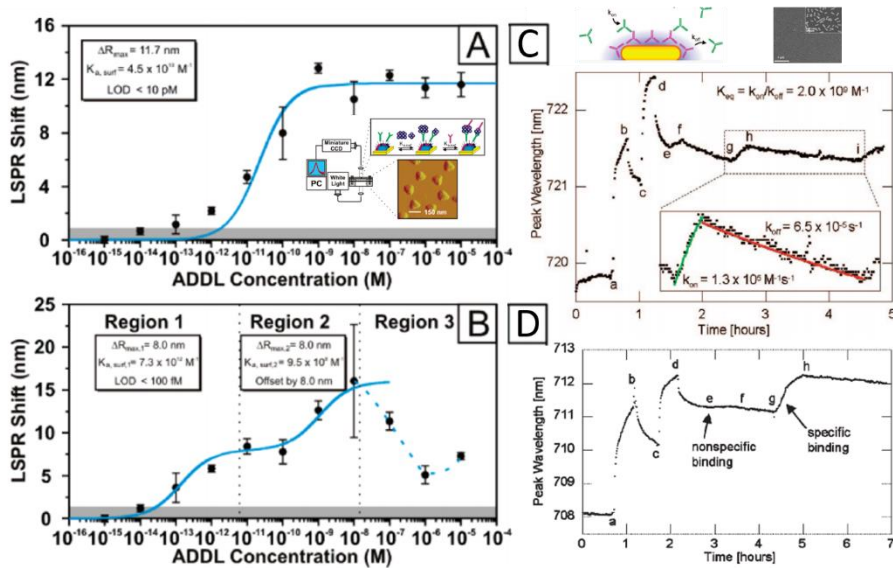


Figure 1.5 (A) Quantitative response curves of amyloid- β derived diffusible ligands (ADDLs). (B) Enhanced LSPR shift for the binding of second anti-ADDL antibody to the ADDL functionalized Ag nanobiosensor.^[43] (C) Demonstration of sensor specificity. Immunoassay with kinetic data fits of an antibody-antigen binding. The LSPR peak wavelength was measured as the various solutions flowed over the substrate of the LSPR biosensor in a continuous experiment versus time. (D) Real time binding kinetics provide an explicit demonstration of specificity with the response to both nonspecific and specific targets of identical molecular weight and concentration.^[60]

Until now, in addition to biotin-streptavidin and antibody-antigen interactions, LSPR sensing has been used to probe other biomolecular interactions, including DNA-hybridization,^[64] DNA-protein^[65, 66] and so on. In comparison with SPR biosensor, the simplicity in optical setup and the low cost make LSPR biosensor good candidate for biosensing, however, only low sensitivity is expected due to the broad LSPR band. Researchers have tried lots of approaches to improve the sensitivity of LSPR biosensor. Two approaches have been proved to be able to boost the sensitivity effectively. One is the introduction of Fano resonance induced by coupled plasmonic systems. Another one is the introduction of interparticle coupling by utilizing biomolecular labeled metallic nanoparticles target.

Fano resonance, which was first observed by Ugo Fano experimentally in 1935 and now bears his name.^[67] He theoretically described the Fano resonance in quantum autoionizing states of atoms in 1961.^[68] The Fano resonance is induced by the overlap of a discrete state with a continuum state, where destructive and constructive interferences take place at close energy positions, which results in the asymmetric profile. Until now, the Fano resonance has been extensively applied in various systems to explain many phenomena. Among them, the plasmonic Fano resonance attracts lots of attentions due to its unique properties. The optical properties of metallic nanostructures can be easily controlled by changing the geometry and composition of nanostructures. Recently, sharp Fano resonance in plasmonic metallic nanostructures has been reported. This is very important for biosensing because narrower full width at half maximum (FWHM) and higher detection limit have been realized by plasmonic Fano resonance.^[69,70]

Figure 1.6 represents a novel Fano resonant biosensor based on gold mushroom array (GMRA) structure. The Fano resonance is derived from the interference between Wood's anomaly and LSPR. Figure 1.6 (a) shows the SEM image of GMRA structure. Figure 1.6 (b), (c) and (d) show the RI sensing behaviors. A RI sensitivity as large as 1015 nm/RI unit (RIU) with spectral line width as narrow as 10 nm are realized. The representative Cytochrome c (Cyt c) and alphafetoprotein (AFP) detection is shown from Figure 1.6 (e) to Figure 1.6 (h). Importantly, the key biosenser performance parameter, the figure of merit (FOM), which is introduced by Sherry et al. to directly compare the overall performance of LSPR sensors, will increase closely to the theory limit.^[81] The FOM can be defined as below:

$$\text{FOM} = \frac{\text{m(eV} \cdot \text{RIU}^{-1})}{\text{FWHM(eV)}} \quad (1.2)$$

The FOM values of LSPR sensor without Fano resonance are normally below 5. However, the LSPR sensor with Fano resonance can be improved by several tens of order. This FOM value of GMRA structure can reach 108, which is comparable to the

theoretically estimated upper FOM limit for commercially available sensors based on propagating surface plasmon resonances.

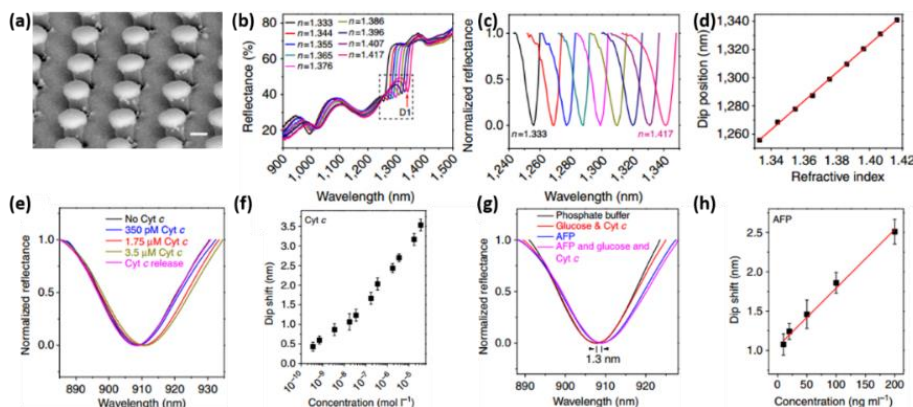


Figure 1.6. (a) SEM image of GMRA structure. (b) Reflectance spectra of the GMRA immersed in glycerine water mixture solutions with varying compositions. (c) Normalized reflectance spectra for D1 in the spectral region indicated with the dashed box in (b). (d) Relationship between the wavelength evolution of D1 and the surrounding RI. (e) Representative reflectance spectra of the GMRA after the treatment of Cyt c solutions at different concentrations. (f) Relationship between the shift of the dip and Cyt c concentration. (g) Reflectance spectra measured when an anti-AFP-functionalized GMRA was immersed in phosphate buffer solution (pH = 7.1) without AFP, a mixture solution of glucose (5 mM) and Cyt c (1.75 μM), an AFP solution (20 ng ml^{-1}), and a mixture solution of AFP (20 ng ml^{-1}), glucose (5 mM) and Cyt c (1.75 μM), respectively. (h) Relationship between the shift of the dip and AFP concentration. The red line is a linear fit.^[75]

The interparticle coupling between two closely spaced nanoparticles can affect the optical properties by the significant near-field coupling. The LSPR peak will have a red shift when reducing the distance between two closely spaced nanoparticles as shown in Figure 1.7 (1). The red shift of the resonant peak observed in the far-field spectrum is affected by the near-field coupling between two nanoparticles. This provides a new approach to increase the sensitivity of LSPR biosensor. For example, both the Ag and

Au nanodimers show a large LSPR peak shifts (102 nm in Ag, 23 nm in Au) after binding as shown in Figure 1.7 (2). The antibody-labeled gold nanoparticles can increase the LSPR peak shift of silver nanotriangles by up to 400% as compared to comparable concentrations of native antibody without labeled Au nanoparticles as shown in Figure 1.7 (3).

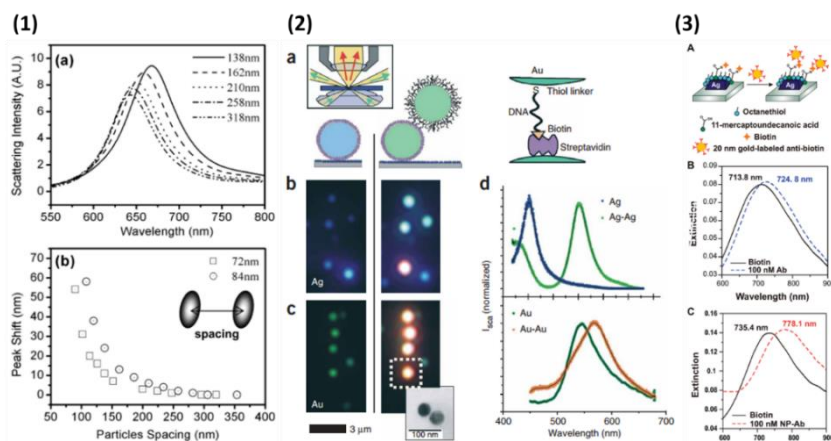


Figure 1.7. (1) Interparticle coupling between two Au nanoparticles. (a) Simulated scattering spectra of two coupled Au nanoparticles with center-center particle spacing from 138 to 318 nm. (b) LSPR peak wavelength as a function of particle center-center spacing. (2) Color effect on Au and Ag nanoparticles and nanodimers. (a) First, Au or Ag nanoparticles functionalized with streptavidin are attached to the glass surface (left). A second particle is attached to the first particle (center) via biotin-streptavidin interaction (right). (b) Individual Ag particles appear blue (left) and Ag nanodimers blue-green (right). (c) Individual Au particles appear green (left), Au particle nanodimers, orange (right). (d) Representative scattering spectra of individual particles and particle pairs for Ag (top) and Au (bottom). (3) Biosensitivity enhancement by interparticle coupling. (A) Ag nanoparticle is firstly modified by biotin, antibiotin and antibiotin labeled Au nanoparticles are subsequently linked to the Ag nanoparticle. (B) LSPR spectra before (solid black) and after (dashed blue) binding of native antibiotin, showing a LSPR peak shift of 11 nm. (C) LSPR spectra before (solid black) and after (dashed red) binding of antibiotin labeled nanoparticles, showing LSPR peak shift of 42.7 nm.

The spectral shift of closely-spaced nanodimers is induced by the near-field coupling. The introduced near-field coupling can boost the sensitivity of LSPR biosensor. However, ponderous instruments for optical measurements still limit its practical application. The fabrication of portable and miniaturized biosensors remains a challenge for optical biosensors. Recently, the surface plasmon-induced photon-to-electron conversion system has received much interest. This makes the electrical measurement of biomolecular interaction possible, which can overcome the disadvantages of optical measurement. However, the sensitivity is low because it also relies on the refractive index change. The plasmon-induced photocurrent generation is believed to be activated by the near-field enhancement of LSPR. However, the near-field coupling effect on photocurrent generation has not been explored. The motivation of this thesis is to utilize the near-field coupling enhanced photocurrent generation to achieve simple and highly sensitive photoelectrochemical (PEC) biosensor and explore the binding affinity and kinetics of biomolecular interactions.

1.2 Optical properties of localized surface plasmon resonance

To give a better understanding of the LSPR, the surface plasmons (SPs) should be introduced first. SPs are generated by the collective oscillations of surface electrons of metallic film (e.g. Au, Ag) when the light irradiated on the surface between metallic film and dielectric (Figure 1.8 shows the representative propagating surface plasmon polaritons (SPPs) along the interface of Au film and dielectric material). The excited SPPs have a penetration depth of several hundred nanometers, which make it very sensitive to the surrounding RI change. This is also the principle of SPR biosensor.

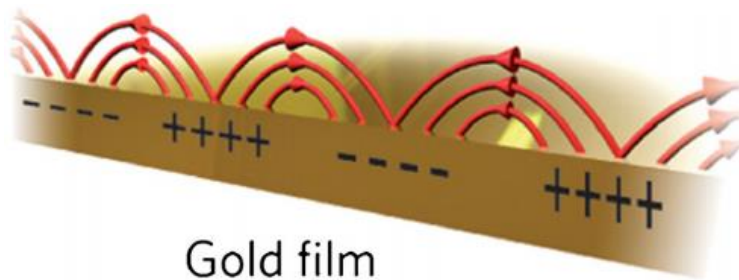


Figure 1.8 Schematic of surface plasmon polaritons that propagating along the Au-dielectric or Au-air interface.^[85,86]

Figure 1.9 shows the working schematic of a typical SPR biosensor. Firstly, receptors are fully immobilized on the sensor chip with Au film. The analyte solution with different concentrations is introduced by a flow channel. The SPP is excited by polarized light coupled with a prism and detected in reflectance. During the flow of analyte solution, the signal change can be detected real time to record the binding between analyte and receptors. After the binding between receptor and analyte reaching saturation, the signal will be stable. Noticed that the receptor should retain their native conformation and specific binding activity to bind the analyte and resistant to non-specific binding of other molecules. This is very important to reveal the binding affinity and kinetics.

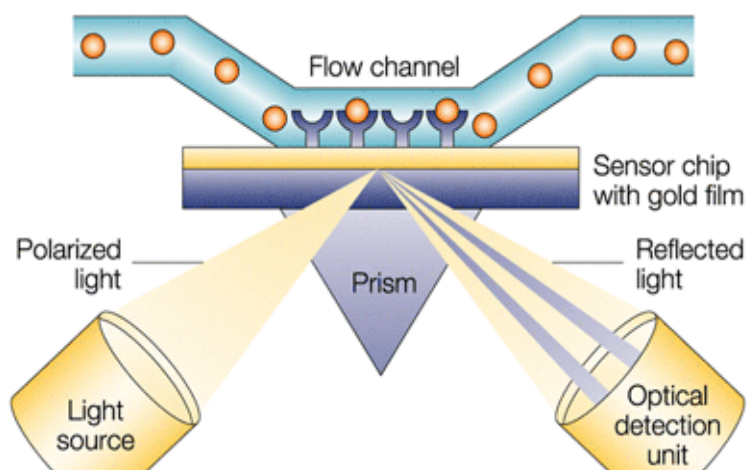


Figure 1.9 Schematic of SPR biosensor.^[87,88]

Figure 1.10 shows a typical SPR biosensor sensorgram using to detect the analyte. At first, a buffer solution passes through the flow channel to get the base line (stable environment). At a certain time, the analyte solution in the running buffer passes over the receptor coated biosensor chip and the analytes starts to bind to the receptors. The induced RI change at the sensor chip surface affects SPR signal, realizing the real time detection of molecular association. This part of association phase gives the information of observed association rate (k_{obs}). If the concentration of analyte is known, the association rate constant of the interaction (k_{ass}) can be determined. As the analyte solution passing through the flow channel, when the amounts of association and dissociation between receptors and analyte saturates, the signal will be stable without any change. This means that the association and dissociation get equilibrium. After that, the buffer solution replaced the analyte solution, the receptor-analyte complex will dissociate, making the SPR signal change reversely. This dissociation phase gives the information of dissociation rate constant (k_{diss}). The binding affinity of the interaction can be calculated as $K_D = 1/K_A = k_{diss}/k_{ass}$. The receptor will be regenerated by flowing regeneration solution (for example, high salt or low pH) to disrupt binding. This will make the receptor free to work again.

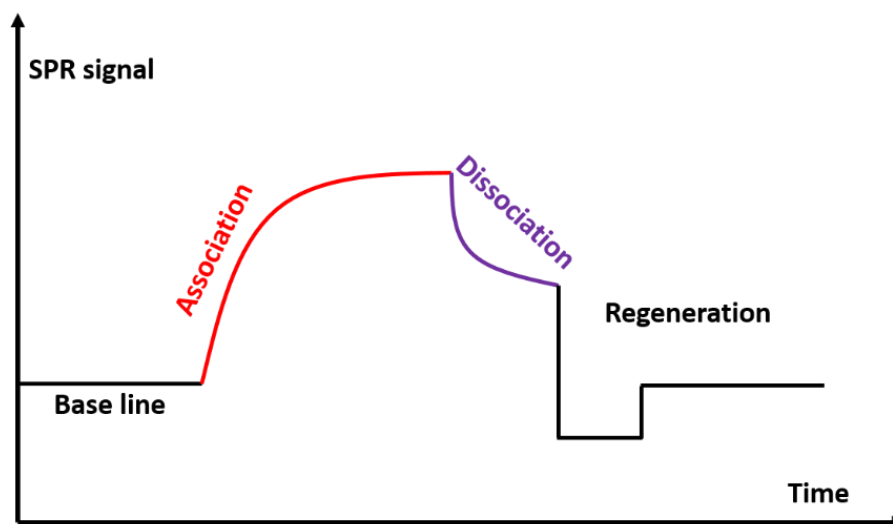


Figure 1.10 Schematic of a typical SPR biosensor sensorgram with three phases, association, dissociation and regeneration.

As mentioned, the SPPs are propagating waves at a metal-dielectric interface. Different from SPPs, localized surface plasmons (LSPs) are the collective oscillations of conduction electrons at the surface of metallic nanostructures as shown in Figure 1.11. Different from propagating SPPs, LSPs can be excited by direct light illumination without the critical phase-matching techniques needed for SPR biosensor as shown in Figure. 1.9.

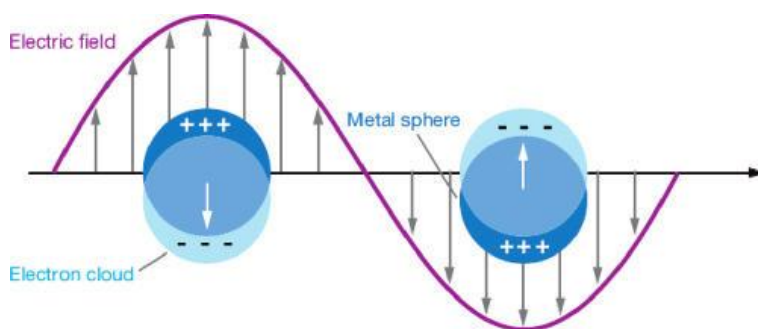


Figure 1.11 Schematic of LSPR in a metal sphere and the displacement of the conduction electron cloud relative to the nuclei.^[10]

The optical properties of LSPR have also been extensively explored. Normally, two approaches are applied to explore the properties of LSPR: far-field and near-field measurement. For example, the color change of metal doped silica relies on the far-field properties of LSPR, which are the intense light absorption and scattering. Therefore, the extinction spectrum measurement in the far-field is often used to explore the optical properties of LSPR. Near-field measurement is another effective approach to explore the nanostructures which is used to detect the local electromagnetic field enhancement. This is usually analyzed by numerical simulations.

1.2.1 Far-field spectral properties

The metallic nanoparticles show different colors, this is due to the light can be influenced by particle shape, size and surrounding environment. The application of nanostructured materials can be traced back to 4th century: the Lycurgus Cup (Rome),

a kind of dichroic glass. The colloidal gold and silver in the glass allow it to look opaque green when lit from outside but translucent red when light shines through the inside as shown in Figure 1.12 (a) and (b), respectively. The scientific researchers first explored the optical properties of metallic nanostructures in the far-field, normally the extinction spectrum measurement.

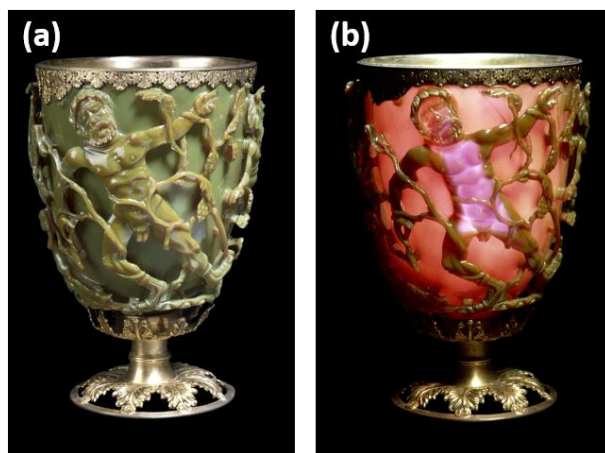


Figure 1.12 The Lycurgus Cup in reflected (a) and transmitted (b) light.

http://www.britishmuseum.org/research/collection_online/collection_object_details.aspx?objectId=61219&partId=1

1.2.1.1 Individual metallic nanoparticles

The individual metallic nanoparticles were firstly explored in the far-field measurement including nanoprisms,^[89] nanorings,^[90] nanospheres,^[91] nanocubes,^[91] nanobranches,^[91] nanorods,^[91] nanobipyramids and so on. Figure 1.13 (A-J) shows the transmission electron microscopy (TEM) images of various types of Au nanoparticles. The extinction spectra were usually measured to explore the far-field properties of metallic nanoparticles with different shapes and sizes by UV-visible/NIR spectrophotometer as shown in Figure 1.13 (K, L). Normally, there will only one LSPR peak as shown in Figure 1.13 (K-a) and (K-b) for Au nanospheres and nanocubes. However, Au nanorods show two LSPR peaks (c-e). One peak (longer wavelength) is due to the excitation of longitudinal LSPR mode associated with the electron

oscillations along the length axis, and another one (shorter wavelength) is the transverse LSPR mode excited by light polarized along the transverse direction. Nanobipyramids and nanobranches also show two LSPR peaks as shown in Figure 1.13 (L). Different nanostructures have different RI sensitivities as shown in Figure 1.13 (M).

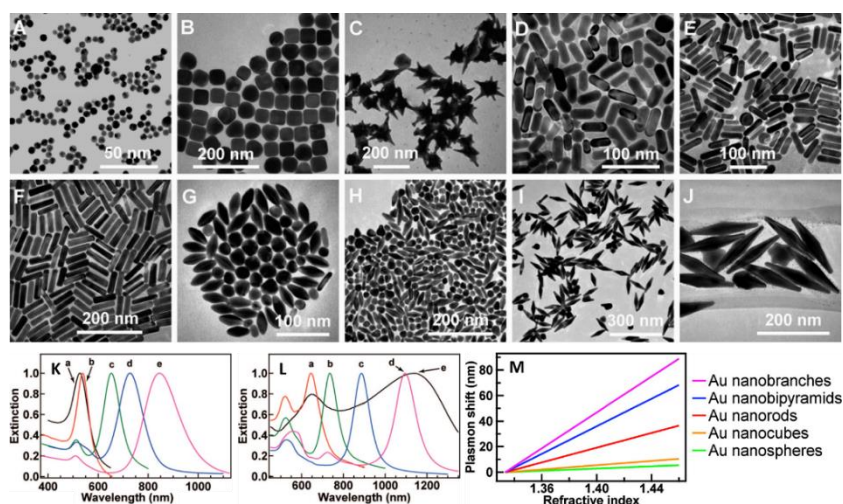


Figure 1.13 The representative TEM images of Au nanoparticles of different shapes and sizes. (A) Nanospheres. (B) Nanocubes. (C) Nanobranches. (D) Nanorods (aspect ratio 2.4 ± 0.3). (E) Nanorods (aspect ratio 3.40 ± 0.5). (F) Nanorods (aspect ratio 4.6 ± 0.8). (G) Nanobipyramids (aspect ratio 1.5 ± 0.3). (H) Nanobipyramids (aspect ratio 2.7 ± 0.2). (I) Nanobipyramids (aspect ratio 3.9 ± 0.2). (J) Nanobipyramids (aspect ratio 4.7 ± 0.2). Normalized extinction spectra of Au nanoparticles of different shapes and sizes. (K) Spectra a-e correspond to nanospheres, nanocubes, and nanorods with aspect ratios of 2.4 ± 0.3 , 3.4 ± 0.5 , and 4.6 ± 0.8 , respectively. (L) Spectra a-e correspond to nanobipyramids with aspect ratios of 1.5 ± 0.3 , 2.7 ± 0.2 , 3.9 ± 0.2 , and 4.7 ± 0.2 , and nanobranches, respectively. (M) The LSPR peak shifts of Au nanoparticles of different shapes and sizes with different RI.^[91]

1.2.1.2 Coupled plasmonic systems

The rapid development of nanofabrication techniques makes it possible for accurate controlling the size and geometry of the nanostructures. Researchers have made much

effort to tune the optical properties of LSPR. Until now, a plethora of coupled plasmonic systems with striking properties have been successfully fabricated.^[92-107] The couplings can not only occur between plasmons,^[92-98] but also other types of modes.^[99-107]

Dramatic near-field coupling will be achieved by placing two metallic nanoparticles closely (nanodimer). Strong near-field enhancement at the gap will modify the spectrum resulting in a red shift of LSPR in the far-field. Ueno et al. reported near-field coupling assisted two-photon polymerization by Au nanodimer structures. Figure 1.14 shows the investigation of near-field coupling of Au nanodimer structures *via* two-photon polymerization of the photoresist surrounding the nanoparticles. Only 5.6 nm gap (Figure 1.14 a) leads to a very strong near-field coupling under the vertical polarization excitation (Figure 1.14 b) and induce similar polymerization of the photoresist with only 0.01 s irradiation in comparison with horizontal polarization excitation with 100 s irradiation (Figure 1.14 c). The huge near-field enhancement located at the gap position can reach 6.3×10^3 by finite-difference time-domain (FDTD) software package (Lumerical, Inc.) solutions simulations (Figure 1.14 d) under the vertical polarization excitation. However, the near-field enhancement can only reach 85 under the horizontal polarization excitation without interparticle coupling.

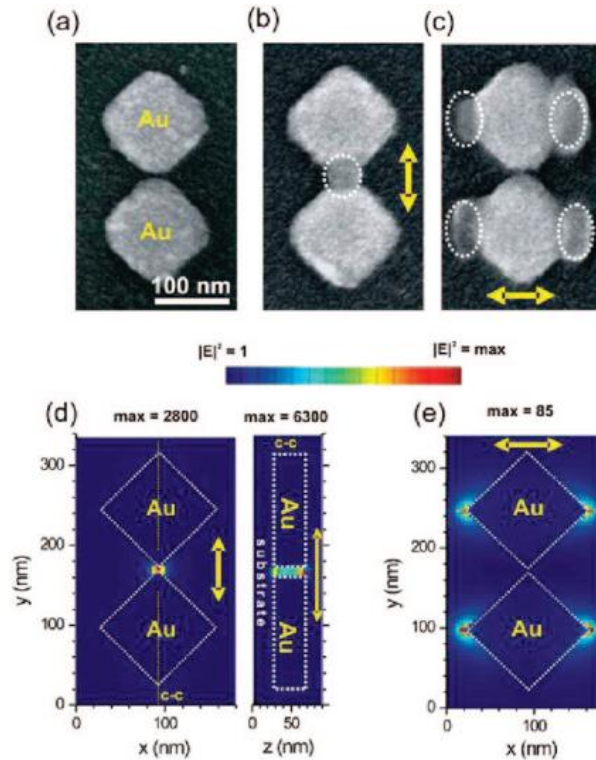


Figure 1.14 Strongly coupled Au nanodimer structures. (a) Au nanodimer structure with 5.6 nm gap. (b) Au nanodimer structure after 0.01 s exposure to the laser beam under vertical polarized laser irradiation. (c) Au nanodimer structure after 100 s exposure under horizontal polarized laser irradiation. (d and e) are calculated near-field patterns corresponding (b and c).^[92]

Niels et al. reported a type of coupled plasmonic systems based on symmetry-breaking nanostructures as shown in Figure 1.15 (A) and (B), respectively.^[93] Figure 1.15 (A) shows Au dolmen structures consists of a planar nanorod monomer and a planar nanorod dimer. Figure 1.15 (B) presents ring-near-disk cavity structures, which are composed by an Au nanodisk and an Au nanoring. Both dolmen and ring-near-disk cavity structures show obvious Fano type resonance in the far-field experimental (Figure 1.15 (A-a) and (B-a)) and simulated (Figure 1.15 (A-b) and (B-b)) extinction spectra under the specific polarized light excitation, respectively. The Fano resonances are very sensitive to the polarization angles and can be tuned by changing the polarization direction as shown in Figure 1.15 (A-c) and (B-c), respectively. They

concluded that both the Fano resonances of two types of nanocavities are due to the coupling of dark quadrupolar and higher order modes with bright dipolar modes, which are verified by the calculated surface charge distributions in Figure 1.15 (A-d, e, f) and (B-d, e, f), respectively.

Halas et al. investigated another type of coupled plasmonic systems named as heptamer structures, which is composed by seven nanodisks, as shown in Figure 1.15 (C-a).^[97] The heptamer is totally symmetry. However, it also shows Fano resonance in the experimental and calculated dark-field scattering spectra as shown in Figure 1.15 (C-b) and Figure 1.15 (C-c), respectively. The collective modes of surrounded six nanodisks can couple efficiently with central nanodisk due to the small gaps between each nanodisk. The two relevant modes for Fano interference are hybridized bonding (superradiant) plasmon mode (the dipolar plasmons of all nanodisks oscillate in phase and in the same direction) and anti-bonding (subradiant) plasmon mode (the dipolar moment of the central nanodisk opposes the dipole moment of the surrounding six nanodisks).

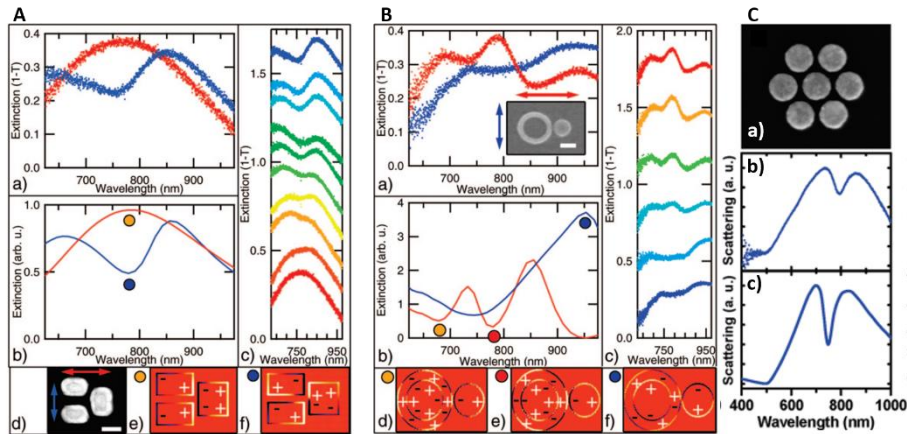


Figure 1.15 The representative far-field spectra of different coupled plasmonic systems. (A) Fano resonance of an individual dolmen structure. Respective experimental (a) and numerical (b) far-field extinction spectra, with horizontal (red) and vertical (blue) polarizations. (c) The evolution of the experimentally measured extinction as the polarization direction is changed in steps of 10° steps. (e, f) Calculated surface charge

distributions of the dipole mode and the Fano extinction dip as shown in (b).^[93] (B) Fano resonance of ring-near-disk cavity. Experimental (a) and numerical (b) spectra, respectively. (c) Experimental extinction spectra for increasing polarization in regular steps of 20°. Surface charge distribution associated with the dips at 680 nm (d) and 770 nm (e) for polarization along the dimer axis. (f) Surface charge distribution associated with the peak at 950 nm for polarization perpendicular to the dimer axis.^[93] (C) Fano resonance of heptamer structures. (a) The SEM images of heptamer structure. (b) The experimental dark-field scattering spectrum, obtained with unpolarized light. (c) Calculated dark-field spectral response of the same structure.^[97]

The LSPR mode can also couple with some other modes, including whispering gallery modes,^[99] Fabry-Perot mode modes,^[100] and waveguide modes.^[101-107] Such couplings can tune the far-field spectra with fine control and bring special applications. Tong et al. reported a coupled plasmonic system fabricated by Au nanorods loaded on silica microfiber as shown in Figure 1.16. Silica microfibers were fabricated by flame-heated taper drawing of standard optical fibers, which can support high quality-factor whispering gallery modes as shown in Figure 1.16 (a). Individual Au nanorods were elaborately deposited on the surface of the microfiber as shown in the inset of Figure 1.16 (b). The scattering spectra of single Au nanorods coupled to microfibers with diameters from 0.51 to 25.4 μm were investigated. Silica microfiber with 1.46 μm diameter can achieve single-band 2-nm-line-width plasmon resonance as shown in Figure 1.16 (b). The extremely narrow LSPR line width of such coupled plasmonic systems is inspired to realize better performance in various applications including ultrasensitivity nanosensors and ultralow-threshold plasmon lasers.

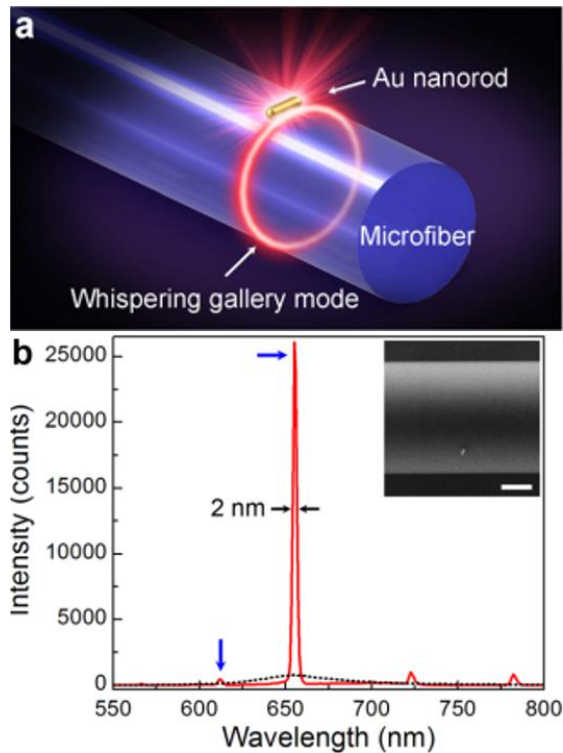


Figure 1.16 (a) Schematic diagram of coupling an Au nanorod with an optical microfiber. (b) Scattering spectra of single Au nanorods coupled to silica microfibers with diameters of 1.46 μm .^[99]

Giessen et al. placed an array of plasmonic Au nanowires on top of a waveguide ITO layer to form the coupled waveguide-plasmon modes as shown in Figure 1.17 (A-a).^[101] Periodic Au nanowires as shown in Figure (A-b), which are fabricated by EBL on top of 140-nm-thick ITO waveguide layer deposited on silica substrate. Figure (A-c) shows the corresponding extinction spectra at TE (black solid line) and TM (dashed line) polarizations. At TE polarization (incident light is parallel to the length of Au nanowires), there will be only one peak, which is due to the excitation of waveguide mode. The LSPR mode cannot be excited due to the overlong Au nanowires. At TM polarization (incident light is perpendicular to the length of Au nanowires), two resonant peaks will be excited due to the strong coupling between LSPR and waveguide mode. This novel effect is a suitable tool for photonic band gap engineering in active photonic crystals and also can be used as band-selective optical polarizer and optical switching device.^[105] The ITO waveguide layer can be replaced by other dielectric

materials such as WO_3 ^[106] and titanium dioxide (TiO_2).^[107] To obtain sensing functionality, Giessen et al. used Au nanowires on top of a gasochromic 120-nm-thick WO_3 waveguide, which undergoes a strong modification of its optical properties when exposed to hydrogen gas as shown in Figure 1.17 (B).^[106] At TM polarization, there will be a sharp dip due to the coupling between the broad plasmon peak and the narrow waveguide mode. This sharp dip is ideally suited for sensing due to its low FWHM. The extinction spectrum will be changed due to the drastically change of optical properties of the WO_3 layer upon hydrogen exposure. The combination of a chemically sensitive waveguide with plasmonic elements can lead to versatile and high-performance sensors. Daniel et al. fabricated periodic Au nanowires structures on 200-nm-thick TiO_2 waveguide layer as shown in Figure 1.17 (C).^[107] The femtosecond transient absorption spectroscopy measurements have shown that this strong coupling regime of LSPR and waveguide modes enhances the injection rate (efficiency) of plasmonic hot-charge carriers into the supporting semiconductor waveguide, showing the potential applications of this coupled system in photon-to-electron conversion.

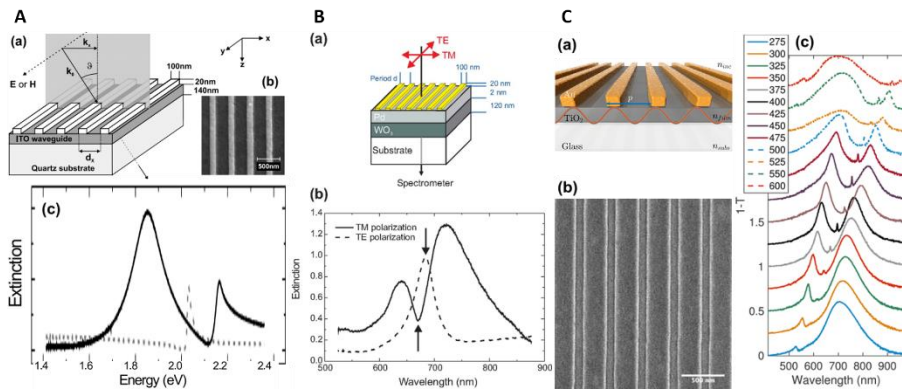


Figure 1.17 (A) Schematic view (a), SEM image (b), and measured extinction spectra with 400 nm pitch size (c) of the gold wire array on top of a 140-nm-thick ITO waveguide layer.^[101] (B) Schematic view (a), measured extinction spectra with 450 nm pitch size (b) of the gold wire array on top of a 120-nm-thick WO_3 waveguide layer.^[106] (C) Schematic view (a), SEM image (b), and measured extinction spectra with various pitch sizes (c) of the gold wire array on top of a 200-nm-thick TiO_2 waveguide layer.^[107]

1.2.2 Near-field spectral properties

The spectrum modulations of coupled plasmonic systems are derived from near-field interactions between different modes. Near-field spectrum measurement techniques are crucial to investigate near-field interactions in coupled plasmonic systems. There are several approaches to measure the near-field including scanning near-field optical microscopy (SNOM),^[108] electron energyloss spectroscopy (EELS),^[109] cathodoluminescence (CL),^[110,111] and photoemission electron microscopy (PEEM).^[112,113] These techniques play very important roles on the investigation of near-field and optimization of complex coupled plasmonic systems for various applications.

1.2.2.1 Scanning near-field optical microscopy

Pablo et al. investigated near-field properties of PI-shaped nanostructures by SNOM as shown in Figure 1.18 (a). The calculated reflection spectra of PI-shaped nanostructures under the horizontal polarization (red) and vertical polarization (blue) are shown in Figure 1.18 (b). There is no Fano resonance and only one broad peak can be observed in the reflection spectra under vertical polarization excitation, which accords well with both the experimental and calculated near-field as shown in Figure 1.18 (c). However, Fano resonance can be observed under the horizontal polarization. The experimental and calculated near-field at each wavelength position are recorded through the near-field mapping by SNOM as shown in Figure 1.18 (d). The SNOM can reveal the information of near-field (electric field intensity and phase) of coupled plasmonic system and give further understanding of plasmonic Fano resonances.

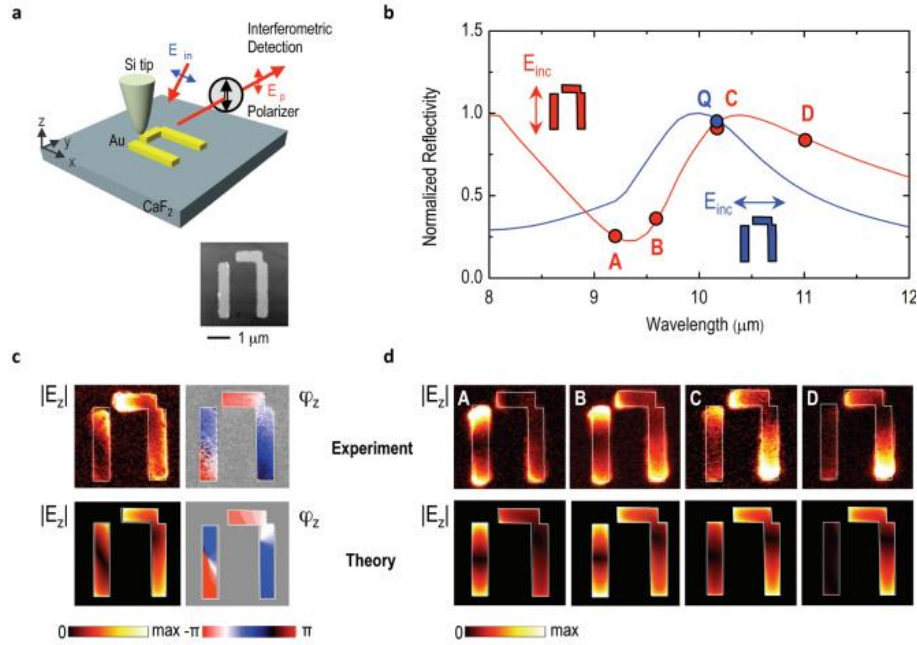


Figure 1.18 Real-space mapping of asymmetric PI-shaped structures. (a) Experimental setup of near-field imaging. (b) The normalized simulated reflection spectra at horizontal (blue) and vertical (red) polarization. (c) Experimental (up) and calculated (down) E_z under horizontal polarization, recorded at $10.2 \mu\text{m}$. (d) Experimental (up) and calculated (down) E_z under vertical polarization, recorded at the spectral positions A-D marked in (b).^[108]

1.2.2.2 Cathodoluminescence and electron energy-loss spectroscopy

Toon et al. investigated the bonding and anti-bonding plasmon modes supported by Au dolmen structures by EELS and CL.^[109] Figure 1.19 (a) and (b) show the CL (blue) and electron EELS (red) spectra of Au dolmen for excitation at different positions of dolmen structure as shown in the inset of Figure 1.19 (a). Furthermore, the EELS and CL mappings under specific wavelength excitation in Figure 1.19 (c) give the near-field intensity distribution for different plasmon modes (bonding and antibonding modes) and better understanding of interaction between different plasmon modes on coupled plasmonic systems.

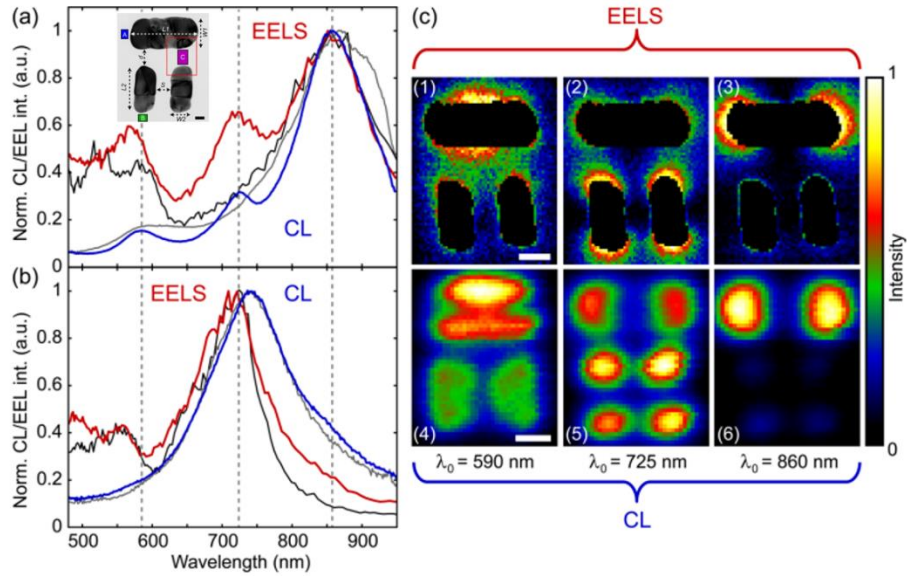


Figure 1.19 (a) CL (blue) and electron EELS (red) spectra of Au dolmen for excitation at position A of the inset. (b) CL and EELS spectra of Au dolmen for excitation at position B of the inset. (c) EELS image (1-3) and CL image (4-6) for different excitation wavelengths.^[109]

1.2.2.3 Photoemission electron microscopy

Misawa et al. investigated the near-field spectrum of single Au dolmen structure by PEEM measurement as shown in Figure 1.20 (a).^[47] The PEEM imaging under UV and femtosecond laser pulses shows both the entire morphology and hot spots of the Au dolmen as shown in Figure 1.20 (b). The PEEM imaging at four different wavelengths can reveal the different coupled modes deriving from the different hot spots locations as shown from Figure Figure 1.20 (c) to (f). The near-field spectrum of Au dolmen structure is in good accordance with the far-field spectrum, allowing for distinguishing the difference of their contribution to the near-field enhancement between plasmon hybridization and Fano resonances in plasmonic dolmen structures.

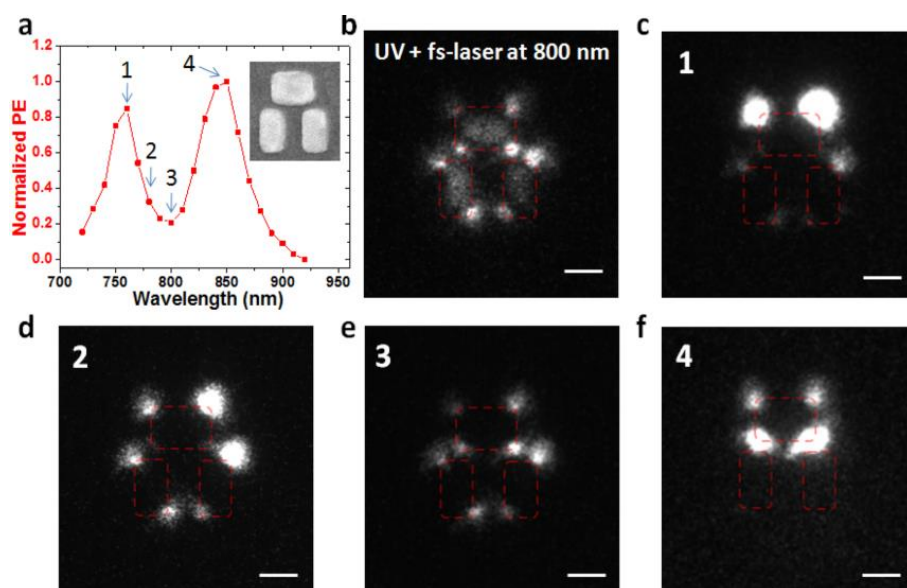


Figure 1.20 Near-field intensity spectrum of Au dolmen structure obtained from PEEM measurements. (a) Near-field spectrum of a single Au dolmen structure as shown in the inset SEM image. (b) PEEM image of Au dolmen structures irradiated with UV light and femtosecond laser pulses (800 nm), simultaneously. (c-f) PEEM images collected under irradiation with femtosecond laser pulses at four different wavelengths marked in (a).^[112]

1.3 Plasmonic photoelectrochemical biosensors

Recently, the metallic nanostructure/TiO₂ system has been applied in PEC biosensing field.^[114-116] The electric signal can overcome the optical measurement technology barrier, showing compelling advantages in comparison with optical measurement to achieve compact and small PEC biosensors. Perhaps the first PEC biosensing platform by utilizing Au nanoparticles (AuNPs)/TiO₂ electrode was reported by Zhu et al.^[114] The cytochrome c (cyt. c) modified AuNPs/TiO₂ was used to detect different concentrations of H₂O₂ solutions. Figure 1.21 (a) and (b) show the SEM image and absorption spectrum of AuNPs/TiO₂ electrode, respectively. The absorption spectrum is still broad and not good candidate for optical biosensing applications. However, as shown in Figure 1.21 (c), direct electron transfer of cyt. c has been realized at the Au/TiO₂ film, and both anodic and cathodic currents of the redox reaction have been

amplified upon visible-light irradiation. Figure 1.21 (d) shows the photocurrent response to successive addition of 1×10^{-5} M H_2O_2 under (A) visible light illumination and (B) without illumination. The analytical performance was enhanced by utilizing surface plasmon resonance effect. Most importantly, Au NPs can absorb visible light and undergo the charge separation upon irradiation with visible light, which avoids the damage on the biomolecules adsorbed on the electrode induced by UV illumination.

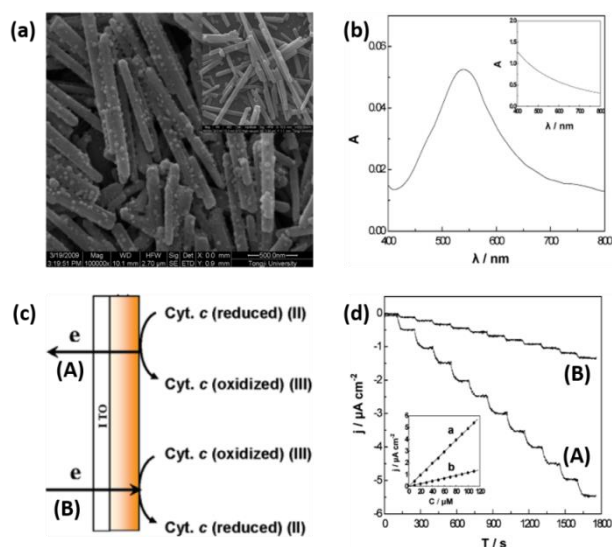


Figure 1.21 (a) SEM images of AuNPs/TiO₂ electrode, inset shows the SEM image of TiO₂ nanoneedle. (b) The absorption spectrum of AuNPs, inset shows the absorption spectrum of TiO₂ nanoneedle. (c) cyt. c modified AuNPs/TiO₂ Film: (A) Anodic and (B) cathodic photocurrent generation in the presence of reduced and oxidized cyt. C, respectively. (d) Typical photocurrent responses of AuNPs/TiO₂/cyt. c electrode to successive addition of 1×10^{-5} M H_2O_2 under (A) visible light illumination and (B) without illumination at 0 V vs Ag/AgCl in 25 mM phosphate buffer solution (PBS, pH 7.2). Inset shows the corresponding calibration curves of current density versus the concentration of H_2O_2 .^[114]

Da et al. reported a PEC protein biosensor by Au nanoparticles decorated TiO₂ nanowires and successfully achieved real time and direct measurement of binding kinetics between cholera toxin subunit B and GM1 (association and disassociation rate

constants).^[116] Figure 1.22 (a) shows the schematic of such biosensing platform. As the LSPR induced photon-to-electron conversion is mainly attributed to the plasmonically near-field enhancement effect as well as the injection of LSPR-generated hot electrons into the conduction band of TiO₂, the near-field enhancement effect and charge-transfer efficiency strongly depends on the local chemical environment fluctuation between Au and TiO₂. The Au nanoparticle-decorated TiO₂ nanowires can not only tune the energy coupling and charge transfer across the interface between these two materials, but also resulting in increased photoconversion efficiency and a much enhanced sensitivity in comparison with only TiO₂ nanowires PEC sensors. Figure 1.22 (b) shows the PEC sensing measurements using TiO₂ nanowires with and without Au nanoparticles decorations. The surface of Au nanoparticles is firstly prefunctionalized with a monolayer of cellular receptor GM1, which can selectively recognize the presence of cholera toxin subunit-B (CTB). The addition of different concentrations of CTB (e.g., 16.7 nM) onto the PEC cell leads to an increase of photocurrent density of Au nanoparticle-decorated TiO₂ nanowires, which reaches equilibrium within 30 s. In contrast, a much smaller photocurrent change is observed on GM1-functionalized TiO₂ nanowires without Au nanoparticles. Furthermore, Figure 1.22 (c) shows another important feature of the PEC sensor: the real time photocurrent measurement allows for direct measurement and analysis of binding kinetics between GM1 and CTB. The observed kinetic rate constant (k_{obs}) calculated by fitting the rising phase of the sensor gram curve and shows linear relationship with association (k_{on}) and disassociation (k_{off}): $k_{\text{obs}} = k_{\text{on}} C + k_{\text{off}}$, in which C stands for CTB concentrations. The slope and intercept can be calculated corresponding to k_{on} and k_{off} , respectively. Figure 1.22 (d) shows the photocurrent response to the addition of different molecular interferences, such as biotin, IgG, lysozyme, and streptavidin, each with a final concentration of 20 nM, does not result in an observable signal of photocurrent change for the GM1 functioned Au nanoparticle-decorated TiO₂ nanowires PEC sensor, which suggests its excellent selectivity.

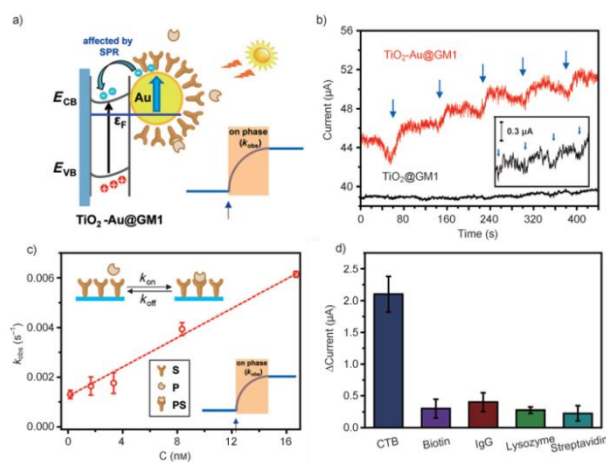


Figure 1.22 (a) Schematic of LSPR-enhanced PEC sensing mechanisms: Functionalization of surface receptors (GM1) and binding of molecular targets (CTB) on Au nanoparticles decorated TiO₂ nanowires sensor surfaces. The binding of GM1 and CTB can effectively tune the hot electron transfer across the interface between Au nanoparticles and TiO₂ nanowires. (b) Successive injections of CTB solutions induced photocurrent response of GM1 functioned TiO₂ nanowires without Au nanoparticles (black curve) and GM1 functioned Au nanoparticles decorated TiO₂ nanowires (red curve). Arrows indicate the successive injection timing. Inset is the zoom-in of the photocurrent response of GM1 functioned TiO₂ nanowires without Au nanoparticles. (c) Schematic illustration of binding kinetics: observed kinetic rate constant (k_{obs}), association (k_{on}) and disassociation (k_{off}). k_{obs} at various concentrations are observed by single-exponential fitting the rising phase of sensor gram and concentration-dependent k_{obs} has linear relationship between k_{on} and k_{off} . The slope and intercept of the linear fit represent the k_{on} and k_{off} , respectively. (d) Good selectivity of CTB by GM1 functioned Au nanoparticles decorated TiO₂ nanowires biosensor over other proteins and small molecular interferences.^[116]

The electronic circuits and detectors of such plasmonic PEC biosensor can be integrated on only one chip. However, only low sensitivity is expected because it is similar to conventional optical LSPR biosensor, which relies on the spectrum change of LSPR.

1.4 Aim and outline of this thesis

This thesis aims at investigating the influence of near-field coupling on photocurrent generation and constructing highly sensitive PEC biosensor using near-field coupling enhanced photocurrent generation for *in situ* real-time measurement of the binding affinity and kinetics of biomolecular interactions. The metallic nanoparticles loaded semiconductor photoelectrodes have been extensively utilized in photocurrent generation deriving from the plasmon-induced electron transfer from metallic nanoparticles to the attached semiconductor. However, it has not been understood how the near-field coupling influence the photocurrent generation. I proposed to explore the influence of near-field coupling on the photocurrent generation using a strongly coupled waveguide-LSPR modes with multiple near-field peaks. Based on this result, a highly sensitive PEC biosensor using the near-field coupling between AuNIs on TiO₂ and AuNPs by connecting using biotin-streptavidin interaction has been developed. Four chapters will be presented in this thesis. In chapter 1, I will describe the backgrounds and motivations of this study briefly, introduce conventional optical LSPR biosensor, newly emerged plasmonic PEC biosensor, spectral properties of various nanostructures (individual nanostructures and coupled plasmonic systems) both in far- and near-field measurement. In chapter 2, I will use the plasmon induced photocurrent generation to measure the near-field spectra of strongly coupled waveguide-LSPR modes, demonstrating that the PEC response is corresponding to the near-field coupling, showing the potential to realize highly sensitive PEC biosensor utilizing near-field coupling. In chapter 3, a sensitive PEC biosensor based on biomolecule modified Au AuNIs decorated TiO₂ photoelectrode is successfully proposed and developed to measure the binding affinities and kinetics between biotin and streptavidin by using the near-field coupling enhanced photocurrent generation. Chapter 4 will summarize the results described in chapter 2 and chapter 3 and make perspectives beyond the research investigated in this thesis.

1.5 References

- [1]. Anthony, T.; Isao, K.; George, W., *Biosensors: Fundamentals and Applications*. Oxford University Press: Oxford, UK, **1987**.
- [2]. Banica, F. G., *Chemical Sensors and Biosensors: Fundamentals and Applications*. John Wiley & Sons, Ltd: West Sussex (UK), **2012**.
- [3]. Clark, L. C.; Lyons, C., Electrode Systems for Continuous Monitoring in Cardiovascular Surgery. *Annals of the New York Academy of Sciences* **1962**, *102*, 29-45.
- [4]. Updike, S.J.; Hicks, G.P., The enzyme electrode. *Nature* **1967**, *214*, 986–988.
- [5]. Homola, J.; Yee, S. S.; Gauglitz, G., Surface plasmon resonance sensors: review. *Sensors and Actuators B-Chemical* **1999**, *54*, 3-15.
- [6]. Homola, J., Surface plasmon resonance sensors for detection of chemical and biological species. *Chemical Reviews* **2008**, *108*, 462-493.
- [7]. Kreibig. U.; Vollmer. M., *Optical Properties of Metal Clusters*, Springer. Berlin, **1995**.
- [8]. Mulvaney. P., Surface plasmon spectroscopy of nanosized metal particles. *Langmuir* **1996**, *12*, 788–800.
- [9]. Hartland. G. V., Optical studies of dynamics in noble metal nanostructures. *Chemical Reviews* **2011**, *111*, 3858–3887.
- [10]. Kelly, K. L.; Coronado, E.; Zhao, L. L.; Schatz, G. C., The optical properties of metal nanoparticles: The influence of size, shape, and dielectric environment. *Journal of Physical Chemistry B* **2003**, *107*, 668-677.
- [11]. Jeanmaire, D. L.; Van Duyne, R. P., *Surface Raman Spectroelectrochemistry: Part1*.

Heterocyclic, Aromatic, and Aliphatic Amines Adsorbed on the Anodized Silver Electrode. *Journal of Electroanalytical Chemistry and Interfacial Electrochemistry* **1977**, *84*, 1–20.

[12] Kneipp, K.; Wang, Y.; Kneipp, H.; Perelman, L. T.; Itzkan, I.; Dasari, R. R.; Feld, M. S., Single Molecule Detection Using Surface-Enhanced Raman Scattering (SERS). *Physical Review Letters* **1997**, *78*, 1667–1670.

[13] Nie, S.; Emory, S. R., Probing Single Molecules and Single Nanoparticles by Surface-Enhanced Raman Scattering. *Science* **1997**, *275*, 1102–1106.

[14] Zhang, Y.; Zhen, Y. R.; Neumann, O.; Day, J. K.; Nordlander, P.; Halas, N. J., Coherent Anti-Stokes Raman Scattering with SingleMolecule Sensitivity Using a Plasmonic Fano Resonance. *Nature Communications* **2014**, *5*, 4424.

[15]. Haes, A. J.; Van Duyne, R. P., Preliminary studies and potential applications of localized surface plasmon resonance spectroscopy in medical diagnostics. *Expert Review of Molecular Diagnostics* **2004**, *4*, 527-537.

[16]. Zhao, J.; Zhang, X. Y.; Yonzon, C. R.; Haes, A. J.; Van Duyne, R. P., Localized surface plasmon biosensors. *Nanomedicine* **2006**, *1*, 219-228.

[17]. Anker, J. N.; Hall, W. P.; Lyandres, O.; Shah, N. C.; Zhao, J.; Van Duyne, R. P., Biosensing with plasmonic nanosensors. *Nature Materials* **2008**, *7*, 442-453.

[18]. Sepulveda, B.; Angelome, P. C.; Lechuga, L. M.; Liz-Marzan., LSPR-based nanobiosensors. *Nano Today* **2009**, *4*, 244-251.

[19]. K. M. Mayer.; J. H. Hafner., Localized surface plasmon resonance sensors. *Chemical Reviews* **2011**, *111*, 3828–3857.

[20]. M. C. Estevez.; M. A. Otte.; B. Sepulveda.; L. M. Lechuga., Trends and challenges of refractometric nanoplasmonic biosensors: A review. *Analytica Chimica Acta* **2014**, *806*, 55–73.

- [21]. Haes, A. J.; Van Duyne, R. P., A nanoscale optical biosensor: sensitivity and selectivity of an approach based on the localized surface plasmon resonance spectroscopy of triangular silver nanoparticles. *Journal of the American Chemical Society* **2002**, *124*, 10596–10604.
- [22]. McFarland, A. D.; Van Duyne, R. P., Single silver nanoparticles as real-time optical sensors with zeptomole sensitivity. *Nano Letters* **2003**, *3*, 1057-1062.
- [23]. Nath. N.; Chilkoti. A., A colorimetric gold nanoparticle sensor to interrogate biomolecular interactions in real time on a surface. *Analytical Chemistry* **2002**, *74*, 504–509.
- [24]. Nath. N.; Chilkoti. A., Label-free biosensing by surface plasmon resonance of nanoparticles on glass: optimization of nanoparticle size. *Analytical Chemistry* **2004**, *76*, 5370–5378.
- [25]. Marinakos, S. M.; Chen, S. H.; Chilkoti, A., Plasmonic detection of a model analyte in serum by a gold nanorod sensor. *Analytical Chemistry* **2007**, *79*, 5278-5283.
- [26]. Chen, C. D.; Cheng, S. F.; Chau, L. K.; Wang, C. R. C., Sensing capability of the localized surface plasmon resonance of gold nanorods. *Biosensors and Bioelectronics* **2007**, *22*, 926-932.
- [27]. T. Arai.; P. K. R. Kumar.; C. Rockstuhl.; K. Awazu.; J. Tominaga., An optical biosensor based on localized surface plasmon resonance of silver nanostructured films. *Journal of Optics A: Pure and Applied Optics* **2007**, *9*, 699–703.
- [28]. Wang, Y.; Qian, W. P.; Tan, Y.; Ding, S. H., A label-free biosensor based on gold nanoshell monolayers for monitoring biomolecular interactions in diluted whole blood. *Biosensors and Bioelectronics* **2008**, *23*, 1166-1170.
- [29]. Hiep, H. M.; Yoshikawa, H.; Saito, M.; Tamiya, E., An Interference Localized

Surface Plasmon Resonance Biosensor Based on the Photonic Structure of Au Nanoparticles and SiO₂/Si Multilayers. *ACS Nano* **2009**, 3, 446-452.

[30]. Dahlin, A. B.; Chen, S.; Jonsson, M. P.; Gunnarsson, L.; Kall, M.; Hook, F., High-Resolution Microspectroscopy of Plasmonic Nanostructures for Miniaturized Biosensing. *Analytical Chemistry* **2009**, 81, 6572-6580.

[31]. Li, X.; Jiang, L.; Zhan, Q. Q.; Qian, J.; He, S. L., Localized surface plasmon resonance (LSPR) of polyelectrolyte-functionalized gold-nanoparticles for bio-sensing. *Colloid Surface A* **2009**, 332, 172-179.

[32]. Hernandez, F. J.; Dondapati, S. K.; Ozalp, V. C.; Pinto, A.; O'Sullivan, C. K.; Klar, T. A.; Katakis, I., Label free optical sensor for Avidin based on single gold nanoparticles functionalized with aptamers. *Journal of Biophotonics* **2009**, 2, 227-231.

[33]. Kim. H. M.; Jin. S. M.; Lee. S. K.; Kim. M. G.; Shin. Y. B., Detection of biomolecular binding through enhancement of localized surface plasmon resonance (LSPR) by gold nanoparticles. *Sensors* **2009**, 9, 2334–2344.

[34]. Zhu, S. L.; Du, C. L.; Fu, Y. Q., Localized surface plasmon resonance-based hybrid Au–Ag nanoparticles for detection of Staphylococcus aureus enterotoxin B. *Optical Materials* **2009**, 31, 1608-1613.

[35]. Yu, C. X.; Irudayaraj, J., Multiplex Biosensor Using Gold Nanorods. *Analytical Chemistry* **2007**, 79, 572-579.

[36]. Yamamichi, J.; Iida, M.; Ojima, T.; Handa, Y.; Yamada, T.; Kuroda, R.; Imamura, T.; Yano, T., The mesoscopic effect on label-free biosensors based on localized surface plasmon resonance of immobilized colloidal gold. *Sensors and Actuators B-Chemical* **2009**, 143, 349-356.

[37]. Riboh, J. C.; Haes, A. J.; McFarland, A. D.; Yonzon, C. R.; Van Duyne, R. P., A Nanoscale Optical Biosensor: Real-Time Immunoassay in Physiological Buffer

Enabled by Improved Nanoparticle Adhesion. *Journal of Physical Chemistry B* **2003**, *107*, 1772-1780.

[38]. Kreuzer, M. P.; Quidant, R.; Salvador, J. P.; Marco, M. P.; Badenes, G., Colloidal-based localized surface plasmon resonance (LSPR) biosensor for the quantitative determination of stanozolol. *Analytical and Bioanalytical Chemistry* **2008**, *391*, 1813-1820.

[39]. Kreuzer, M. P.; Quidant, R.; Badenes, G.; Marco, M. P., Quantitative detection of doping substances by a localised surface plasmon sensor. *Biosensors and Bioelectronics* **2006**, *21*, 1345-1349.

[40]. Kitano, H.; Anraku, Y.; Shinohara, H., Sensing Capabilities of Colloidal Gold Monolayer Modified with a Phenylboronic Acid-Carrying Polymer Brush. *Biomacromolecules* **2006**, *7*, 1065-1071.

[41]. Kalele, S. A.; Ashtaputre, S. S.; Hebalkar, N. Y.; Gosavi, S. W.; Deobagkar, D. N.; Deobagkar, D. D.; Kulkarni, S. K., Sensing Capabilities of Colloidal Gold Monolayer Modified with a Phenylboronic Acid-Carrying Polymer Brush. *Chemical Physics Letters* **2005**, *404*, 136-141.

[42]. Hiep, H. M.; Yoshikawa, H.; Tamiya, E., Interference Localized Surface Plasmon Resonance Nanosensor Tailored for the Detection of Specific Biomolecular Interactions. *Analytical Chemistry* **2010**, *82*, 1221-1227.

[43]. Haes, A. J.; Chang, L.; Klein, W. L.; Van Duyne, R. P., Detection of a Biomarker for Alzheimer's Disease from Synthetic and Clinical Samples Using a Nanoscale Optical Biosensor. *Journal of the American Chemical Society* **2005**, *127*, 2264-2271.

[44]. Guo, L. H.; Chen, G. N.; Kim, D. H. Three-Dimensionally Assembled Gold Nanostructures for Plasmonic Biosensors. *Analytical Chemistry* **2010**, *82*, 5147-5153.

[45]. Gish, D. A.; Nsiah, F.; McDermott, M. T.; Brett, M. J. Localized surface plasmon

resonance biosensor using silver nanostructures fabricated by glancing angle deposition. *Analytical Chemistry* **2007**, *79*, 4228-4232.

[46]. Fujiwara, K.; Watarai, H.; Itoh, H.; Nakahama, E.; Ogawa, N. Measurement of antibody binding to protein immobilized on gold nanoparticles by localized surface plasmon spectroscopy. *Analytical and Bioanalytical Chemistry* **2006**, *386*, 639-644.

[47]. Frederix, F.; Friedt, J. M.; Choi, K. H.; Laureyn, W.; Campitelli, A.; Mondelaers, D.; Maes, G.; Borghs, Biosensing Based on Light Absorption of Nanoscaled Gold and Silver Particles. *G. Analytical Chemistry* **2003**, *75*, 6894-6900.

[48]. Englebienne, P. Use of colloidal gold surface plasmon resonance peak shift to infer affinity constants from the interactions between protein antigens and antibodies specific for single or multiple epitopes. *Analyst* **1998**, *123*, 1599-1603.

[49]. Endo, T.; Yamamura, S.; Nagatani, N.; Morita, Y.; Takamura, Y.; Tamiya, E., Localized surface plasmon resonance based optical biosensor using surface modified nanoparticle layer for label-free monitoring of antigen-antibody reaction. *Science and Technology of Advanced Materials* **2005**, *6*, 491-500.

[50]. Chen, H. H.; Suzuki, H.; Sato, O.; Gu, Z. Z., Biosensing capability of gold-nanoparticle-immobilized three-dimensionally ordered macroporous film. *Applied Physics a-Materials Science & Processing* **2005**, *81*, 1127.

[51]. Anker, J. N.; Hall, W. P.; Lambert, M. P.; Velasco, P. T.; Mrksich, M.; Klein, W. L.; Van Duyne, R. P., Detection and Identification of Bioanalytes with High Resolution LSPR Spectroscopy and MALDI Mass Spectrometry. *Journal of Physical Chemistry C* **2009**, *113*, 5891.

[52]. Endo, T.; Kerman, K.; Nagatani, N.; Hiepa, H. M.; Kim, D. K.; Yonezawa, Y.; Nakano, K.; Tamiya, E., Multiple Label-Free Detection of Antigen-Antibody Reaction Using Localized Surface Plasmon Resonance-Based Core-Shell Structured Nanoparticle Layer Nanochip. *Analytical Chemistry* **2006**, *78*, 6465-6475.

[53]. Haes, A. J.; Hall, W. P.; Chang, L.; Klein, W. L.; Van Duyne, R. P., A localized surface plasmon resonance biosensor: First steps toward an assay for Alzheimer's disease. *Nano Letters* **2004**, *4*, 1029-1034.

[54]. Chang, T. C.; Wu, C. C.; Wang, S. C.; Chau, L. K.; Hsieh, W. H., Using A Fiber Optic Particle Plasmon Resonance Biosensor To Determine Kinetic Constants of Antigen–Antibody Binding Reaction. *Analytical Chemistry* **2013**, *85*, 245-250.

[55]. Law, W. C.; Yong, K. T.; Baev, A.; Prasad, P. N., Sensitivity Improved Surface Plasmon Resonance Biosensor for Cancer Biomarker Detection Based on Plasmonic Enhancement. *ACS Nano* **2011**, *5*, 4858-4864.

[56]. Hall, W. P.; Ngatia, S. N.; Van Duyne, R. P., LSPR Biosensor Signal Enhancement Using Nanoparticle-Antibody Conjugates. *Journal of Physical Chemistry C* **2011**, *115*, 1410-1414.

[57]. Huang, C. J.; Bonroy, K.; Reekman, G.; Verstreken, K.; Lagae, L.; Borghs, G., An on-chip localized surface plasmon resonance-based biosensor for label-free monitoring of antigen-antibody reaction. *Microelectronic Engineering* **2009**, *86*, 2437-2441.

[58]. Guo, L. H.; Kim, D. H., LSPR biomolecular assay with high sensitivity induced by aptamer-antigen-antibody sandwich complex. *Biosensors and Bioelectronics* **2012**, *31*, 567-570.

[59]. Adamczyk, M.; Moore, J. A.; Yu, Z. G., Application of surface plasmon resonance toward studies of low-molecular-weight antigen-antibody binding interactions. *Methods* **2000**, *20*, 319-328.

[60]. Mayer, K. M.; Lee, S.; Liao, H.; Rostro, B. C.; Fuentes, A.; Scully, P. T.; Nehl, C. L.; Hafner, J. H., A label-free immunoassay based upon localized surface plasmon resonance of gold nanorods. *ACS Nano* **2008**, *2*, 687-692.

- [61]. Lee, S.; Mayer, K. M.; Hafner, J. H., Improved Localized Surface Plasmon Resonance Immunoassay with Gold Bipyramid Substrates. *Analytical Chemistry* **2009**, *81*, 4450-4455.
- [62]. Mayer, K. M.; Hao, F.; Lee, S.; Nordlander, P.; Hafner, J. H., A single molecule immunoassay by localized surface plasmon resonance. *Nanotechnology* **2010**, *21*, 255503 (8pp).
- [63]. Chen, S.; Svedendahl, M.; Kall, M.; Gunnarsson, L.; Dmitriev, A., Ultrahigh sensitivity made simple: nanoplasmonic label-free biosensing with an extremely low limit-of-detection for bacterial and cancer diagnostics. *Nanotechnology* **2009**, *20*, 434015 (9pp).
- [64]. Yoo, S. Y.; Kim, D. K.; Park, T. J.; Kim, E. K.; Tamiya, E.; Lee, S. Y., Detection of the Most Common Corneal Dystrophies Caused by BIGH3 Gene Point Mutations Using a Multispot Gold-Capped Nanoparticle Array Chip. *Analytical Chemistry* **2010**, *82*, 1349-1357.
- [65]. Zhou, Y. L.; Xu, Z. N.; Wang, M.; Sun, B.; Yin, H. S.; Ai, S. Y., DNA methyltransferase activity assay based on visible light-activated photoelectrochemical biosensor. *Biosensors and Bioelectronics* **2014**, *53*, 263–267.
- [66]. Zhao, W.W.; Xu, J. J.; Chen, H. Y., Photoelectrochemical DNA Biosensors. *Chemical Reviews* **2014**, *114*, 7421–7441.
- [67]. U. Fano., Sullo spettro di assorbimento dei gas nobili presso il limite dello spettro d'arco. *Nuovo Cimento* **1935**, *12*, 154-161.
- [68]. U. Fano., Effects of Configuration Interaction on Intensities and Phase Shifts. *Physical Review* **1961**, *124*, 1866–1878.

- [69]. Lassiter, J. B.; Sobhani, H.; Fan, J. A.; Kundu, J.; Capasso, F.; Nordlander, P.; Halas, N. J., Fano Resonances in Plasmonic Nanoclusters: Geometrical and Chemical Tunability. *Nano Letters* **2010**, *10*, 3184-3189.
- [70]. Luk'yanchuk, B.; Zheludev, N. I.; Maier, S. A.; Halas, N. J.; Nordlander, P.; Giessen, H.; Chong, C. T., The Fano resonance in plasmonic nanostructures and metamaterials. *Nature Materials* **2010**, *9*, 707-715.
- [71]. Wu, C. H.; Khanikaev, A. B.; Adato, R.; Arju, N.; Yanik, A. A.; Altug, H.; Shvets, G., Fano-resonant asymmetric metamaterials for ultrasensitive spectroscopy and identification of molecular monolayers. *Nature Materials* **2012**, *11*, 69-75.
- [72]. Yanik, A. A.; Cetin, A. E.; Huang, M.; Artar, A.; Mousavi, S. H.; Khanikaev, A.; Connor, J. H.; Shvets, G.; Altug, H., Seeing protein monolayers with naked eye through plasmonic Fano resonances. *Proceedings of the National Academy of Sciences USA* **2011**, *108*, 11784-11789.
- [73]. Cetin, A. E.; Altug, H., Fano Resonant Ring/Disk Plasmonic Nanocavities on Conducting Substrates for Advanced Biosensing. *ACS Nano* **2012**, *6*, 9989-9995.
- [74]. Rahmani, M.; Luk'yanchuk, B.; Hong, M. H., Fano resonance in novel plasmonic nanostructures. *Laser & Photonics Reviews* **2013**, *7*, 329-349.
- [75]. Shen, Y.; Zhou, J. H.; Liu, T. R.; Tao, Y. T.; Jiang, R. B.; Liu, M. X.; Xiao, G. H.; Zhu, J. H.; Zhou, Z. K.; Wang, X. H.; Jin, C. J.; Wang, J. F., Plasmonic gold mushroom arrays with refractive index sensing figures of merit approaching the theoretical limit. *Nature Communications* **2013**, *4*, 2381.
- [76]. Yang, Z. J.; Hao, Z. H.; Lin, H. Q.; Wang, Q. Q., Plasmonic Fano resonances in metallic nanorod complexes. *Nanoscale* **2014**, *6*, 4985-4997.
- [77]. Lee, K. L.; Huang, J. B.; Chang, J. W.; Wu, S. H.; Wei, P. K., Ultrasensitive Biosensors Using Enhanced Fano Resonances in Capped Gold Nanoslit Arrays. *Scientific Reports* **2015**, *5*, 8547.

[78]. Lee, K. L.; You, M. L.; Tsai, C. L.; Hung, C. Y.; Hsieh, S. Y.; Wei, P. K., Visualization of biosensors using enhanced surface plasmon resonances in capped silver nanostructures. *Analyst* **2016**, *141*, 974-980.

[79]. Lee, K. L.; You, M. L.; Tsai, C. H.; Lin, E. H.; Hsieh, S. Y.; Ho, M. H.; Hsu, J. C.; Wei, P. K., Nanoplasmonic biochips for rapid label-free detection of imidacloprid pesticides with a smartphone. *Biosensors and Bioelectronics* **2016**, *75*, 88-95.

[80]. Lee, K. L.; Chang, C. C.; You, M. L.; Pan, M. Y.; Wei, P. K., Enhancing the Surface Sensitivity of Metallic Nanostructures Using Oblique-Angle-Induced Fano Resonances. *Scientific Reports* **2016**, *6*, 33126.

[81]. Sherry, L. J.; Chang, S. H.; Schatz, G. C.; Van Duyne, R. P., Localized Surface Plasmon Resonance Spectroscopy of Single Silver Nanocubes. *Nano Letters* **2005**, *5*, 2034–2038.

[82]. Su, K. H.; Wei, Q. H.; Zhang, X.; Mock, J. J.; Smith, D. R.; Schultz, S., Interparticle coupling effects on plasmon resonances of nanogold particles. *Nano Letters* **2003**, *3*, 1087-1090.

[83]. Sonnichsen, C.; Reinhard, B. M.; Liphardt, J.; Alivisatos, A. P., A molecular ruler based on plasmon coupling of single gold and silver nanoparticles. *Nature Biotechnology* **2005**, *23*, 741-745.

[84]. Hall, W. P.; Ngatia, S. N.; Van Duyne, R. P., LSPR Biosensor Signal Enhancement Using Nanoparticle-Antibody Conjugates, *Journal of Physical Chemistry C* **2011**, *115*, 1410-1414.

[85]. Juan, M. L.; Righini, M.; Quidant, R., Plasmon nano-optical tweezers. *Nature Photonics* **2011**, *5*, 349-356.

[86]. Liang, Z. Q.; Sun, J.; Jiang, Y. Y.; Jiang, L.; Chen, X. D., Plasmonic Enhanced Optoelectronic Devices. *Plasmonics* **2014**, *9*, 859-866.

- [87]. Cooper, M. A., Optical biosensors in drug discovery. *Nature reviews Drug discovery* **2002**, *1*, 515-528.
- [88]. Pires, N. M. M.; Dong, T.; Hanke, U.; Hoivik, N., Recent Developments in Optical Detection Technologies in Lab-on-a-Chip Devices for Biosensing Applications. *Sensors* **2014**, *14*, 15458-15479.
- [89]. Malinsky, M. D.; Kelly, K. L.; Schatz, G. C.; Van Duyne, R. P., Chain length dependence and sensing capabilities of the localized surface plasmon resonance of silver nanoparticles chemically modified with alkanethiol self-assembled monolayers. *Journal of the American Chemical Society* **2001**, *123*, 1471-1482.
- [90]. Larsson, E. M.; Alegret, J.; Kall, M.; Sutherland, D. S., Sensing characteristics of NIR localized surface plasmon resonances in gold nanorings for application as ultrasensitive biosensors. *Nano Letters* **2007**, *7*, 1256-1263.
- [91]. Chen, H. J.; Kou, X. S.; Yang, Z.; Ni, W. H.; Wang, J. F., Shape- and size-dependent refractive index sensitivity of gold nanoparticles. *Langmuir* **2008**, *24*, 5233-5237.
- [92]. Ueno, K.; Juodkazis, S.; Shibuya, T.; Yokota, Y.; Mizeikis, V.; Sasaki, K.; Misawa, H., Nanoparticle plasmon-assisted two-photon polymerization induced by incoherent excitation source. *Journal of the American Chemical Society* **2008**, *130*, 6928-6929.
- [93] Verellen, N.; Sonnefraud, Y.; Sobhani, H.; Hao, F.; Moshchalkov, V. V.; Van Dorpe, P.; Nordlander, P.; Maier, S. A., Fano Resonances in Individual Coherent Plasmonic Nanocavities. *Nano Letters* **2009**, *9*, 1663–1667.
- [94] Luk'yanchuk, B.; Zheludev, N. I.; Maier, S. A.; Halas, N. J.; Nordlander, P.; Giessen, H.; Chong, C. T., The Fano Resonance in Plasmonic Nanostructures and Metamaterials. *Nature Materials* **2010**, *9*, 707–715.
- [95] Halas, N. J.; Lal, S.; Chang, W.-S.; Link, S.; Nordlander, P., Plasmons in Strongly

Coupled Metallic Nanostructures. *Chemical Reviews* **2011**, *111*, 3913–3961.

[96] Hentschel, M.; Saliba, M.; Vogelgesang, R.; Giessen, H.; Alivisatos, A. P.; Liu, N., Transition from Isolated to Collective Modes in Plasmonic Oligomers. *Nano Letters* **2010**, *10*, 2721–2726.

[97] Lassiter, J. B.; Sobhani, H.; Fan, J. A.; Kundu, J.; Capasso, F.; Nordlander, P.; Halas, N. J., Fano Resonances in Plasmonic Nanoclusters: Geometrical and Chemical Tunability. *Nano Letters* **2010**, *10*, 3184–3189.

[98] Rahmani, M.; Luk'yanchuk, B.; Hong, M. H., Fano Resonance in Novel Plasmonic Nanostructures. *Laser & Photonics Reviews* **2013**, *7*, 329–349.

[99] Wang, P.; Wang, Y.; Yang, Z.; Guo, X.; Lin, X.; Yu, X.-C.; Xiao, Y.-F.; Fang, W.; Zhang, L.; Lu, G.; Gong, Q.; Tong, L., Single-Band 2-nm-Line-Width Plasmon Resonance in a Strongly Coupled Au Nanorod. *Nano Letters* **2015**, *15*, 7581–7586.

[100] Haegglund, C.; Zeltzer, G.; Ruiz, R.; Wangperawong, A.; Roelofs, K. E.; Bent, S. F., Strong Coupling of Plasmon and Nanocavity Modes for Dual-Band, Near-Perfect Absorbers and Ultrathin Photovoltaics. *ACS Photonics* **2016**, *3*, 456–463.

[101] Christ, A.; Tikhodeev, S. G.; Gippius, N. A.; Kuhl, J.; Giessen, H., Waveguide-Plasmon Polaritons: Strong Coupling of Photonic and Electronic Resonances in a Metallic Photonic Crystal Slab, *Physical Review Letters* **2003**, *91*, 183901.

[102] Christ, A.; Zentgraf, T.; Kuhl, J.; Tikhodeev, S. G.; Gippius, N. A.; Giessen, H., Optical Properties of Planar Metallic Photonic Crystal Structures: Experiment and Theory, *Physical Review B* **2004**, *70*, 125113.

[103] Linden, S.; Rau, N.; Neuberth, U.; Naber, A.; Wegener, M.; Pereira, S.; Busch, K.; Christ, A.; Kuhl, J., Near-Field Optical Microscopy and Spectroscopy of One-Dimensional Metallic Photonic Crystal Slabs, *Physical Review B* **2005**, *71*, 245119.

- [104] Zhang, X. P.; Sun, B. Q.; Friend, R. H.; Guo, H. C.; Nau, D.; Giessen, H., Metallic Photonic Crystals Based on Solution-Processible Gold Nanoparticles, *Nano Letters* **2006**, *6*, 651–655.
- [105] Zhang, X. P.; Sun, B. Q.; Hodgkiss, J. M.; Friend, R. H., Tunable Ultrafast Optical Switching via Waveguided Gold Nanowires, *Advanced Materials* **2008**, *20*, 4455–4459.
- [106] Nau, D.; Seidel, A.; Orzekowsky, R. B.; Lee, S.-H.; Deb, S.; Giessen, H., Hydrogen Sensor Based on Metallic Photonic Crystal Slabs, *Optics Letters* **2010**, *35*, 3150–3152.
- [107] Zeng, P.; Cadusch, J.; Chakraborty, D.; Smith, T. A.; Roberts, A.; Sader, J. E.; Davis, T. J.; Gomez, D. E., Photoinduced Electron Transfer in the Strong Coupling Regime: Waveguide–Plasmon Polaritons, *Nano Letters* **2016**, *16*, 2651–2656.
- [108] Alonso-Gonzalez, P.; Schnell, M.; Sarriugarte, P.; Sobhani, H.; Wu, C. H.; Arju, N.; Khanikaev, A.; Golmar, F.; Albella, P.; Arzubiaga, L.; Casanova, F.; Hueso, L. E.; Nordlander, P.; Shvets, G.; Hillenbrand, R., Real-Space Mapping of Fano Interference in Plasmonic Metamolecules. *Nano Letters* **2011**, *11*, 3922–3926.
- [109] Coenen, T.; Schoen, D. T.; Mann, S. A.; Rodriguez, S. R. K.; Brenny, B. J. M.; Polman, A.; Brongersma, M. L., Nanoscale Spatial Coherent Control over the Modal Excitation of a Coupled Plasmonic Resonator System. *Nano Letters* **2015**, *15*, 7666–7670.
- [110] Lassiter, J. B.; Sobhani, H.; Knight, M. W.; Mielczarek, W. S.; Nordlander, P.; Halas, N. J., Designing and Deconstructing the Fano Lineshape in Plasmonic Nanoclusters. *Nano Letters* **2012**, *12*, 1058–1062.
- [111] Frimmer, M.; Coenen, T.; Koenderink, A. F., Signature of a Fano Resonance in a Plasmonic Metamolecule’s Local Density of Optical States. *Physical Review Letters* **2012**, *108*, 077404.
- [112] Yu, H.; Sun, Q.; Ueno, K.; Oshikiri, T.; Kubo, A.; Matsuo, Y.; Misawa, H., Exploring Coupled Plasmonic Nanostructures in the Near field by Photoemission Electron

Microscopy. *ACS Nano* **2016**, *10*, 10373–10381.

[113] Yu, H.; Sun, Q.; Yang, J. H.; Ueno, K.; Oshikiri, T.; Kubo, A.; Matsuo, Y.; Gong, Q. H.; Misawa, H., Near-Field Spectral Properties of Coupled Plasmonic Nanoparticle Arrays. *Optics Express* **2017**, *25*, 6883–6894.

[114]. Zhu, A. W.; Luo, Y. P.; Tian Y., Plasmon-Induced Enhancement in Analytical Performance Based on Gold Nanoparticles Deposited on TiO₂ Film. *Analytical Chemistry* **2009**, *81*, 7243–7247.

[115]. Zhao. W. W.; Tian, C. Y.; Xu, J. J.; Chen, H. Y.; The coupling of localized surface plasmon resonance-based photoelectrochemistry and nanoparticle size effect: towards novel plasmonic photoelectrochemical biosensing. *Chemical Communications* **2012**, *48*, 895–897.

[116]. Da, P. M.; Li, W. J.; Lin, X.; Wang, Y. C.; Tang, J.; Zheng, G. F. Surface Plasmon Resonance Enhanced Real-Time Photoelectrochemical Protein Sensing by Gold Nanoparticle Decorated TiO₂ Nanowires. *Analytical Chemistry* **2014**, *86*, 6633–6639.

Chapter 2

Near-field spectrum measurement of strongly coupled waveguide-plasmon modes by photoelectrochemistry

2.1 Introduction

To elucidate the influence of near-field coupling on PEC response, a suitable plasmonic system with near-field coupling needs to be employed. A simple coupled plasmonic system such as nanogap dimer Au particles exhibit only one peak in the near-field spectrum and PEC spectrum. Even if the shape of PEC spectrum corresponds to that of the near-field spectrum, it is difficult to conclude that the near-field spectrum is completely reproduced by the PEC spectrum because the physical parameter of y-axis of each spectrum differs from each other. If there are multiple peaks in the near-field spectrum and the PEC spectrum completely responds to the near-field spectrum, the difference in the spectrum shape can be discussed as a relative comparison even if the physical parameter of y-axis is different.

Plasmonic strong coupling system is promising to be used for exploring the influence of near-field coupling on the PEC response because the coupled plasmonic system has multiple peaks and near-field intensity of each peak can be modulated by detuning of strong coupling. Here, I employed Au nanogratings (Au-NGs) loaded titanium dioxide (TiO_2) waveguide structures showing strong coupling due to the interaction of the evanescent wave of the waveguide and LSPR modes, resulting in multiple peaks in far-field and near-field spectra.

In this chapter, periodic Au-NGs/ TiO_2 structures with various pitch sizes have been fabricated and their far-field and near-field spectral properties as well as PEC responses have been studied. The near-field spectra also show multiple peaks due to the strong coupling between waveguide modes and LSPR. Importantly, the near-field intensity of

multiple peaks can be tuned by changing the pitch size of the Au-NGs to compare the shape difference between near-field and PEC spectra.

Prior starting the experimental section of this chapter, the photocatalytic properties of TiO_2 and metallic nanostructured TiO_2 will be presented to give a better understanding of the plamon-induced photocurrent generation mechanism. TiO_2 has been extensively applied for photocatalytic fuel generation^[1-3] and organic pollution degradation^[4-14] after the photocatalytic splitting of water under ultraviolet (UV) light irradiation, which was discovered by A. Fujishima and K. Honda in 1972^[15] as shown in Figure 2.1. Under the irradiation of UV light, the electrons and holes are generated and the electrons reduce water to form H_2 at Pt electrode and the holes oxide water to form O_2 at TiO_2 electrode.

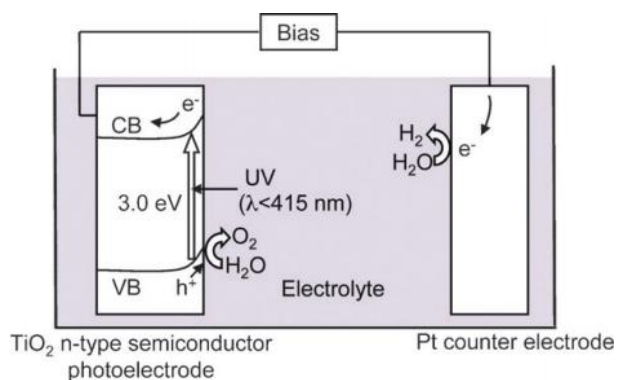


Figure 2.1 Honda-Fujishima effect-water splitting using a TiO_2 photoelectrode.^[15]

Lots of materials have been synthesized and found to display photocatalytic activity including metal oxides (such as TiO_2 ^[1-16], ZnO ^[17-19], SnO_2 ^[20], VO_2 ^[21], ZrO_2 ^[22,23], Ta_2O_5 ^[24-26], Nb_2O_5 ^[27], SrTiO_3 ^[28-35], BaTiO_3 ^[36], CaTiO_3 ^[37] etc.) and nonoxide photocatalysts (GaN ^[38,39], InP ^[40], ZnS ^[41], Ge_3N_4 ^[42-44], Ta_3N_5 ^[45], CdS ^[16], CdSe ^[46] etc.). However, TiO_2 remains the most studied among these materials due to its chemical stability, low cost, non-toxicity, and accessible band gap. Lots of researches have been done about different types of TiO_2 .^[47-50] There are mainly four phase structures of TiO_2

found in nature known as anatase, rutile, brookite, and TiO₂(B) as shown in Figure 2.2 and Table 2.1.^[50] Generally, rutile is the most stable phase thermodynamically especially for large TiO₂ particles and can be normally obtained from the other three polymorphs by high temperature annealing at elevated temperatures. The phase transformations are: anatase → rutile; brookite → anatase → rutile and TiO₂(B) → anatase → rutile.

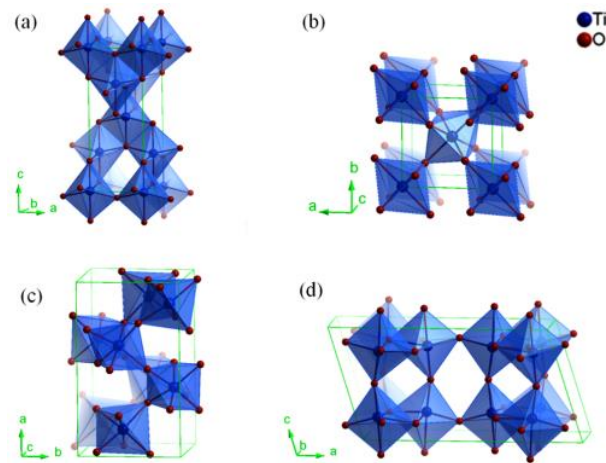


Figure 2.2 Crystalline structures of TiO₂ in four different phases: (a) anatase, (b) rutile, (c) brookite, and (d) TiO₂(B).^[50]

Table 2.1. Four main polymorphs of TiO₂ and their structural parameters.^[50]

crystal form	crystal system	space group	unit cell parameters			
			<i>a</i> /nm	<i>b</i> /nm	<i>c</i> /nm	<i>β</i> /deg
anatase	tetragonal	<i>I</i> ₄ <i>1</i> / <i>amd</i>	0.379		0.951	
rutile	tetragonal	<i>P</i> ₄ <i>2</i> / <i>mmm</i>	0.459		0.296	
brookite	orthorhombic	<i>Pbca</i>	0.918	0.545	0.515	
TiO ₂ (B)	monoclinic	<i>C</i> ₂ / <i>m</i>	1.216	0.374	0.651	107.3

In the recent four decades, rutile and anatase are mostly investigated. Because only about 5% of the solar light (UV region as shown in Figure 2.3) can be absorbed by the TiO₂ due to the wide band gap of TiO₂ (3.0 eV for rutile and 3.2 eV for anatase),^[51] solar energy in visible, near infrared (IR) and IR region is hardly harvested. Researchers tried a lot of efforts to promote the photoactivity of TiO₂ to a longer

wavelength via various approaches such as metal ion doping (Cr, Ga, Ni, Sn, Eu, Sb, V, Mn, Fe, Ag, Pt, etc.),^[52-59] nonmetal-ion doping (N, C, F, P, S, H, B, Br, Si, etc.),^[60-71] metal/nonmetal-ion codoping (Ce/C, Ce/I, Ce/N, Ce/B, Fe/C, Fe/N, Bi/C, Bi/N, Bi/S, Ni/B, Ni/N, La/S, La/I, W/N, Pt/N, Pd/N, etc.),^[72-86] organic dye sensitization^[87-88] and many other methods.^[89]

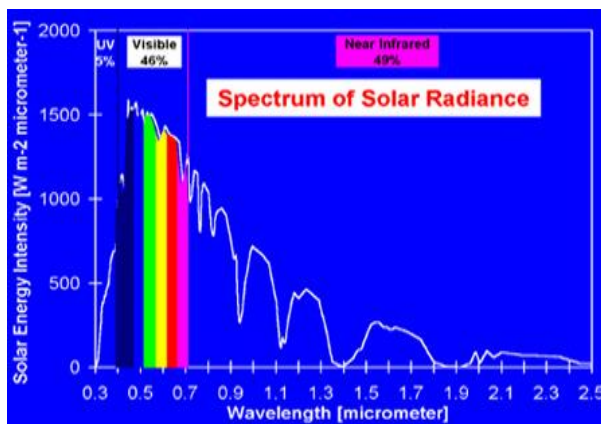


Figure 2.3 The radiation energy distribution from the sun by wavelength and photon energy. http://solarcellcentral.com/solar_page.html.

In the past decade, the surface plasmon resonance of metallic nanoparticles incorporated with semiconductor has been investigated to improve the efficiency of photocatalytic processes.^[90-108] The photocatalytic production of hydrogen is particularly interesting for its ability to store the solar energy in chemical bonds, which can be released later without producing harmful byproducts. Many photocatalysis properties have been found to benefit from LSPR of various metallic nanostructures. How does the LSPR improve the efficiency of photocatalytic processes? Typically, photocatalysis consists of a series of working steps. In brief, the metal nanostructures will first absorb and scatter the incoming photons and produce an extremely enhanced local electric field. As a result, active charge carriers are generated and then separated. To date, two main mechanisms have been approved to explain the plasmon-induced or enhanced water oxidation and splitting: plasmon-induced charge separation and electron transfer, near-field enhancement.

Charge separation and electron transfer mechanism is the most extensively accepted theory to explain the plasmon-induced water oxidation and splitting. Tatsuma et al. observed that the incident photon to current efficiency (IPCE) action spectrum under visible light illumination upon loading Au or Ag nanoparticles into TiO₂ sol gel films accords well with the absorption spectrum of surface plasmon. They proposed that the surface plasmon resonance excites electrons in Au or Ag, which are then transferred to the conduction band of the adjacent TiO₂, as shown schematically in Figure 2.4 (a).^[92] This is similar to that of a dye-sensitized solar cell. Charge separation and electron transfer mechanism was then proved by Furube et al. using femtosecond transient absorption spectroscopy with an infrared probe as shown in Figure 2.4 (b).^[93] Laser pulses (duration: 150 fs, wavelength: 550 nm) were used to excite LSPR in Au nanoparticles deposited on TiO₂ substrate, meanwhile, the transient absorption of TiO₂ at 3500 nm was simultaneously monitored. They found that electron generation and transfer completed within 50 fs with an efficiency around 40% from plasmon-excited Au nanoparticles into TiO₂ in comparison with ruthenium N3 dye on TiO₂, which is known to have a carrier injection efficiency of almost 100%.

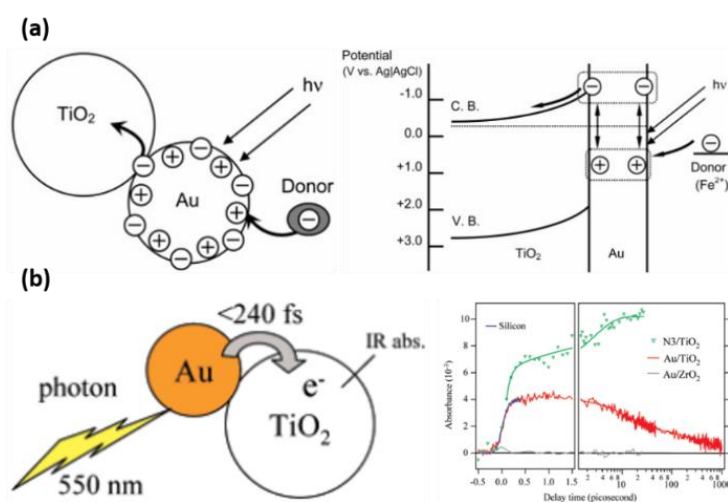


Figure 2.4 (a) Schematic illustration of the proposed plasmon-induced charge separation and electron transfer mechanism.^[92] (b) Schematic diagram of a gold nanoparticles attaching on a TiO₂ substrate, also indicating the revealed plasmon-induced charge separation and electron transfer.^[93]

As mentioned in chapter 1, the metallic nanostructures can generate extremely intense local electric field enhancement near the surface of the nanostructures. Ample evidences have proved the existence of plasmonic “hot spots” with high local near-field enhancement, which can reach as much as 1000 times higher than that of the incident electric field not only by the numerical simulations as shown in Figure 2.5 (a) and 2.6 (a),^[101,102] but also the experimental observations, such as EELS, CL and PEEM as shown in chapter 1. The photocurrent generation is enhanced after depositing Au or Ag nanoparticles on the surface of TiO₂ substrate as shown in 2.5 (b) and 2.6 (c), respectively. Meanwhile, hydrogen and oxygen production rates are also boosted as shown in Figure 2.6 (b). Stephen et al. believed that in these “hot spots” regions, the electron-hole pair generation rate is 1000 times that of the incident electromagnetic field. Therefore, an increased amount of photo-induced photocurrent is generated. They also found that this local near-field enhancement mechanism highly relies on the presence of defect states in the TiO₂. The photocurrent is enhanced with Au nanoparticles in doped TiO₂ with N- and F-impurities. However, there will be no photocurrent generation for undoped TiO₂ prepared by the sol-gel method with or without nanoparticles. The light absorption below the band gap of the semiconductor due to the defect is necessary.

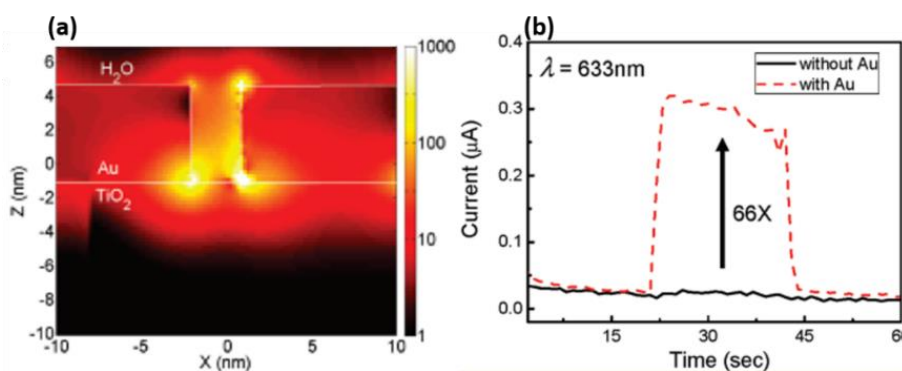


Figure 2.5 (a) Simulated electric field intensity at the interface of Au-TiO₂. (b) Photocurrent obtained from with (red) and without (black) Au decorated TiO₂ photoelectrodes irradiated with a monochromatic light at 633 nm for 22 s.^[101]

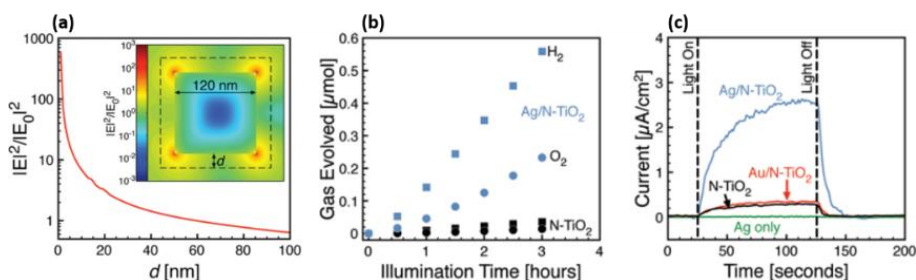


Figure 2.6 (a) Calculated average electric field enhancement around a silver cube with an edge length of 120 nm as a function of the distance d from the cube. Inset: Simulated local enhancement of the electric field of a 120 nm Ag cube in water. (b) H_2 and O_2 production with visible light irradiation on N-TiO₂ (black) and Ag/N-TiO₂ (blue). (c) Photocurrent responses upon illumination with a broadband visible light source responding to the light on and off.^[102]

The external quantum efficiency (EQE, same as IPCE) and internal quantum efficiency (IQE) spectra are two important parameters to evaluate the performance and quality of various photosensitive devices including solar cells, charge-coupled device (CCD), photodetector and so on. The IQE is determined by correcting the EQE for the fraction of incident photons absorbed by the device. The IQE gives the photon-to-charge conversion efficiency and is always larger than the EQE. Typically, the IQE action spectrum shows no wavelength dependence that corresponds to the absorption spectrum of dye sensitizer driving the electron transfer.^[109] However, Grancini et al. reported wavelength-dependent IQE of polymer solar cells based on PCPDTBT:PC60BM blends.^[110] The IQE increased monotonically (by a factor of two) with increasing excitation energies. They found that excitons can create both relaxed charge transfer states and free charge carriers, which are depended on the excess energy. Due to much stronger coupling between high-energy singlets and hot charge transfer states with high-energy excitation, the high-lying singlet states can be converted into hot charge transfer states with higher generation efficiency. On the contrast, the relaxed charge transfer state has much lower photocurrent generation efficiency. Hot charge

transfer states in charge carrier generation played an important role in wavelength-dependent IQE spectrum.

However, Scharber and Armin et al. commented that the IQE spectrum measured by Grancini et al. is not accurate and claimed that the IQE is independent of the wavelength across the absorption spectrum of the blend because the accurate determination of IQE is not easy.^[111,112] After that, Grancini et al. replied these comments and acknowledged the difficulty in obtaining accurate IQE due to interference and parasitic absorptions.^[113] They further made a new planar device with simplified in terms of optical effects and demonstrated that the IQE of the planar device also shows wavelength-dependence.

Recently, some researchers have reported that the IQE action spectra of some plasmonic devices are strongly wavelength dependent with the plasmon band.^[94, 114-120] Misawa et al. reported the IQE spectrum of Au nanorods loaded TiO₂ photoelectrode is highly dependent on wavelength as shown in Figure 2.7. Figure 2.7 (a) shows the SEM image of Au nanorods loaded on TiO₂ substrate and corresponding extinction spectra under different polarized light. Two apparent peaks can be observed in the IQE spectrum as shown in Figure 2.7 (b), which are in good accordance with the extinction spectra as shown as blue curve in Figure 2.7 (a). They attributed this to the nonlinear photo-induced electron transfer from Au nanorods to TiO₂ photoelectrode induced by the combinations of antenna effects and giant electromagnetic field enhancement effects.

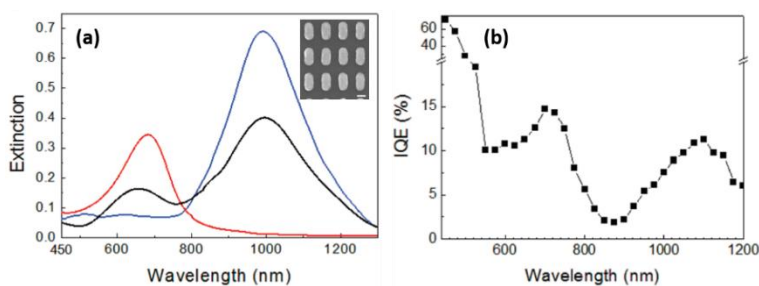


Figure 2.7 (a) Extinction spectra of the Au nanorods loaded on TiO₂ substrate in water. Black: under irradiation of nonpolarized light. Red and blue: minor-axis direction (T-

mode) and major-axis direction (L-mode) under irradiation of linearly polarized light, respectively. (b) The corresponding highly wavelength dependent IQE spectrum under irradiation of nonpolarized light.^[94]

Park et al. reported the combined influence of dye molecules and surface plasmons on hot electron flows detected on Au/TiO₂ nanodiodes generated by the absorption of photons as shown in Figure 2.8. Figure 2.8 (a) shows the schematic of a Au/TiO₂ diode. Figure 2.8 (b) shows the corresponding three IPCE spectra of three different samples. There is no effect (blue triangular curve), only surface plasmons (black squared curve) and the combined dye molecules (merbromin) and surface plasmons (red circled curve), respectively. The IQE spectra of only dye molecules effect (black squared curve) and combined influence of dye molecules and surface plasmons (red squared curve) are shown in Figure 2.8 (c). It should be noticed that the IQE spectrum of merbromin deposited continuous Au film (black squared curve in Figure 2.8 (c)) shows no wavelength dependence. However, the combined influence of dye molecules and surface plasmons (red squared curve) shows apparent wavelength dependence, which is also in good accordance with the IPCE spectrum in Figure 2.8 (b). They attributed the enhanced IQE of dye molecules modified Au islands/TiO₂ diodes to an additional pathway for generating hot electron flows between the dye molecules and surface plasmons.^[115,116]

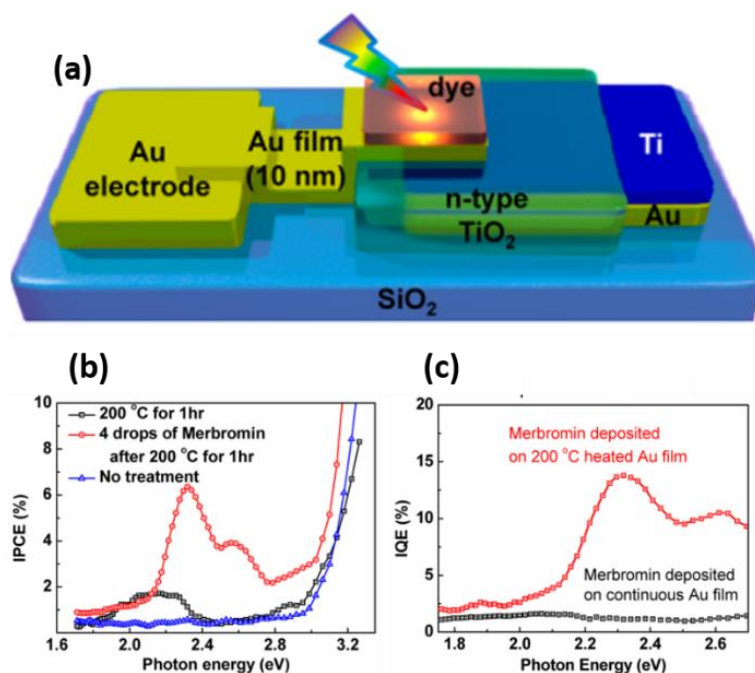


Figure 2.8 (a) Scheme of a Au/TiO₂ diode to detect hot electron flow driven by the coupling of dye molecules and surface plasmons. (b) IPCE spectra after surface treatments (blue line, untreated Au/TiO₂ diode; black line, IPCE measured on a surface modified Au/TiO₂ diode after heating at 200 °C for 1 h; red line, merbromin adsorbed on a Au/TiO₂ diode after heating at 200 °C for 1 h). (c) IQE of the merbromin adsorbed on Au/TiO₂ diodes after annealing at 200 °C, and that of the merbromin on the continuous Au/TiO₂ diodes.^[115]

Moskovits et al. reported a stable, wholly plasmonic photovoltaic device in which photon absorption and carrier generation take place exclusively in the plasmonic metallic nanostructures. Figure 2.9 (a) and Figure 2.9 (b) show the schematic of the plasmonic photovoltaic device and the corresponding SEM image, respectively. Figure 2.9 (c) shows the absorption spectrum of gold nanorod arrays capped with 10 nm ALD-deposited TiO₂ film, which is measured by separating the absorbance from the transmittance and both specular and diffuse reflectance in an integrating sphere. Figure 2.9 (d) and Figure 2.9 (e) show the IPCE and IQE spectra with 10 nm (orange), 30 nm (blue), and 50 nm (purple) ALD-deposited TiO₂ film, respectively. Apparent peaks accord with absorbance spectrum can also be observed. They attributed wavelength-

dependent IQE of plasmonic photovoltaic device to two different types of absorbance, one absorbance is due to the direct single-electrons absorptions, i.e. band to band absorptions in the TiO_2 and interband transitions in the gold, another absorbance is due to the surface plasmon.

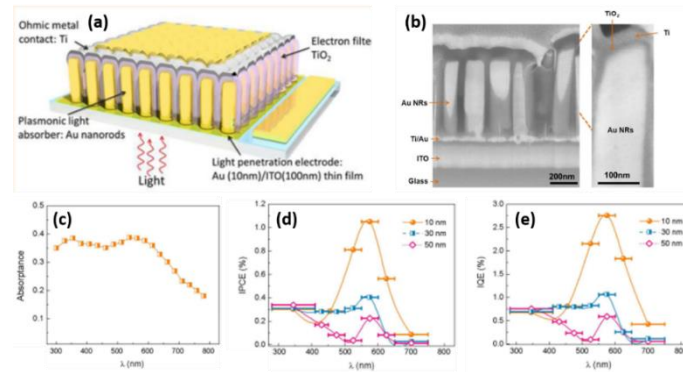


Figure 2.9 (a). Plasmonic photovoltaic device. (b). Cross sectional SEM micrograph of plasmonic photovoltaic device. (c) The absorption spectrum of plasmonic photovoltaic device. (d) IPCE spectra of devices fabricated with TiO_2 layers of varying thickness: (i) 10, (ii) 30, and (iii) 50 nm. (e) The corresponding IQE spectra.^[118]

Kim et al. reported that an Au/TiO_2 metallic-semiconductor photonic crystal (MSPhC) device for photochemical energy conversion showed a sub-bandgap photoresponse centered at the surface plasmon polariton (SPP) resonant wavelength of this device as shown in Figure 2.10 (a) and (b). The electric field distribution at cross-section of MSPhC nano-cavity is shown in Figure 2.10 (c), which shows SPP at the Au/TiO_2 interface along the cavity side wall at 590 nm. The measured (blue solid line) and calculated (blue dashed curve) reflectance spectra and normalized photoresponse of MSPhC from 400 nm to 800 nm are shown in Figure 2.10 (d). The Fowler's theory, which has been widely used to model the Schottky internal photoemission.^[122] The IQE of a Schottky device, such as Au/TiO_2 MSPhC, could be fitted to Fowler's equation, as shown by the black curve in Figure 2.10 (e). However, the calculated IQE spectrum is deviated from the measured IQE spectrum, which is shown as symbols and blue dash

line in Figure 2.10 (e). In fact, various experimental results have also shown that the applicability of Fowler's theory is limited when plasmon resonance exists.^[123-125] All these evidences predict that the surface plasmon induced hot electron transfer is different from the electron transfer and charge separation induced by only photon absorption, e.g. semiconductor, dye molecules et al. However, detailed information and exploration need further investigation.

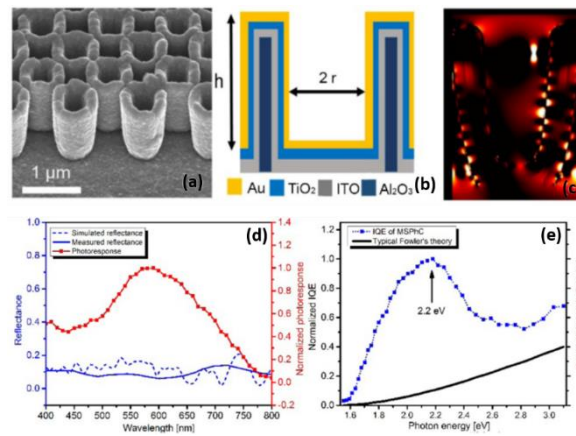


Figure 2.10 (a). Schematic of Au/TiO₂ metallic-semiconductor photonic crystal (MSPhC) device. (a) Focused ion beam (FIB) photo of MSPhC viewed at 30° angle. (b) The crosssection view of MSPhC structure. r and d represent the radius (250 nm) and depth (1 μm) of the nano-cavity, respectively. (c) Electric field distribution at cross-section of nano-cavity, obtained from FDTD simulation, which shows SPP at the Au/TiO₂ interface along the cavity side wall at 590 nm. (d) Measured (blue solid line) and calculated (blue dashed curve) reflectance spectra and normalized photoresponse of MSPhC from 400 nm to 800 nm. The low reflectance from UV-Vis measurement and FDTD simulation indicates high absorption in this range. Value of photoresponse is normalized against the highest value at 590 nm. (e) Normalized IQE spectrum of MSPhC (symbols and blue dash line), which is normalized against the value at 2.21 eV (560 nm). The IQE is calculated with the measured photocurrent and absorption by the Au layer. Example of IQE curve (black solid line) based on Fowler's theory with barrier height of 1.53 eV and arbitrary fitting constant.^[120]

I hypothesized that the plasmon induced local near-field enhancement plays a significant role in wavelength-dependent IQE of plasmonic devices. Due to the localization of surface plasmon, for example, the giant electromagnetic field enhancement is normally localized at the sharp corners of Au nanosquares.^[101,102] In Au nanostructured TiO₂ induced water oxidation and photocurrent generation systems, the surface plasmon excited electrons are transferred to the conduction band of TiO₂ and the remained holes are trapped to the surface states of TiO₂ at the restricted nanospace near the Au/TiO₂/water interface. In general, IQE spectrum should be wavelength independent if the photocurrent generation is triggered only by the light absorption because the efficiency is normalized by the absorbed photons. However, the plasmon-induced water oxidation efficiency should be influenced not only by the light absorption but also by the local near-field intensity because the reaction proceeds via multi-electron transfers only at the restricted nanospace. Namely, the IQE spectrum in the plasmon-induced photocurrent generation using water as an electron source should correspond to the near-field spectrum.

To explore the near-field enhancement effect on the plasmon-induced photocurrent generation and water oxidation, a coupled plasmonic system, strongly coupled waveguide-LSPR modes are explored by photocurrent generation measurement and numerical near-field spectral simulation. The relationship between the near-field and IQE spectra is analyzed and compared in detail in this chapter.

2.2 Experimental details

2.2.1 Preparation of periodic gold nanogratings patterned titanium dioxide photoelectrode

The glass substrates were rinsed with acetone, methanol, and deionized water in an ultrasonic bath for 5 minutes, respectively. The glass substrates were then dried with compressed nitrogen. After that, TiO₂ thin film with thickness of 250 nm was deposited on one side of glass substrate using a commercial hot-wall flow-type atomic layer

deposition (ALD) reactor (SUNALETM R series, Picosun, Finland). The deposition of TiO₂ thin film was processed by alternating exposures of TiCl₄ and subsequent deionized water vapor at a process temperature of 300°C with nitrogen as a precursor carrier and purge gas at a pressure of 1.6 kPa layer by layer. The TiO₂ deposited silica glass substrate was then rinsed with acetone, methanol, and deionized water in an ultrasonic bath for 5 minutes separately again and dried with compressed nitrogen. After that, periodic Au-NGs were fabricated on the surface of TiO₂ substrate. A conventional copolymer resist (ZEP-520A; Zeon Chemicals, Louisville, USA) diluted with ZEP-A (Zeon Chemicals) thinner (volumetric ratio 1:1) was spin-coated on the 250 nm TiO₂ thin film (1000 rpm for 10 s, and 4000 rpm for 90 s), and prebaked on a hot plate for 2 min at 150°C. Electron beam lithography (EBL, ELS-F125; Elionix, Tokyo, Japan) was conducted at an acceleration voltage of 125 kV, a beam current of 3 nA and a dose of 512 μC cm⁻² by skip scan method. After the development by 4-Methyl-2-pentanone (methyl isobutyl ketone, Wako) for 60 s, 1 nm-thick titanium as an adhesion layer was deposited onto the substrate followed by the deposition of a 50 nm-thick Au film via sputtering (MPS-4000, ULVAC). Finally, the residual resist was removed by a lift-off process in an ultrasonic bath of anisole (Methoxybenzene, Wako) for 5 minutes, and subsequently rinsed with acetone, methanol, and deionized water in an ultrasonic bath for 5 minutes, respectively.

2.2.2 Photoelectrochemical measurements

Figure 2.11 shows the detailed information for PEC measurements. Good Ohmic contact and electron conductivity are achieved by pasting In–Ga alloy (4:1 in weight ratio) film and a thin layer of silver on the backside of the Au-NGs/TiO₂ substrate before measurement. A platinum wire, a saturated calomel electrode and Au-NGs/TiO₂ sample utilized as counter electrode, reference electrode and working electrode, were connected to an electrochemical analyzer (ALS/CH Instruments 852C, ALS) to create a three-electrode system. An aqueous KClO₄ (0.1 mol/L in water) solution was used as

the supporting electrolyte solution. A xenon lamp used as a light source (Model 66870, Newport), monochromatic light with full width at half-maximum (fwhm) of less than 7 nm was employed to obtain the EQE action spectrum. The working potential was set to +0.3 V versus the reference electrode during the photocurrent measurement.

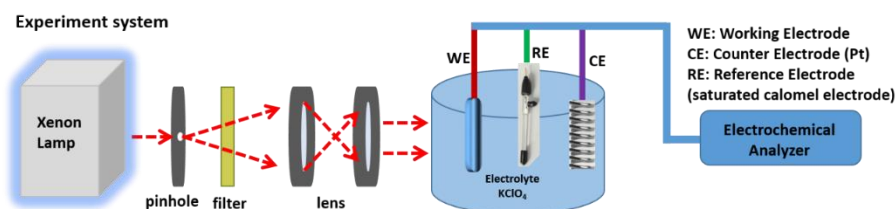


Figure 2.11 Schematic of PEC measurements. Xenon lamp was employed as light source. Au-NGs/TiO₂, Pt wire and saturated calomel electrode were employed as working electrode, counter electrode and reference electrode, respectively.

2.3 Results and discussions

2.3.1 Structural geometries of periodic gold nanogratings patterned titanium dioxide photoelectrode

The schematic illustration of periodic Au-NGs/TiO₂ structure is shown in the diagram of Figure 2.12 (a). The samples consist of variable periodic Au-NGs, which are deposited on the top of TiO₂ waveguide film. As a consequence, the Au-NGs excite LSPR mode (with resonance energy of E_p) and TiO₂ waveguide film supports waveguide mode (with resonance energy of E_w) when the incident light is polarized perpendicular to the Au-NGs length as shown in Figure 2.12 (b). The strong coupling between these two modes will occur by tuning the pitch size of periodic Au-NGs, leading to the formation of strongly coupled hybrid states (upper branch (P₊) and lower branch (P₋), separated by $\hbar\Omega$ in energy). The typical top-viewed SEM image of the periodic arrays of Au-NGs/TiO₂ structure with 300 nm pitch size was shown in figure 2.13.

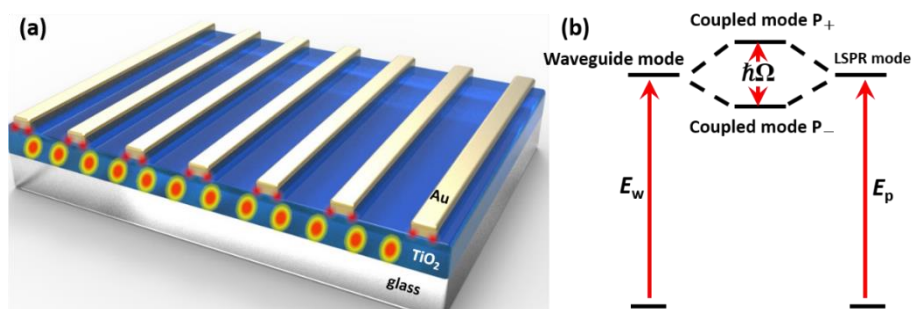


Figure 2.12 (a) A schematic illustration of periodic Au-NGs of 100 nm in width and 50 nm in height deposited on 250 nm TiO₂ film. The Au-NGs excite LSPR mode and TiO₂ film supports waveguide mode when the incident light is polarized perpendicular to the Au-NGs length. (b) The formation of strongly coupled waveguide-LSPR coupling modes, upper branch (P₊) and lower branch (P₋) with splitting energy of $\hbar\Omega$ deriving from uncoupled waveguide (E_w) and plasmon (E_p) modes, respectively.

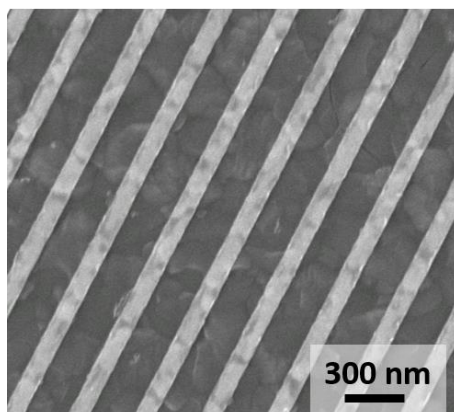


Figure 2.13 Typical top-viewed SEM images of the Au-NGs/TiO₂ structure with 300 nm pitch size. The scale bars represent 300 nm.

2.3.2 Experimental extinction properties of periodic gold nanogratings patterned titanium dioxide photoelectrode

The extinction spectra were measured to investigate the far-field spectrum properties of the Au-NGs/TiO₂. Figure 2.14 shows extinction spectra evolution of the periodic Au-NGs/TiO₂ structures in water (in accordance with the photocurrent measurement due to the samples were immersed into KClO₄ electrolyte solution) with increasing

pitch size from 200 nm to 400 nm. The incident light is polarized perpendicular to the Au-NGs length. Only one peak can be observed corresponding to LSPR mode of periodic Au-NGs with 200 nm and 225 nm pitch sizes, demonstrating the absence of waveguide mode. Starting with a pitch size of 250 nm, three peaks can be observed, and the peaks show spectrum shift with increasing of pitch size. Detailed discussions will be introduced in the next section.

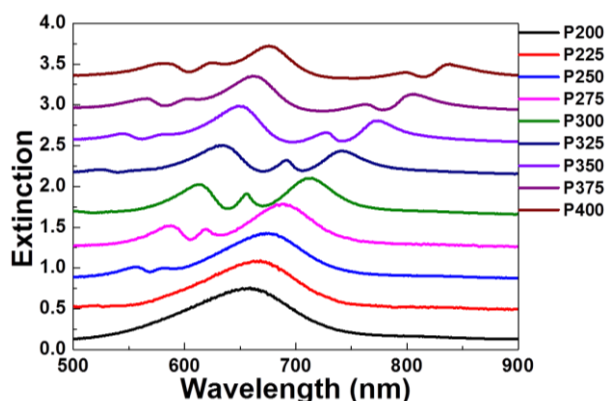


Figure 2.14 Measured far-field extinction spectra of Au-NGs/TiO₂ structure with different pitch sizes in water (P200 means Au-NGs/TiO₂ structure with 200 nm pitch size). Multi peaks can be observed with pitch size larger than 250 nm and they show spectral shift with increasing pitch size.

2.3.3 Finite-difference time-domain simulation results

To give a better understanding of the strong coupling mechanism, FDTD solutions software package was utilized to calculate and explore the far- and near-field spectra of Au-NGs/TiO₂ structures. The optical constants of the silica glass were obtained from Palik. The TiO₂ substrate was assumed to behave as a dielectric material with an average refractive index $n = 2.4$. The optical constants of Au were obtained using the data from Johnson and Christy.^[126] A discrete, uniformly spaced mesh with a mesh size of 2.5 nm was performed during the FDTD simulations. The background index of FDTD was set to be 1.33. The plane wave light source was injected onto Au-NGs/TiO₂

structures from the structure side polarized perpendicular to the Au-NGs length at normal incidence and oblique incidence with an incidence angle of 1.5° , respectively. In the light propagation direction, the perfectly matched layer boundary conditions were imposed, and in the plane perpendicular to the light propagation direction, the Bloch boundary conditions were applied on each boundary. The extinction spectra were obtained by a transmission power monitor located at 400 nm below the TiO_2 surface. Two power and profile monitors were performed to explore the near-field properties. One was located at the interface of the Au-NGs and TiO_2 to monitor the near-field enhancement. Another one covered the entire cross section of Au-NGs/ TiO_2 structures to monitor the electric and magnetic fields evolutions with various pitch sizes.

Figure 2.15 shows the simulated extinction spectra of such structures with various pitch sizes at normal incidence (a) and with 1.5° incidence degree (b), respectively. Obvious difference due to the oblique incidence is observed in Figure 2.15 (b) comparing with the spectra in Figure 2.15 (a). There is only one peak with 200 nm and 225 nm pitch sizes, which is in good accordance with the experimental extinction spectra as shown in Figure 2.14. The periodic Au-NGs can impart momentum to the incident light and couple it to waveguide modes supported by the TiO_2 waveguide thin film. As the pitch size is increased, starting with period of 250 nm, another additional peak which is due to the waveguide mode resonance appears as shown in Figure 2.15 (a). The strong coupling of the waveguide mode with the LSPR mode results in spectral doublets that display an avoided crossing behavior, as shown in the progression of the spectra with increasing pitch size in Figure 2.15 (a). However, the experimental extinction spectra as shown in Figure 2.14 have three peaks. This is due to the non-collimated incoherent light source employed during the extinction measurement and it is inevitable for oblique incidence. Therefore, various incidence degrees to the light source were introduced to optimize the simulations and 1.5° incidence angle gives the best reproduction of experimental data. As shown in Figure 2.15 (b), a sharp third peak appeared between the two peaks at normal incidence with pitch sizes larger than 250 nm due to the oblique incidence. The appearance of three peaks can be attributed to the

couplings between LSPR and two waveguide modes and two waveguide modes are excited by the oblique incidence.

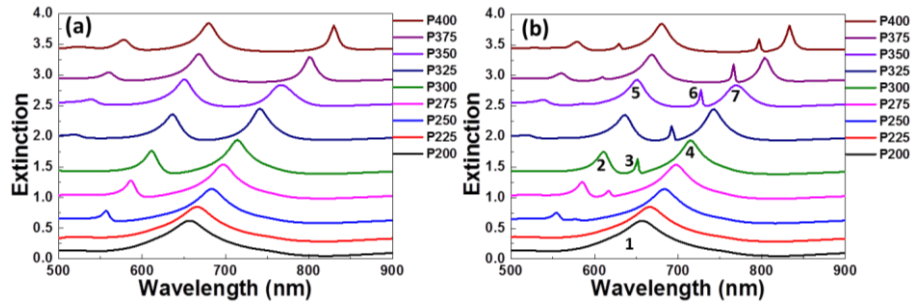


Figure 2.15 Calculated extinction spectra at normal incidence (a) and with (b) 1.5° incidence degree of Au-NGs/TiO₂ structure with different pitch sizes in water (P200 means Au-NGs/TiO₂ structure with 200 nm pitch size). Seven resonance peaks are marked from (1) to (7) as shown in (b) corresponding to pitch size of 200 nm (1) uncoupled one, 300 nm (2), (3) and (4), coupling (near tuning), 350 nm (5), (6) and (7) coupling (detuning).

The absorption, scattering and extinction cross-section of periodic Au-NGs-TiO₂ structures are also calculated by FDTD simulations. Figure 2.16 shows the respective simulated extinction (black), scattering (red) and absorption (blue) cross-section spectra with pitch size of 300 nm (a) and 350 nm (b), which show good agreement with the far-field extinction spectra as shown in Figure 2.15 (b). The scattering cross-sections of such structures are much larger than that of absorption ones due to the large size of Au-NGs.

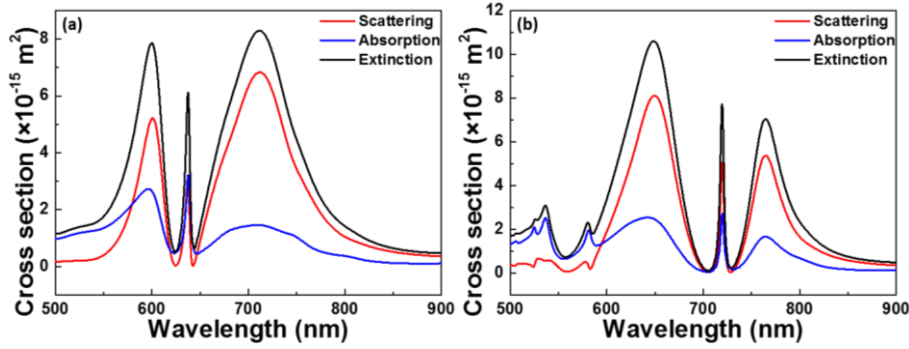


Figure 2.16 Calculated extinction (black), scattering (red) and absorption (blue) cross-sections of Au-NGs/TiO₂ structures with 300 nm (a) and 350 nm (b) pitch size, respectively.

The electric field distributions of selected seven characterized wavelengths corresponding to three pitch sizes of 200 nm, 300 nm and 350 nm are shown in Figure 2.17. Only LSPR mode is excited with 200 nm pitch size as shown in Figure 2.17 (1) due to absence of waveguide mode, which agrees with the far-field extinction spectra well. As the pitch size increases to 300 nm, both shorter-wavelength and longer-wavelength peaks show strong spatial confinements of electric fields at the interface between the Au-NGs and supported TiO₂ substrate, which are deriving from the excitation of LSPR mode of Au-NGs as shown in Figure 2.17 (2) (shorter-wavelength peak) and 2.17 (4) (longer-wavelength peak), respectively. Moreover, the electric field distributions inside the TiO₂ thin waveguide film also show the waveguide mode patterns especially the shorter-wavelength peak as shown in Figure 2.17 (2). However, in the case of 350 nm, shorter-wavelength peak shows much clearer plasmon characteristic than that of 300 nm pitch size, while the waveguide characteristic depresses as shown in Figure 2.17 (5). Therefore, shorter-wavelength peak is more plasmon-like mode with 350 nm pitch size. However, longer-wavelength peak is more waveguide-like mode as shown in Figure 2.17 (7).

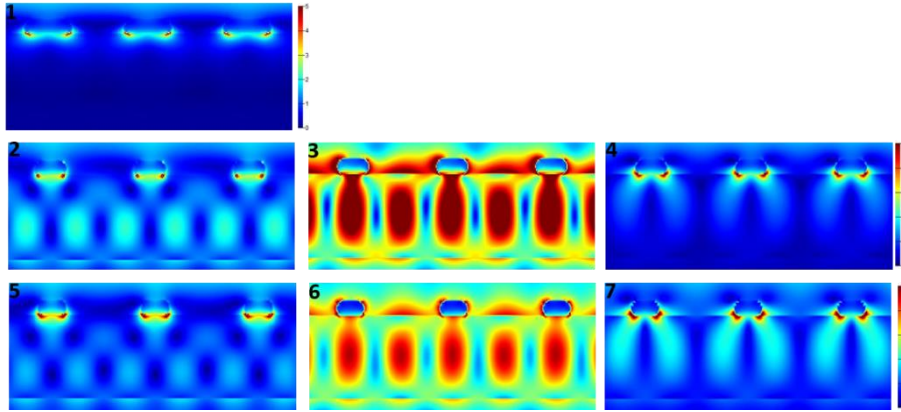


Figure 2.17 Calculated electric field $|E|$ distributions under selected seven characterized wavelengths with 200 nm, 300 nm and 350 nm period, respectively. Only LSPR mode is excited with 200 nm period as shown in (1) due to the absence of waveguide mode. Three characterized wavelengths of coupled waveguide-LSPR modes with 300 nm period: the shorter-peak wavelength (2, also named as P_+), the middle-peak wavelength (3), and the longer-peak wavelength of (4, P_-). (5), (6), and (7) correspond to three resonant peaks of 350 nm period.

The magnetic field distributions of selected seven characterized wavelengths of three pitch sizes of 200 nm, 300 nm and 350 nm corresponding to Figure 2.15 are shown in 2.18, which shows similar but much clearer behavior in comparison with Figure 2.17. The simulated results agree well with the experimental data, demonstrating that the coupling between LSPR and waveguide modes can be tuned by changing the pitch size of periodic Au-NGs.

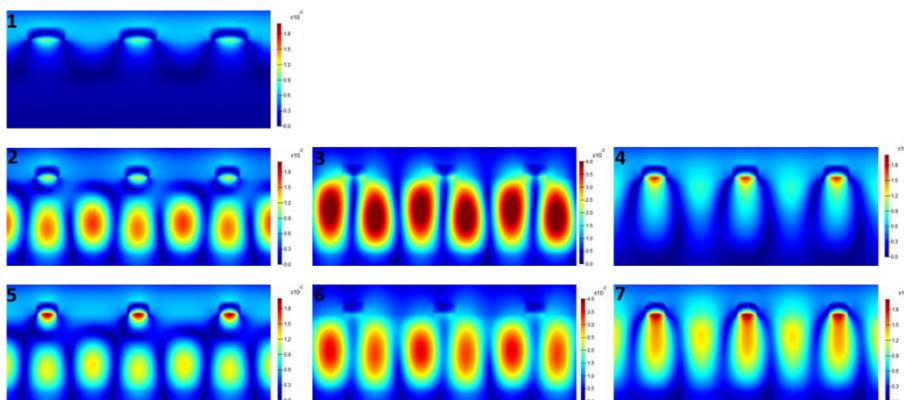


Figure 2.18 Calculated magnetic field $|H|$ distributions under selected seven characterized wavelengths with 200 nm, 300 nm and 350 nm period, respectively. Only LSPR mode is excited with 200 nm period as shown in (1). Three characterized wavelengths of coupled waveguide-LSPR modes with 300 nm period: the shorter-peak wavelength (2, also named as P_+), the middle-peak wavelength (3), and the longer-peak wavelength of (4, P_-). (5), (6), and (7) correspond to three peaks of 350 nm period.

2.3.4 Experimental and calculated hybrid dispersion curves

Due to strong coupling between the waveguide mode and LSPR mode, a strong anticrossing behavior of the modes instead of their spectral overlap can be observed in Figure 2.19, the experimental (a) and calculated (b) spectral peak positions (in photon energy) of two coupled waveguide-LSPR modes P_+ and P_- , which are obtained from the experimental (Figure 2.14) and simulated (Figure 2.15 (b)) extinction spectra, are plotted as a function of momentum. The momentum is calculated from the pitch sizes. As shown in Figure 2.19 (a), the horizontal red line shows the extinction maximum of the uncoupled bare LSPR mode (200 nm pitch size). The black line is the uncoupled bare waveguide mode estimated by numerical simulations using TiO_2 -NGs instead of Au-NGs. The interaction between the LSPR mode and the waveguide mode could result in hybridized plexciton states, which exhibit typical anticrossing behavior. The energies of the upper branch (P_+) and lower branch (P_-) plexciton states are calculated using a coupled harmonic oscillator model.^[127]

$$E_{\text{UB, LB}} = \frac{E_p + E_w}{2} \pm \frac{1}{2} \sqrt{(E_p - E_w)^2 + (\hbar\Omega)^2} \quad (2.1)$$

where E_p and E_w are the resonance energies of uncoupled bare LSPR mode and waveguide mode, respectively. $\hbar\Omega$ is the strong-coupling energy. The green and blue curves in Figure 2.19 (a) are fitting results calculated using equation 2.1. The splitting energy is estimated to be approximately 250 meV. The corresponding simulated

dispersion curve 3.12 (b) is also in very good agreement with the experimental results (a).

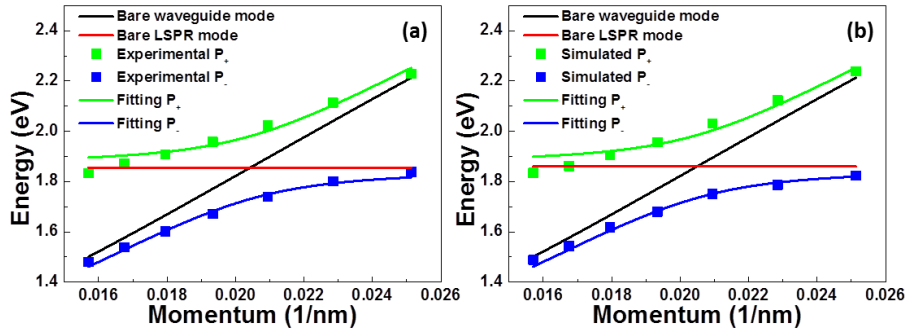


Figure 2.19 (a) Experimental and (b) calculated waveguide-LSPR modes hybrid dispersion curves. The black and red lines correspond to the uncoupled bare waveguide and LSPR modes, respectively. The green and blue dots were obtained from the maxima of the extinction spectrum. The green and blue lines are the corresponding fitted results deriving from green and blue dots, respectively.

2.3.5 Near-field and internal quantum efficiency spectra of periodic gold nanogratings patterned titanium dioxide photoelectrode

The near-field spectra of Au-NGs/TiO₂ structures with different pitch sizes were measured by utilizing a plasmon-induced photocurrent generation measurement to elucidate whether the strongly coupled waveguide-LSPR coupling modes are really induced or not. The photocurrent response of Au-NGs/TiO₂ photoelectrode under irradiation with different wavelength light was explored. Firstly, a 300-nm pitch size Au-NGs/TiO₂ photoelectrode was measured under dark and irradiation conditions with monochromatic light with different wavelengths. The linear sweep voltammograms *I-V* and *I-t* curves are shown in Figure 2.20 (a) and (b), respectively. 650 and 700 nm monochromatic wavelengths were employed for these measurements, respectively. From Figure 2.20 (b), anodic photocurrents were clearly observed under both 650 and 700 nm monochromatic wavelengths irradiations. Therefore, this indicates that the electrons were transferred from the periodic Au-NGs to the conduction band of TiO₂

and the remained holes in locally Au/TiO₂/water interface might oxidize water to evolve oxygen. Importantly, the induced photocurrent values are different with different irradiation wavelength. The EQE was calculated by the following formula:

$$EQE(\%) = \frac{I_{sc}(A)}{P(W)} \times \frac{1240}{\lambda(nm)} \times 100 \quad (2.2)$$

The EQE action spectrum is usually measured over a wide range of different wavelengths. I_{sc} is the generated photocurrent at a particular wavelength region. $P(W)$ is the incident power at this wavelength. Therefore, the EQE spectrum can be calculated and obtained as shown in Figure 2.20 (c).

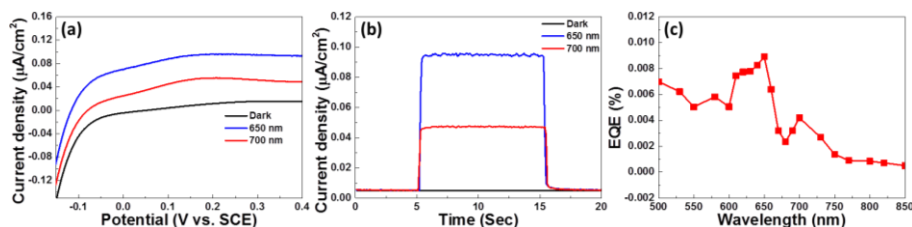


Figure 2.20 Photocurrent response of linear sweep voltammograms I - V (a) and I - t curves (b) measured using a 300-nm pitch size Au-NGs/TiO₂ photoelectrode under dark and irradiation conditions with a monochromatic light at wavelengths of 650 nm, and 700 nm, respectively. The sweep rate for the measurement of linear sweep voltammograms I - V was set at 5 mV/s, and the applied potential was set at +0.3 V versus SCE during the I - t curve measurements. (c) Calculated EQE spectrum of 300 nm pitch size Au-NGs/TiO₂ photoelectrode obtained from (b).

The IQE spectrum represents the ratio of the number of electrons resulting in the photocurrent generation with respect to the number of photons absorbed by Au-NGs. The IQE spectrum can be estimated from the generated photocurrents from a monochromatic photon flux over a long wavelength region. The IQE is normally calculated by correcting the EQE spectrum and photons absorbed by the Au-NGs as:

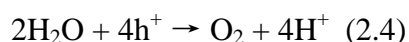
$$IQE = EQE/\eta \quad (2.3)$$

where η is the ratio of absorbed photons by Au-NGs among the irradiated photons.^[94] Therefore, η can be calculated and expressed by the following equation: absorbed photon flux/total photon flux. η can be easily obtained from the measured extinction spectra. However, lots of photons are scattered and lost in total extinction in the case of Au-NGs due to the larger size of Au-NGs. Therefore, a new parameter, absorption ratio in total extinction (γ), which is necessary to be taken into consideration to obtain the true IQE spectrum.

γ can be expressed by the ratio of the absorbed photons among all the incident photons. How to obtain the γ values of each wavelength? The absorption, scattering and extinction cross-sections of Au-NGs/TiO₂ structure with different pitch sizes have been calculated by FDTD simulations as shown in Figure 2.16. γ can be calculated and expressed by the following equation: $\gamma = \text{absorption cross section}/\text{extinction cross-section}$. The calculated absorption, scattering and extinction cross-sections of periodic Au-NGs/TiO₂ structure with 300 nm and 350 nm pitch sizes are shown in Figure 2.16 (a) and (b), respectively. From the experimental extinction spectrum and γ , η can be determined by multiplying experimental extinction and γ . Therefore, the IQE action spectra of Au-NGs/TiO₂ structure with 300 nm and 350 nm pitch sizes can be obtained from the equation 2.3.

The near-field enhancement spectra and IQE action spectra of periodic Au-NGs/TiO₂ structures with 300 nm and 350 nm pitch sizes plotted as a function of illuminated wavelength are shown in Figure 2.21 (a), (b), (c) and (d), respectively. The near-field enhancement spectra and IQE action spectra of periodic Au-NGs/TiO₂ structures with 300 nm and 350 nm pitch sizes both have three peaks as shown in Figure 2.21. It is hypothesized that the plasmon induced near-field enhancement plays a significant role in wavelength-dependent IQE. It was considered that the water oxidation, which is four electronic transitions, proceeds even with low energy light because the electron transfer reaction is induced by the near-field, and multiple holes are trapped to the surface states of TiO₂ at the restricted nanospace near the Au/TiO₂/water interface. In general, the IQE spectrum of dye-sensitized solar cell is not dependent on the wavelength because

the efficiency is normalized by the absorbed photons if the photocurrent generation is triggered only by the light absorption by organic dye molecules. However, the plasmon-induced water oxidation efficiency should be influenced not only by the light absorption but also by the local near-field intensity because the reaction proceeds via multi-electron transfers only at the restricted nanospace. The photocurrent generation is induced by water oxidation. Therefore, water molecules are used as an electron source for photocurrent generation as shown below:



Efficient oxidation of water molecules requires highly concentrated electron holes at a local site because multiple electron-transfer processes are required with two water molecules. It is hypothesized that excited electrons are transferred into the conduction band of TiO_2 immediately from Au-NGs induced by plasmonically enhanced near-field and multiple holes trapped at a local site through surface states of TiO_2 near the hot site of Au/ TiO_2 /water interface. The stored multiple holes confined at a local site of the TiO_2 may be able to accelerate the oxidation of water and the subsequent evolution of oxygen. This demonstrates that the near-field enhancement directly affected the oxidation of water molecules and photocurrent generation. Therefore, the IQE action spectra are highly dependent on near-field enhancement spectra.

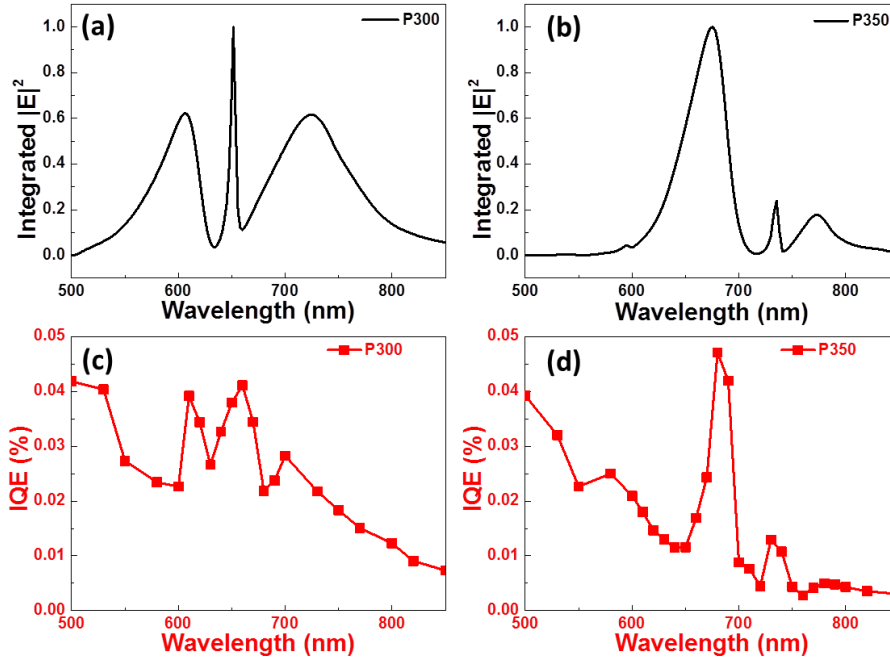


Figure 2.21 The normalized near-field (black) enhancement action spectra of Au-NGs/TiO₂ structure with 300 nm (a) and 350 nm (b) period, respectively. The corresponding IQE (red) spectra of Au-NGs/TiO₂ structure with 300 nm (c) and 350 nm (d), respectively. The action spectrum of near-field intensity was calculated by monitoring at the interface between Au-NGs and the TiO₂ film by the FDTD numerical simulations.

The relative intensity of IQE and near-field enhancement spectra need to be taken into consideration. In the case of 300 nm pitch size as shown in Figure 2.21 (a) and (c), importantly, P_+ (shorter-wavelength) and P_- (longer-wavelength) modes have comparable near-field enhancement and IQE values. However, in the case of 350 nm pitch size as shown in Figure 3.14 (b) and (d), the P_+ (shorter-wavelength) has much higher near-field enhancement and IQE values in comparison with P_- (longer-wavelength). The plasmon-induced photocurrent generation is induced by the plasmon-induced charge separation which is happened at the interface between Au nanostructures and TiO₂ and subsequent water oxidation. However, in the case of coupled waveguide-plasmon modes systems, the waveguide mode, which is confined

inside the TiO_2 waveguide film, cannot induce the photocurrent generation because TiO_2 does not absorb the visible light. Therefore, the plasmon component plays the role in photocurrent generation. In the case of 300 nm pitch size, both of the coupled P_+ and P_- have comparable plasmon characteristics and near-field enhancement. As a result, both coupled P_+ and P_- can obtain comparable IQE values. However, in the case of 350 nm pitch size, the P_+ is more plasmon-like mode and the P_- is more waveguide-like mode. Therefore, the P_+ has much higher near-field enhancement and obtain larger IQE value than the P_- with 350 nm pitch size. The IQE action spectra are in good accordance with near-field spectra.

2.4 Conclusions

In conclusion, plasmon-induced photocurrent generation was pursued as an effective approach to explore the spectral near-field properties of strongly coupled waveguide-plasmon modes. Periodic Au-NGs/TiO₂ structures, which can support both waveguide and plasmon modes and induce strong coupling of waveguide-LSPR modes with a large splitting energy of approximate 250 meV, were fabricated and utilized as photoelectrodes to measure the photocurrent generation. Moreover, under tuning and detuning conditions by changing the pitch size, it was clearly elucidated that the PEC response is corresponding to the near-field coupling. A highly sensitive PEC biosensor is highly respected by utilizing near-field coupling enhanced photocurrent generation.

2.5 References

- [1]. Yamaguti, K.; Sato, S., "Photolysis of Water over Metallized Powdered Titanium-Dioxide", *Journal of the Chemical Society, Faraday Transactions 1* **1985**, *81*, 1237-1246.
- [2]. Abe, T.; Suzuki, E.; Nagoshi, K.; Miyashita, K.; Kaneko, M., "Electron source in photoinduced hydrogen production on Pt-supported TiO₂ particles", *Journal of Physical Chemistry B* **1999**, *103*, 1119-1123.
- [3]. Kuwabata, S.; Uchida, H.; Ogawa, A.; Hirao, S.; Yoneyama, H., "Selective Photoreduction of Carbon-Dioxide to Methanol on Titanium-Dioxide Photocatalysts in Propylene Carbonate Solution", *Journal of the Chemical Society, Chemical Communications* **1995**, 829-830.
- [4]. Inoue, T.; Fujishima, A.; Konishi, S.; Honda, K., "Photoelectrocatalytic Reduction of Carbon-Dioxide in Aqueous Suspensions of Semiconductor Powders", *Nature* **1979**, *277*, 637-638.
- [5]. Davis, A. P.; Green, D. L., "Photocatalytic oxidation of cadmium-EDTA with titanium dioxide", *Environmental Science & Technology* **1999**, *33*, 609-617.
- [6]. Zhao, W.; Ma, W. H.; Chen, C. C.; Zhao, J. C.; Shuai, Z. G., "Efficient degradation of toxic organic pollutants with Ni₂O₃/TiO₂-xBx under visible irradiation", *Journal of the American Chemical Society* **2004**, *126*, 4782-4783.
- [7]. Jang, H. D.; Kim, S. K.; Kim, S. J., "Effect of particle size and phase composition of titanium dioxide nanoparticles on the photocatalytic properties", *Journal of Nanoparticle Research* **2001**, *3*, 141-147.
- [8]. Matthews, R. W., "Purification of Water with near-Uv Illuminated Suspensions of Titanium-Dioxide", *Water Research* **1990**, *24*, 653-660.
- [9]. Reeves, P.; Ohlhausen, R.; Sloan, D.; Pamplin, K.; Scoggins, T.; Clark, C.; Hutchinson, B.; Green, D., "Photocatalytic Destruction of Organic-Dyes in Aqueous

TiO₂ Suspensions Using Concentrated Simulated and Natural Solar-Energy”, *Solar Energy* **1992**, *48*, 413-420.

[10]. Taylor, C. E., “Methane conversion via photocatalytic reactions”, *Catalysis Today* **2003**, *84*, 9-15.

[11]. Pramauro, E.; Prevot, A. B.; Vincenti, M.; Gamberini, R., “Photocatalytic degradation of naphthalene in aqueous TiO₂ dispersions: Effect of nonionic surfactants”, *Chemosphere*, **1998**, *36*, 1523-1542.

[12]. Chen, L. C.; Chou, T. C., “Photobleaching of Methyl-Orange in Titanium-Dioxide Suspended in Aqueous-Solution”, *Journal of Molecular Catalysis* **1993**, *85*, 201-214.

[13]. Sun, B.; Vorontsov, A. V.; Smirniotis, P. G., Role of platinum deposited on TiO₂ in phenol photocatalytic oxidation. *Langmuir* **2003**, *19*, 3151-3156.

[14]. Kim, D. H.; M. A. Anderson., Photoelectrocatalytic Degradation of Formic-Acid Using a Porous TiO₂ Thin-Film Electrode. *Environmental Science & Technology* **1994**, *28*, 479-483.

[15]. Fujishima, A.; Honda, K., Electrochemical Photolysis of Water at a Semiconductor Electrode. *Nature* **1972**, *238*, 37-38.

[16]. Kudo, A.; Miseki, Y., Heterogeneous photocatalyst materials for water splitting. *Chemical Society Reviews* **2009**, *38*, 253-278.

[17]. Yang, X. Y.; Wolcott, A.; Wang, G. M.; Sobo, A.; Fitzmorris, R. C.; Qian, F.; Zhang, J. Z.; Li, Y., Nitrogen-Doped ZnO Nanowire Arrays for Photoelectrochemical Water Splitting. *Nano Letters* **2009**, *9*, 2331-2336.

[18]. Qiu, Y. C.; Yan, K. Y.; Deng, H.; Yang, S. H., Secondary Branching and Nitrogen Doping of ZnO Nanotetrapods: Building a Highly Active Network for Photoelectrochemical Water Splitting. *Nano Letters* **2012**, *12*, 407-413.

[19]. Wang, C.; Feng, Y. J.; Cai, L.; Yang, X. Y.; He, J. F.; Yan, W. S.; Liu, Q. H.; Sun, Z. H.; Hu, F. C.; Xie, Z.; Yao, T.; Wei, S. Q., ZnO@S-doped ZnO core/shell

nanocomposites for highly efficient solar water splitting. *J Power Sources* **2014**, 269, 24-30.

[20]. Gurunathan, K.; Maruthamuthu, P.; Sastri, M. V. C., Photocatalytic hydrogen production by dye-sensitized Pt/SnO₂ and Pt/SnO₂/RuO₂ in aqueous methyl viologen solution. *International journal of hydrogenenergy* **1997**, 22, 57-62.

[21]. Wang, Y. Q.; Zhang, Z. J.; Zhu, Y.; Li, Z. C.; Vajtai, R.; Ci, L. J.; Ajayan, P. M., Nanostructured VO₂ photocatalysts for hydrogen production. *ACS Nano* **2008**, 2, 1492-1496.

[22]. Sayama, K.; Arakawa, H., Photocatalytic Decomposition of Water and Photocatalytic Reduction of Carbon-Dioxide over ZrO₂ Catalyst. *Journal of Physical Chemistry* **1993**, 97, 531-533.

[23]. Sayama, K.; Arakawa, H., Effect of Na₂CO₃ Addition on Photocatalytic Decomposition of Liquid Water over Various Semiconductor Catalysts. *J Journal of Photochemistry and Photobiology A: Chemistry* **1994**, 77, 243-247.

[24]. Huang, Y. F.; Xie, Y. M.; Fan, L. Q.; Li, Y. B.; Wei, Y. L.; Lin, J. M., Synthesis and photochemical properties of La-doped HCa₂Nb₃O₁₀. *International journal of hydrogenenergy* **2008**, 33, 6432-6438.

[25]. Kato, H.; Kudo, A., New tantalate photocatalysts for water decomposition into H₂ and O₂. *Chemical Physics Letters* **1998**, 295, 487-492.

[26]. Sayama, K.; Arakawa, H.; Domen, K., Photocatalytic water splitting on nickel intercalated A₄TaxNb_{6-x}O₁₇ (A=K, Rb). *Catalysis Today* **1996**, 28, 175-182.

[27]. Chen, X. Y.; Yu, T.; Fan, X. X.; Zhang, H. T.; Li, Z. S.; Ye, J. H.; Zou, Z. G., Enhanced activity of mesoporous Nb₂O₅ for photocatalytic hydrogen production. *Applied Surface Science* **2007**, 253, 8500-8506.

[28]. Domen, K.; Naito, S.; Soma, M.; Onishi, T.; Tamaru, K., Photocatalytic Decomposition of Water-Vapor on an NiO-SrTiO₃ Catalyst. *Journal of the Chemical Society, Chemical Communications* **1980**, 543-544.

- [29]. Domen, K.; Naito, S.; Onishi, T.; Tamaru, K., Study of the Photocatalytic Decomposition of Water-Vapor over a NiO-SrTiO₃ Catalyst. *Journal of Physical Chemistry* **1982**, *86*, 3657-3661.
- [30]. Domen, K.; Naito, S.; Onishi, T.; Tamaru, K., Photocatalytic Decomposition of Liquid Water on a NiO-SrTiO₃ Catalyst. *Chemical Physics Letters* **1982**, *92*, 433-434.
- [31]. Domen, K.; Kudo, A.; Onishi, T., Mechanism of Photocatalytic Decomposition of Water into H₂ and O₂ over NiO-SrTiO₃. *Journal of Catalysis* **1986**, *102*, 92-98.
- [32]. Domen, K.; Kudo, A.; Onishi, T.; Kosugi, N.; Kuroda, H., Photocatalytic Decomposition of Water into H₂ and O₂ over NiO-SrTiO₃ Powder .1. Structure of the Catalyst. *Journal of Physical Chemistry* **1986**, *90*, 292-295.
- [33]. Liu, Y.; Xie, L.; Li, Y.; Yang, R.; Qu, J. L.; Li, Y. Q.; Li, X. G., Synthesis and high photocatalytic hydrogen production of SrTiO₃ nanoparticles from water splitting under UV irradiation. *Journal of Power Sources* **2008**, *183*, 701-707.
- [34]. Qin, Y.; Wang, G. Y.; Wang, Y. J., Study on the photocatalytic property of La-doped CoO/SrTiO₃ for water decomposition to hydrogen. *Catalysis Commun* **2007**, *8*, 926-930.
- [35]. Takata, T.; Domen, K., Defect Engineering of Photocatalysts by Doping of Aliovalent Metal Cations for Efficient Water Splitting. *Journal of Physical Chemistry C* **2009**, *113*, 19386-19388.
- [36]. Yamashita, Y.; Yoshida, K.; Kakihana, M.; Uchida, S.; Sato, T., Polymerizable complex synthesis of RuO₂/BaTi₄O₉ photocatalysts at reduced temperatures: Factors affecting the photocatalytic activity for decomposition of water. *Chemistry of Materials* **1999**, *11*, 61-66.
- [37]. Mizoguchi, H.; Ueda, K.; Orita, M.; Moon, S. C.; Kajihara, K.; Hirano, M.; Hosono, H., Decomposition of water by a CaTiO₃ photocatalyst under UV light irradiation. *Materials Research Bulletin* **2002**, *37*, 2401-2406.

- [38]. Maeda, K.; Teramura, K.; Saito, N.; Inoue, Y.; Domen, K., Photocatalytic overall water splitting on gallium nitride powder. *Bulletin of the Chemical Society of Japan* **2007**, *80*, 1004-1010.
- [39]. Arai, N.; Saito, N.; Nishiyama, H.; Inoue, Y.; Domen, K.; Sato, K., Overall water splitting by RuO₂-dispersed divalent-ion-doped GaN photocatalysts with d10 electronic configuration. *Chemistry letters* **2006**, *35*, 796-797.
- [40]. Ohmori, T.; Mametsuka, H.; Suzuki, E., Photocatalytic hydrogen evolution on InP suspension with inorganic sacrificial reducing agent. *International journal of hydrogenenergy* **2000**, *25*, 953-955.
- [41]. Reber, J. F.; Meier, K., Photochemical Production of Hydrogen with Zinc-Sulfide suspensions. *Journal of Physical Chemistry* **1984**, *88*, 5903-5913.
- [42]. Maeda, K.; Saito, N.; Lu, D. L.; Inoue, Y.; Domen, K., Photocatalytic properties of RuO₂-loaded β -Ge₃N₄ for overall water splitting. *Journal of Physical Chemistry C* **2007**, *111*, 4749-4755.
- [43]. Sato, J.; Saito, N.; Yamada, Y.; Maeda, K.; Takata, T.; Kondo, J. N.; Hara, M.; Kobayashi, H.; Domen, K.; Inoue, Y., RuO₂-loaded β -Ge₃N₄ as a non-oxide photocatalyst for overall water splitting. *Journal of the American Chemical Society* **2005**, *127*, 4150-4151.
- [44]. Maeda, K.; Saito, N.; Inoue, Y.; Domen, K., Dependence of activity and stability of germanium nitride powder for photocatalytic overall water splitting on structural properties. *Chemistry of Materials* **2007**, *19*, 4092-4097.
- [45]. Maeda, K.; Nishimura, N.; Domen, K., A precursor route to prepare tantalum (V) nitride nanoparticles with enhanced photocatalytic activity for hydrogen evolution under visible light. *Applied Catalysis A: General* **2009**, *370*, 88-92.
- [46]. Amirav, L.; Alivisatos, A. P., Photocatalytic Hydrogen Production with Tunable Nanorod Heterostructures. *Journal of Physical Chemistry Letters* **2010**, *1*, 1051-1054.

- [47]. Linsebigler, A. L.; Lu, G. Q.; Yates, J. T., Photocatalysis on TiO₂ Surfaces: Principles, Mechanisms, and Selected Results. *Chemical Reviews* **1995**, *95*, 735-758.
- [48]. Bai, J.; Zhou, B. X., Titanium Dioxide Nanomaterials for Sensor Applications. *Chemical Reviews* **2014**, *114*, 10131-10176.
- [49]. Bourikas, K.; Kordulis, C.; Lycourghiotis, A., Titanium Dioxide (Anatase and Rutile): Surface Chemistry, Liquid Solid Interface Chemistry, and Scientific Synthesis of Supported Catalysts. *Chemical Reviews* **2014**, *114*, 9754-9823.
- [50]. Ma, Y.; Wang, X. L.; Jia, Y. S.; Chen, X. B.; Han, H. X.; Li, C., Titanium Dioxide-Based Nanomaterials for Photocatalytic Fuel Generations. *Chemical Reviews* **2014**, *114*, 9987-10043.
- [51]. Bendavid, A.; Martin, P. J.; Jamting, A.; Takikawa, H., Structural and optical properties of titanium oxide thin films deposited by filtered arc deposition. *Thin Solid Films* **1999**, *355*, 6-11.
- [52]. Borgarello, E.; Kiwi, J.; Gratzel, M.; Pelizzetti, E.; Visca, M., Visible-Light Induced Water Cleavage in Colloidal Solutions of Chromium-Doped Titanium-Dioxide Particles. *Journal of the American Chemical Society* **1982**, *104*, 2996-3002.
- [53]. Chae, J.; Lee, J.; Jeong, J. H.; Kang, M., Hydrogen Production from Photo Splitting of Water Using the Ga-incorporated TiO₂ Prepared by a Solvothermal Method and Their Characteristics. *Bulletin of the Korean Chemical Society* **2009**, *30*, 302-308.
- [54]. Jing, D. W.; Zhang, Y. J.; Guo, L. J., Study on the synthesis of Ni doped mesoporous TiO₂ and its photocatalytic activity for hydrogen evolution in aqueous methanol solution. *Chemical Physics Letters* **2005**, *415*, 74-78.
- [55]. Sasikala, R.; Sudarsan, V.; Sudakar, C.; Naik, R.; Sakuntala, T.; Bharadwaj, S. R., Enhanced photocatalytic hydrogen evolution over nanometer sized Sn and Eu doped titanium oxide. *International journal of hydrogenenergy* **2008**, *33*, 4966-4973.

- [56]. Kato, H.; Kudo, A., Visible-light-response and photocatalytic activities of TiO₂ and SrTiO₃ photocatalysts codoped with antimony and chromium. *Journal of Physical Chemistry B* **2002**, *106*, 5029-5034.
- [57]. Umebayashi, T.; Yamaki, T.; Itoh, H.; Asai, K., Analysis of electronic structures of 3d transition metal-doped TiO₂ based on band calculations. *Journal of Physical Chemistry Solids* **2002**, *63*, 1909-1920.
- [58]. Rengaraj, S.; Li, X. Z., Enhanced photocatalytic activity of TiO₂ by doping with Ag for degradation of 2,4,6-trichlorophenol in aqueous suspension. *Journal of Molecular Catalysis A: Chemical* **2006**, *243*, 60-67.
- [59]. Kim, S.; Hwang, S. J.; Choi, W. Y., Visible light active platinum-ion-doped TiO₂ photocatalyst. *Journal of Physical Chemistry B* **2005**, *109*, 24260-24267.
- [60]. Park, J. H.; Kim, S.; Bard, A. J., Novel carbon-doped TiO₂ nanotube arrays with high aspect ratios for efficient solar water splitting. *Nano Letters* **2006**, *6*, 24-28.
- [61]. Irie, H.; Watanabe, Y.; Hashimoto, K., Carbon-doped anatase TiO₂ powders as a visible-light sensitive photocatalyst. *Chemistry letters* **2003**, *32*, 772-773.
- [62]. Asahi, R.; Morikawa, T.; Ohwaki, T.; Aoki, K.; Taga, Y., Visible-light photocatalysis in nitrogen-doped titanium oxides. *Science* **2001**, *293*, 269-271.
- [63]. Chen, X. B.; Burda, C., The electronic origin of the visible-light absorption properties of C-, N- and S-doped TiO₂ nanomaterials. *Journal of the American Chemical Society* **2008**, *130*, 5018-5019.
- [64]. Li, Q.; Li, Y. W.; Wu, P. G.; Xie, R. C.; Shang, J. K., Palladium Oxide Nanoparticles on Nitrogen-Doped Titanium Oxide: Accelerated Photocatalytic Disinfection and Post-Illumination Catalytic "Memory". *Advanced Materials* **2008**, *20*, 3717-3723
- [65]. Wang, G. M.; Wang, H. Y.; Ling, Y. C.; Tang, Y. C.; Yang, X. Y.; Fitzmorris, R. C.; Wang, C. C.; Zhang, J. Z.; Li, Y., Hydrogen-Treated TiO₂ Nanowire Arrays for Photoelectrochemical Water Splitting. *Nano Letters* **2011**, *11*, 3026-3033.

- [66]. Ohno, T.; Mitsui, T.; Matsumura, M., Photocatalytic activity of S-doped TiO₂ photocatalyst under visible light. *Chemistry letters* **2003**, *32*, 364-365.
- [67]. Chen, X. B.; Liu, L.; Yu, P. Y.; Mao, S. S., Increasing Solar Absorption for Photocatalysis with Black Hydrogenated Titanium Dioxide Nanocrystals. *Science* **2011**, *331*, 746-750.
- [68]. Sheng, Y. G.; Xu, Y.; Jiang, D.; Liang, L. P.; Wu, D.; Sun, Y. H., Hydrothermal preparation of visible-light-driven N-Br-codoped TiO₂ photocatalysts. *International Journal of Photoenergy* **2008**.
- [69]. Ozaki, H.; Iwamoto, S.; Inoue, M., Improved visible-light responsive photocatalytic activity of N and Si co-doped titanias. *Journal of materials science* **2007**, *42*, 4009-4017.
- [70]. Luo, H. M.; Takata, T.; Lee, Y. G.; Zhao, J. F.; Domen, K.; Yan, Y. S., Photocatalytic activity enhancing for titanium dioxide by co-doping with bromine and chlorine. *Chemistry of Materials* **2004**, *6*, 846-849.
- [71]. Liu, G.; Zhao, Y.; Sun, C.; Li, F.; Lu, G. Q.; Cheng, H. M., Synergistic effects of B/N doping on the visible-light photocatalytic activity of mesoporous TiO₂. *Angewandte Chemie-International Edition* **2008**, *47*, 4516-4520.
- [72]. Xu, J. J.; Ao, Y. H.; Fu, D. G., A novel Ce, C-codoped TiO₂ nanoparticles and its photocatalytic activity under visible light. *Applied Surface Science* **2009**, *256*, 884-888.
- [73]. Song, S.; Tu, J. J.; Xu, L. J.; Xu, X.; He, Z. Q.; Qiu, J. P.; Ni, J. G.; Chen, J. M., Preparation of a titanium dioxide photocatalyst codoped with cerium and iodine and its performance in the degradation of oxalic acid. *Chemosphere* **2008**, *73*, 1401-1406.
- [74]. Liu, C.; Tang, X. H.; Mo, C. H.; Qiang, Z., Characterization and activity of visible-light-driven TiO₂ photocatalyst codoped with nitrogen and cerium. *Journal of Solid State Chemistry* **2008**, *181*, 913-919.

- [75]. Wei, C. H.; Tang, X. H.; Liang, J. R.; Tan, S. Y., Preparation, characterization and photocatalytic activities of boron and cerium-codoped TiO₂. *Journal of Environmental-China* **2007**, *19*, 90-96.
- [76]. Tryba, B., Increase of the photocatalytic activity of TiO₂ by carbon and iron modifications. *International Journal of Photoenergy* **2008**.
- [77]. Shen, X. Z.; Guo, J.; Liu, Z. C.; Xie, S. M., Visible-light-driven titania photocatalyst co-doped with nitrogen and ferrum. *Applied Surface Science* **2008**, *254*, 4726-4731.
- [78]. Lv, K. L.; Zuo, H. S.; Sun, J.; Deng, K. J.; Liu, S. C.; Li, X. F.; Wang, D. Y., (Bi, C and N) codoped TiO₂ nanoparticles. *Journal of Hazardous Materials* **2009**, *161*, 396-401.
- [79]. Wang, Y.; Wang, Y.; Meng, Y. L.; Ding, H. M.; Shan, Y. K.; Zhao, X.; Tang, X. Z., A highly efficient visible-light-activated photocatalyst based on bismuth- and sulfur-codoped TiO₂. *Journal of Physical Chemistry C* **2008**, *112*, 6620-6626.
- [80]. Huang, Y.; Ho, W. K.; Ai, Z. H.; Song, X. A.; Zhang, L. Z.; Lee, S. C., Aerosol-assisted flow synthesis of B-doped, Ni-doped and B-Ni-codoped TiO₂ solid and hollow microspheres for photocatalytic removal of NO. *Applied Catalysis B: Environmental* **2009**, *89*, 398-405.
- [81]. Zhang, X.; Liu, Q. Q., Visible-light-induced degradation of formaldehyde over titania photocatalyst co-doped with nitrogen and nickel. *Applied Surface Science* **2008**, *254*, 4780-4785.
- [82]. Xia, H. L.; Zhuang, H. S.; Xiao, D. C.; Zhang, T., Photocatalytic activity of La³⁺/S/TiO₂ photocatalyst under visible light. *Journal of Alloys and Compounds* **2008**, *465*, 328-332.
- [83]. He, Z. Q.; Xu, X.; Song, S.; Xie, L.; Tu, J. J.; Chen, J. M.; Yan, B., A Visible Light-Driven Titanium Dioxide Photocatalyst Codoped with Lanthanum and Iodine: An Application in the Degradation of Oxalic Acid. *Journal of Physical Chemistry C* **2008**, *112*, 16431-16437.

- [84]. Long, R.; English, N. J., First-principles calculation of nitrogen-tungsten codoping effects on the band structure of anatase-titania. *Applied Physics Letters* **2009**, *94*, 132102.
- [85]. Huang, L. H.; Sun, C.; Liu, Y. L., Pt/N-codoped TiO₂ nanotubes and its photocatalytic activity under visible light. *Applied Surface Science* **2007**, *253*, 7029-7035.
- [86]. Sasikala, R.; Shirole, A. R.; Sudarsan, V.; Jagannath.; Sudakar, C.; Naik, R.; Rao, R.; Bharadwaj, S. R., Enhanced photocatalytic activity of indium and nitrogen co-doped TiO₂-Pd nanocomposites for hydrogen generate. *Applied Catalysis A: General* **2010**, *37*, 47-54.
- [87]. O'Regan, B.; Gratzel, M., A low-cost, high-efficiency solar cell based on dye-sensitized colloidal TiO₂ films. *Nature* **1991**, *353* (6346), 737-740.
- [88]. Brown, M. D.; Suteewong, T.; Kumar, R. S. S.; D'Innocenzo, V.; Petrozza, A.; Lee, M. M.; Wiesner, U.; Snaith, H. J., Plasmonic Dye-Sensitized Solar Cells Using Core-Shell Metal-Insulator Nanoparticles. *Nano Letters* **2011**, *11*, 438-445.
- [89]. Chen, X. B.; Shen, S. H.; Guo, L. J.; Mao, S. S., Semiconductor-based Photocatalytic Hydrogen Generation. *Chemical Reviews* **2010**, *110*, 6503-6570.
- [90]. Zhao, G.; Kozuka, H.; Yoko, T., Sol-gel preparation and photoelectrochemical properties of TiO₂ films containing Au and Ag metal particles. *Thin Solid Films* **1996**, *277*, 147-154.
- [91]. Tian, Y.; Tatsuma, T., Plasmon-induced photoelectrochemistry at metal nanoparticles supported on nanoporous TiO₂. *Chemical Communications* **2004**, 1810-1811.
- [92]. Tian, Y.; Tatsuma, T., Mechanisms and applications of plasmon-induced charge separation at TiO₂ films loaded with gold nanoparticles. *Journal of the American Chemical Society* **2005**, *127*, 7632-7637.

- [93]. Furube, A.; Du, L.; Hara, K.; Katoh, R.; Tachiya, M., Ultrafast plasmon-induced electron transfer from gold nanodots into TiO₂ nanoparticles. *Journal of the American Chemical Society* **2007**, *129*, 14852-14853.
- [94]. Nishijima, Y.; Ueno, K.; Yokota, Y.; Murakoshi, K.; Misawa, H., Plasmon-Assisted Photocurrent Generation from Visible to Near-Infrared Wavelength Using a Au-Nanorods/TiO₂ Electrode. *Journal of Physical Chemistry Lett* **2010**, *1*, 2031-2036.
- [95]. Nishijima, Y.; Ueno, K.; Kotake, Y.; Murakoshi, K.; Inoue, H.; Misawa, H., Near-Infrared Plasmon-Assisted Water Oxidation. *Journal of Physical Chemistry Lett* **2012**, *3*, 1248-1252.
- [96]. Shi, X.; Ueno, K.; Takabayashi, N.; Misawa, H., Plasmon-Enhanced Photocurrent Generation and Water Oxidation with a Gold Nanoisland-Loaded Titanium Dioxide Photoelectrode. *Journal of Physical Chemistry C* **2013**, *117*, 2494-2499.
- [97]. Shi, X.; Ueno, K.; Oshikiri, T.; Misawa, H., Improvement of Plasmon-Enhanced Photocurrent Generation by Interference of TiO₂ Thin Film. *Journal of Physical Chemistry C* **2013**, *117*, 24733-24739.
- [98]. Zhong, Y. Q.; Ueno, K.; Mori, Y.; Shi, X.; Oshikiri, T.; Murakoshi, K.; Inoue, H.; Misawa, H., Plasmon-Assisted Water Splitting Using Two Sides of the Same SrTiO₃ Single-Crystal Substrate: Conversion of Visible Light to Chemical Energy. *Angewandte Chemie-International Edition* **2014**, *53*, 10350-10354.
- [99]. Oshikiri, T.; Ueno, K.; Misawa, H., Plasmon-Induced Ammonia Synthesis through Nitrogen Photofixation with Visible Light Irradiation. *Angewandte Chemie-International Edition* **2014**, *53*, 9802-9805.
- [100]. Bian, Z. F.; Tachikawa, T.; Zhang, P.; Fujitsuka, M.; Majima, T., Au/TiO₂ Superstructure-Based Plasmonic Photocatalysts Exhibiting Efficient Charge Separation and Unprecedented Activity. *Journal of the American Chemical Society* **2014**, *136*, 458-465.

- [101]. Liu, Z. W.; Hou, W. B.; Pavaskar, P.; Aykol, M.; Cronin, S. B., Plasmon Resonant Enhancement of Photocatalytic Water Splitting Under Visible Illumination. *Nano Letters* **2011**, *11*, 1111-1116.
- [102]. Ingram, D. B.; Linic, S. Water Splitting on Composite Plasmonic-Metal/Semiconductor Photoelectrodes: Evidence for Selective Plasmon-Induced Formation of Charge Carriers Near the Semiconductor Surface. *Journal of the American Chemical Society* **2011**, *133*, 5202–5205.
- [103]. Zhong, Y. Q.; Ueno, K.; Mori, Y.; Oshikiri, T.; Misawa, H., Cocatalyst Effects on Hydrogen Evolution in a Plasmon-Induced Water-Splitting System. *Journal of Physical Chemistry C* **2015**, *119*, 8889-8897.
- [104]. Oshikiri, T., Ueno, K., Misawa, H., Selective Dinitrogen Conversion to Ammonia Using Water and Visible Light through Plasmon-induced Charge Separation. *Angewandte Chemie-International Edition* **2016**, *55*, 3942-3946.
- [105]. Zhang, X. M.; Chen, Y. L.; Liu, R. S.; Tsai, D. P., Plasmonic photocatalysis. *REPORTS ON PROGRESS IN PHYSICS* **2013**, *76*, 046401.
- [106]. Ueno, K.; Misawa, H., Plasmon-enhanced photocurrent generation and water oxidation from visible to near-infrared wavelengths. *NPG Asia Materials* **2013**, *5*, e61.
- [107]. Hou, W. B., Cronin, S. B. A Review of Surface Plasmon Resonance-Enhanced Photocatalysis. *Advanced Functional Materials* **2013**, *23*, 1612-1619.
- [108]. Clavero, C., Plasmon-induced hot-electron generation at nanoparticle/metal-oxide interfaces for photovoltaic and photocatalytic devices. *Nat Photonics* **2014**, *8*, 95-103.
- [109]. McFarland, E. W.; Tang, J., A Photovoltaic Device Structure Based on Internal Electron Emission. *Nature* **2003**, *421*, 616–618.

[110]. Grancini, G.; Maiuri, M.; Fazzi, D.; Petrozza, A.; Egelhaaf, H.-J.; Brida, D.; Cerullo, G.; Lanzani, G., Hot Exciton Dissociation in Polymer Solar Cells. *Nature Materials* **2013**, *12*, 29-33.

[111]. Armin, A.; Zhang, Y. L.; Burn, P. L.; Meredith, P.; Pivrikas, A., Measuring internal quantum efficiency to demonstrate hot exciton dissociation, *Nature Materials* **2013**, *12*, 593.

[112]. Scharber, M., Measuring internal quantum efficiency to demonstrate hot exciton dissociation, *Nature Materials* **2013**, *12*, 594.

[113]. Grancini, G.; Binda, M.; Criante, L.; Perissinotto, S.; Maiuri, M.; Fazzi, D.; Petrozza, A.; Egelhaaf, H.-J.; Brida, D.; Cerullo, G.; Lanzani, G., Measuring internal quantum efficiency to demonstrate hot exciton dissociation Reply, *Nature Materials* **2013**, *12*, 594-595.

[114]. Bian, Z.; Tachikawa, T.; Zhang, P.; Fujitsuka, M.; Majima, T., Au/TiO₂ superstructure-based plasmonic photocatalysts exhibiting efficient charge separation and unprecedented activity,” *Journal of the American Chemical Society* **2014**, *136*, 458–465.

[115]. Lee, Y. K.; Park, J.; Park, J. Y., The Effect of Dye Molecules and Surface Plasmons in Photoninduced Hot Electron Flows Detected on Au/TiO₂ Nanodiodes. *Journal of Physical Chemistry C* **2012**, *116*, 18591-18596.

- [116]. Lee, Y. K.; Lee, H.; Lee, C.; Hwang, E.; Park, J. Y., Hot-Electron-based Solar Energy Conversion with Metal-Semiconductor Nanodiodes. *Journal of Physics: Condensed Matter* **2016**, *28*, 254006.
- [117]. Lee, C.; Nedrygailov, I. I.; Lee, Y. K.; Ahn, C.; Lee, H.; Jeon, S.; Park, J. Y., Amplification of hot electron flow by the surface plasmon effect on metal-insulator-metal nanodiodes. *Nanotechnology* **2015**, *26*, 445201.
- [118]. Mubeen, S.; Lee, J.; Lee, W.-R.; Singh, N.; Stucky, G. D.; Moskovits, M., On the Plasmonic Photovoltaic. *ACS Nano* **2014**, *8*, 6066-6073.
- [119]. Fang, Y. R.; Jiao, Y.; Xiong, K. L.; Ogier, R.; Yang, Z. J.; Gao, S. W.; Dahlin, A. B.; Kall, M., Plasmon Enhanced Internal Photoemission in Antenna-Spacer-Mirror Based Au/TiO₂ Nanostructures. *Nano Letters* **2015**, *15*, 4059-4065.
- [120]. Li, X. H.; Chou, J. B.; Kwan, W. L.; Elsharif, A. M.; Kim, S. G., Effect of anisotropic electron momentum distribution of surface plasmon on internal photoemission of a Schottky hot carrier device. *Optics Express* **2017**, *25*, A264-A273.
- [121]. Robotjazi, H.; Zhao, H. Q.; Swearer, D. F.; Hogan, N. J.; Zhou, L. N.; Alabastri, A.; McClain, M. J.; Nordlander, P.; Halas, N. J., Plasmon-induced selective carbon dioxide conversion on earth-abundant aluminum-cuprous oxide antenna-reactor nanoparticles. *Nature Communications* **2017**, *8*, 27.

- [122]. Fowler, R. H., The analysis of photoelectric sensitivity curves for clean metals at various temperatures. *Physical Review* **1931**, *38*, 45–56.
- [123]. Lee, Y. K.; Jung, C. H.; Park, J.; Seo, H.; Somorjai, G. A.; Park, J. Y., Surface Plasmon-Driven Hot Electron Flow Probed with Metal-Semiconductor Nanodiodes. *Nano Letters* **2011**, *11*, 4251-4255.
- [124]. Chen, H. M.; Chen, C. K.; Chen, C. J.; Cheng, L. C.; Wu, P. C.; Cheng, B. H.; Ho, Y. Z.; Tseng, M. L.; Hsu, Y. Y.; Chan, T. S.; Lee, J. F.; Liu, R. S.; Tsai, D. P., Plasmon Inducing Effects for Enhanced Photoelectrochemical Water Splitting: X-ray Absorption Approach to Electronic Structures. *ACS Nano* **2012**, *6*, 7362-7372.
- [125]. Chen, C. J.; Chen, C. K.; Lu, T. H.; Hu, S. F.; Liu, R. S., The substitution of the platinum counter electrode in a plasmonic photoelectrochemical system with near-infrared absorption for solar water splitting. *RSC Advances* **2016**, *6*, 103160-103168.
- [126]. Johnson, P. B.; Christy, R. W., Optical Constants of Noble Metals. *Physical Review B* **1972**, *6*, 4370-4379.
- [127]. Rudin, S.; Reinecke, T., Oscillator Model for Vacuum Rabi Splitting in Microcavities. *Physical Review B* **1999**, *59*, 10227.

Chapter 3

***In situ* real-time measurement of biotin-streptavidin binding kinetics by photoelectrochemistry**

3.1 Introduction

The near-field coupling has been proved to be able to enhance the plasmon-induced photocurrent generation in chapter 2, which shows a great potential to realize highly sensitive PEC biosensor by utilizing the near-field coupling effect. The interparticle interaction between two closely spaced nanoparticles is known to induce strong near-field enhancement as introduced in chapter 1. In this chapter, I proposed to develop a highly sensitive PEC biosensor utilizing the near-field coupling between two nanoparticles to detect the binding affinities and kinetics of biotin-STA interaction. The enhanced photocurrent response to different concentrations of streptavidin-modified gold nanoparticles (STA-AuNPs) should be observed due to the near-field coupling between the gold nanoislands (AuNIs) and STA-AuNPs. The AuNIs loaded TiO₂ photoelectrode was prepared and modified by TTB molecules for 2 h. The STA-AuNPs were selected as a model target due to the specific interaction of biotin-STA. The introduced interparticle interaction between AuNPs and AuNIs induced near-field coupling can enhance the photocurrent generation. The photocurrent response to different concentrations of STA-AuNPs will be measured under only visible light, which prevents UV light-induced decomposition of organic molecules. Moreover, direct investigation of the binding kinetics of the biotin-STA association at different concentrations will be analyzed by real-time monitoring of the PEC sensing characteristics. I believe this affinity biosensor can be further utilized to detect and determine the binding affinity and kinetics of other biomolecular interactions such as antibody-antigen^[1,2], DNA-protein^[3,4].

3.2 Experimental details

3.2.1 Gold film preparation and modifications

Two silicon substrates were rinsed with acetone, methanol, and deionized water in an ultrasonic bath for 5 minutes separately and dried by compressed nitrogen. 1 nm Ti adhesion layer and 40 nm Au film were deposited on the surface of silicon substrates by Helicon sputtering (MPS-4000, ULVAC) to form the Au film. The biomolecule modification process is shown in Figure 3.1. A sample was immersed into the TTB solution with a sealed vessel for 2 h at room temperature. The TTB molecules can bind to the surface of AuNIs directly due to the extremely strong Au-S bond.^[5-8] The Au-S bond is very strong with good resistance to acid, alkali, and external forces and good selectivity to prevent interactions with other functional groups. Purchased TTB (HS-(CH₂)₁₁-NH-CO-biotin, ProChimia Co., Gdansk, Poland) solution was prepared by dissolving 5 mg TTB powder into 5 mL 2-propanol solution (ultrasonic bath needed to dissolve the TTB completely). The TTB modified Au film was then rinsed with 2-propanol and deionized water in an ultrasonic bath for 5 minutes separately and dried by compressed nitrogen completely. Same method has been applied to process the STA-AuNPs (98 nM, EM.STP20, BBI, Cardiff, UK) conjugate solution modifications but with 24 h to make sure the biotin-STA combine completely. However, for removing excess STA-AuNPs that do not bound on AuNIs, the biotin-STA association is not strong enough to prevent the broken from ultrasonic bath and high speed compressed nitrogen. Therefore, after STA-AuNPs modification, the sample was cleaned by immersing the sample into deionized water and kindly shaking by hand for 30 seconds. The samples were cleaned thrice to ensure the minimum physical absorption of STA-AuNPs. Another sample had only STA-AuNPs modification directly without TTB modification for control experiment to verify the key role of TTB biotinylation in this series. This experiment was to verify the nonspecific binding of TTB and STA molecules. While some other protein molecules may still bind to Au film

with or without TTB modification, therefore, Bovine Serum Albumin modified AuNPs (BSA-AuNPs, 98 nM, EM.BSA10, BBI, Cardiff, UK) conjugate solution was selected to verify the nonspecific binding of other protein molecules. STA (Jackson ImmunoResearch, PA, USA), which was dissolved in TBS buffer solutions, was also prepared as a control experiment to verify the significant effect of interparticle coupling induced near-field enhancement to increase the photocurrent generation by the introduced AuNPs.

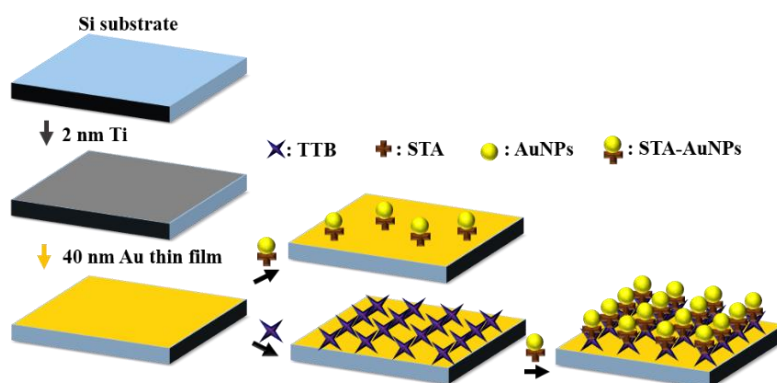


Figure 3.1 Schematic of Au film preparations and two different biomolecule-modified samples. One is modified by STA-AuNPs directly without TTB biotinylation and another one is modified by both TTB and subsequent STA-AuNPs.

3.2.2 Preparation of gold nanoislands decorated titanium dioxide photoelectrode and biomodifications

The AuNIs/TiO₂ photoelectrode was prepared as shown in Figure 3.2. TiO₂ (Rutile, single crystal [001] Crystal Base, 0.05 wt % niobium doped, 10 × 10 × 0.5 mm³), which was purchased from Furuuchi Chemical, was selected as the photoelectrode in this study. The TiO₂ substrate was first rinsed with acetone, methanol, and deionized water in an ultrasonic bath for 5 minutes each and dried with compressed nitrogen. The gold nanoislands-loaded TiO₂ (AuNIs/TiO₂) photoelectrode was fabricated by depositing a 3 nm Au film by helicon sputtering (MPS-4000, ULVAC Co., Ltd.) on the surface of the TiO₂ substrate with subsequent annealing at 800 °C for 1 h under a N₂ atmosphere. The noncontinuous gold film will transform into AuNIs on the surface of TiO₂.

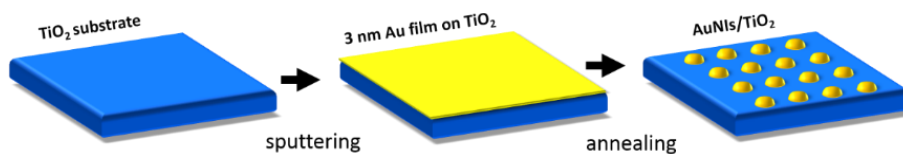


Figure 3.2 Schematic of AuNIs decorated TiO₂ substrate.

Figure 3.3 shows the modification process of AuNIs/TiO₂. The AuNIs/TiO₂ sample was first immersed into a TTB solution in a sealed vessel for 2 h at room temperature. After TTB biomodifications, the TTB immobilized AuNIs/TiO₂ sample was rinsed with 2-propanol and deionized water in an ultrasonic bath for 5 minutes separately and dried by compressed N₂. I employed same method to process the STA/STA-AuNPs modifications but using 24 h to ensure that biotin-STA combine completely. After STA/STA-AuNPs modifications, the samples were cleaned by immersing into deionized water followed by shaking by hand for 30 seconds. The samples were cleaned thrice to ensure minimum physical absorption of the STA/STA-AuNPs. The extinction spectra were measured using a spectrometer (PMA-11, Hamamatsu Photonics) equipped with an optical microscope (BX-51, Olympus) via an optical fiber before and after modifications. The morphologies of the samples before and after modifications were observed by field-emission scanning electron microscopy (FE-SEM, JSM-6700FT, JEOL) with a maximum resolution of 1 nm at an electron acceleration voltage of 15 kV.

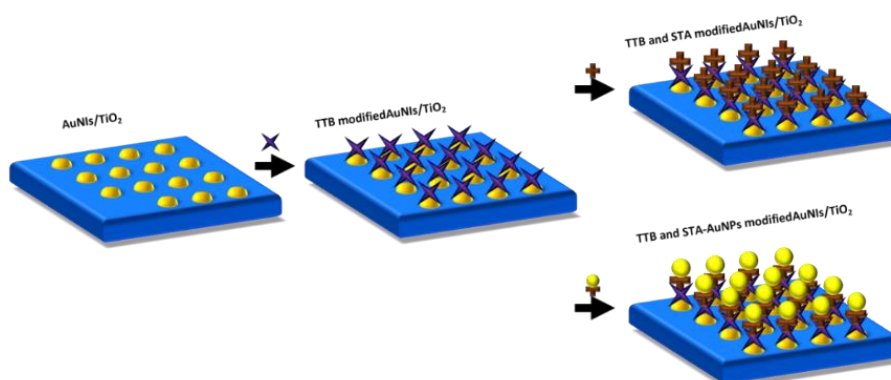


Figure 3.3 Schematic of biomodifications of AuNIs/TiO₂ photoelectrodes.

3.2.3 Photoelectrochemical measurements

The photoelectrochemical measurement was processed the same as shown in chapter 2 for AuNIs/TiO₂ before and after biomolecular modifications. However, special PEC cell needs to be designed for TTB modified AuNIs/TiO₂ photoelectrode to realize *in situ* real-time measurement of STA-AuNPs as shown in Figure 3.4. Different amounts of pristine 98 nM STA-AuNP solution (0.15 μL, 0.15 μL, 0.3 μL, 0.6 μL, 1.2 μL, 2.4 μL, 4.8 μL, 4.8 μL, 4.8 μL, and 4.8 μL) were step-by-step injected into the reaction chamber that was equipped with a TTB-modified AuNIs/TiO₂ electrode and 150 μL of a KClO₄ solution to achieve real-time and *in situ* measurement of the biotin-STA association and binding kinetics. For *in situ* measurement, a platinum wire was employed as a quasi-reference electrode due to the special reaction chamber design (extremely small).

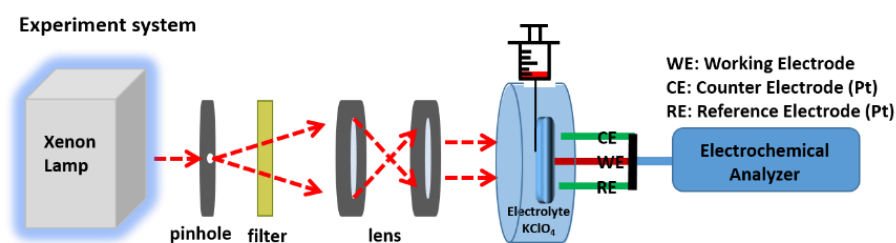


Figure 3.4 The *in situ* real-time PEC measurement. A platinum wire was employed as a quasi-reference electrode.

3.3 Results and discussions

3.3.1 Nonspecific adsorptions

The nonspecific adsorptions will introduce a large error during the real measurement. Therefore, the nonspecific adsorptions were firstly analyzed by immersing the Au film into solution containing other proteins. BSA, which is often used as a protein concentration standard in laboratory experiments, was selected for nonspecific adsorption. The Au film samples with and without TTB modifications were immersed

into BSA-AuNPs solution for 24 h. The SEM images of nonspecific adsorptions of BSA-AuNPs to Au films with and without TTB modifications were shown in Figure 3.5 (a) and (b), respectively. There is no obvious adsorption of BSA-AuNPs both the Au films with and without TTB modifications. This means the nonspecific adsorptions of other protein molecules in my system are negligible.

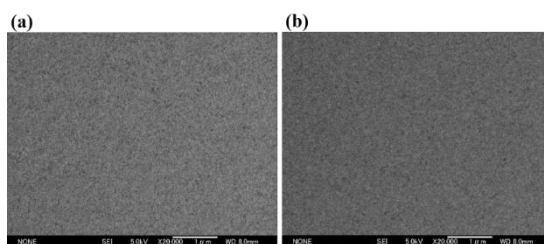


Figure 3.5 SEM images of Au films with only BSA-AuNPs modification (a) and both TTB and BSA-AuNPs modifications (b).

The SEM images of adsorptions of STA-AuNPs on the surface of Au films with and without TTB modifications were shown in Figure 3.6. The density of nonspecific adsorption without TTB modification is $0.5/\mu\text{m}^2$ after calculation as shown in Figure 3.6 (a). The specific adsorption with TTB modification is $150/\mu\text{m}^2$ as shown in Figure 3.6 (b), demonstrating the indispensable significance of biotinylation to adsorb the STA.

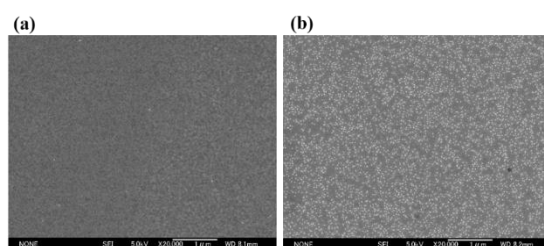


Figure 3.6 SEM images of Au films with only STA-AuNPs modification (a) and both TTB and STA-AuNPs modifications (b). Densities are 0.5 and $150/\mu\text{m}^2$, respectively.

3.3.2 Structural geometries of gold nanoislands decorated titanium dioxide photoelectrode

Figure 3.7 (a) shows the SEM image of AuNIs on TiO₂ surface. The corresponding particle size distributions are shown in Figure 3.7 (b), which is derived from the analysis of Figure 3.7 (a) by ImageJ. The AuNIs have about 18 nm mean diameter with a standard deviation of 8 nm.

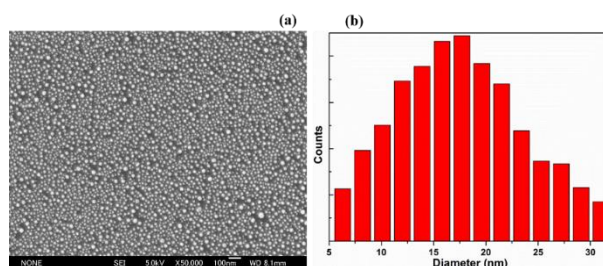


Figure 3.7 The SEM images of AuNIs/TiO₂ and diameters distribution of AuNIs.

3.3.3 Optical properties of gold nanoislands decorated titanium dioxide photoelectrode and streptavidin-modified gold nanoparticles

The extinction spectrum of STA-AuNPs conjugate solution is measured and shown in Figure 3.8. The LSPR peak locates around 530 nm.

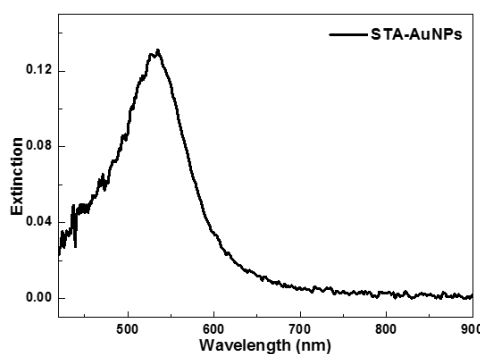


Figure 3.8 The extinction spectrum of STA-AuNPs conjugate solution.

The extinction spectrum of AuNIs/TiO₂ is shown in Figure 3.9. The LSPR peak locates around 600 nm. The sizes of AuNIs and AuNPs are very similar but the AuNIs

shows a longer wavelength of LSPR. This is due to the large refractive index of TiO₂ substrate. Detailed numerical results by FDTD simulations will be shown next.

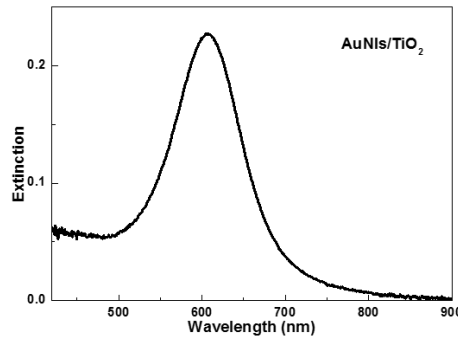


Figure 3.9 The extinction spectrum of AuNIs/TiO₂.

3.3.4 Verification of the plasmon-induced photocurrent generation

To verify that the photocurrent in visible region is induced by surface plasmons, IPCE action spectrum has been measured by Eq. 2.2. The extinction (black) and IPCE (red) action spectra of the AuNIs/TiO₂ photoelectrode have good accordance as shown in Figure 3.10, except a small mismatch in the wavelength region from 450 to 550 nm resulted from the intrinsic light absorption of gold based on the interband electronic excitation from d bands to sp conduction bands. This demonstrates the photocurrent generation deriving from the LSPR. The IPCE action spectrum of bare TiO₂ is not shown here because the photocurrent at visible region is extremely low.

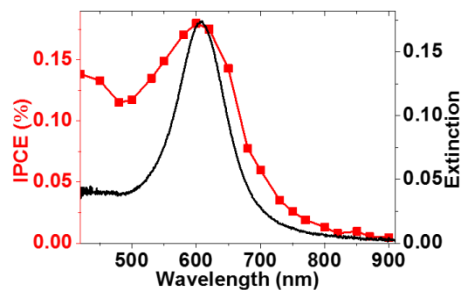


Figure 3.10 Extinction spectrum (black) and IPCE action spectrum (red) of the AuNIs/TiO₂ photoelectrode without modification.

3.3.5 Optical and photoelectrochemical measurements before and after biomolecular modifications

3.3.5.1 Streptavidin modification

Figure 3.11 shows the extinction spectra change before (green) and after (red) TTB and subsequent STA modifications (black), respectively. The LSPR peak showed a redshift, and the extinction intensity enhanced after TTB and STA modifications, demonstrating the successful bindings between AuNIs and TTB, and TTB and STA.

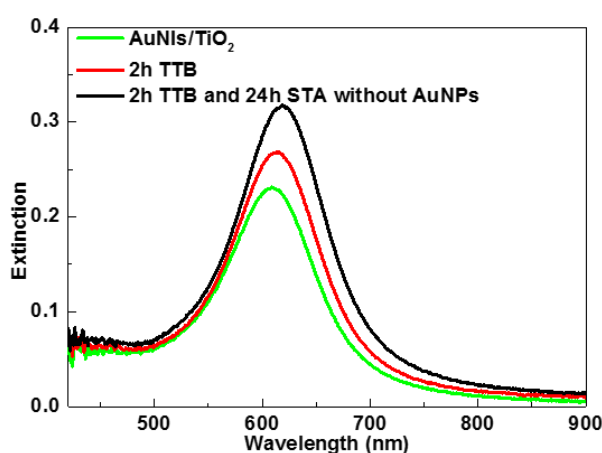


Figure 3.11 The extinction spectra evolutions of the AuNIs/TiO₂ photoelectrode before modification (green), after TTB modification (red) and STA modification (black), respectively.

Figure 3.12 shows the *I-t* curves (a) with irradiation of monochromatic light at 600 nm (LSPR region) and the corresponding IPCE action spectra (b) before (green) and after (red) TTB with subsequent STA modifications (black), respectively. The photocurrent weakened after TTB and subsequent STA modifications, which suggests that the TTB and STA molecules may prevent the water molecules from acting as electron donors. In comparison with TTB modification alone, the STA seems not so large effect to the photocurrent generation. So the TTB modified AuNIs/TiO₂ photoelectrode seems not so sensitive to measure the STA.

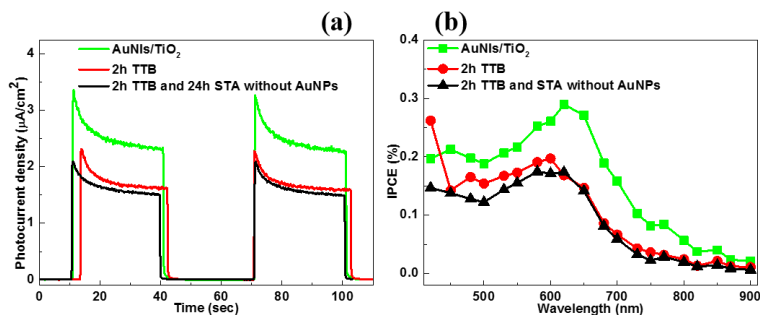


Figure 3.12 (a) The photocurrent response change under irradiation of monochromatic light at 600 nm before modification (green), after TTB modification (red) and STA modification (black), respectively. (b) The corresponding IPCE action spectral evolution of the AuNIs/TiO₂ photoelectrode.

3.3.5.2 Streptavidin-modified gold nanoparticles modification

Here I introduce STA-AuNPs to replace STA due to the strong interparticle coupling induced optical near-field enhancement. Figure 3.13 shows the extinction spectra evolutions before (green) and after (red) TTB and subsequent STA-AuNPs modifications (black), respectively. The LSPR peak also showed a redshift, and the extinction intensity enhanced after TTB and STA-AuNPs modifications, demonstrating the successful bindings between AuNIs and TTB, and TTB and STA-AuNPs. One notable point is that the redshift and intensity enhancement of LSPR peak after STA-AuNPs modification are larger than STA alone.

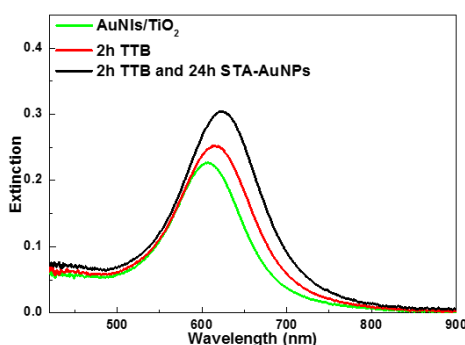


Figure 3.13 The extinction spectra evolution of the AuNIs/TiO₂ photoelectrode before modification (green), after TTB modification (red) and STA-AuNPs modification (black).

Figure 3.14 shows the *I-t* curves with irradiation of monochromatic light at 600 nm (LSPR region) of TiO₂ (blue), AuNIs/TiO₂ (green) and after TTB (red) and STA-AuNPs (black) modifications. The photocurrent of AuNIs/TiO₂ is more than 100 times larger than that of only TiO₂ without AuNIs, demonstrating the significance of plasmonically near-field induced hot electron transfer and photocurrent generation. The photocurrent was decreased after the TTB modification. However, the photocurrent was increased after both TTB and STA-AuNPs modifications. The result indicated that the photoactivity of the electrode was enhanced after modification of STA-AuNPs due to the interparticle interactions between AuNIs and AuNPs. This made the TTB modified AuNIs/TiO₂ photoelectrode possible to be utilized to detect different concentrations of STA-AuNPs.

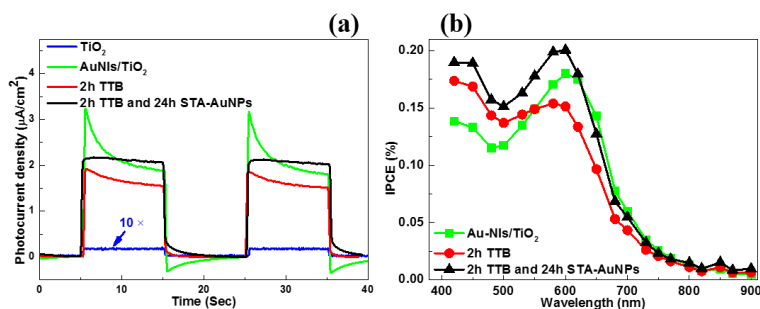


Figure 3.14 (a) The photocurrent response under irradiation with 600 nm monochromatic light of TiO₂ (blue), AuNIs/TiO₂ photoelectrode (green), after TTB modification (red) and subsequent STA-AuNPs modification (black). (b) The corresponding IPCE action spectral evolutions of the AuNIs/TiO₂ photoelectrode before and after various biomodifications.

3.3.6 *In situ* real-time measurement of streptavidin-modified gold nanoparticles

As shown in Figure 3.15 (a), a stepwise increase in the photocurrent response was observed under irradiation of 600 nm light after each continuous injection of STA-AuNPs. One notable point is that there is sudden drop of the photocurrent response

during the injection timing (only few seconds). This is due to the special design of extremely small reaction chamber and a portion of the light is inevitably blocked by the needle of the microsyringe. The sudden drops in all the injection time were related to be depicted by a clearer representation and accurate analysis. The photocurrent finally reaches saturation at around 8 nM of STA-AuNPs, indicating that almost all the binding sites of TTB were nearly occupied by STA-AuNPs. The normalized photocurrent enhancement as a function of different concentrations of STA-AuNP is shown in Figure 3.15 (b). The normalized photocurrent enhancement at each concentration was calculated by $\Delta i/\Delta i_{max}$, where Δi and Δi_{max} are the photocurrent increase at the concentration and the maximum value of the photocurrent increase, respectively.

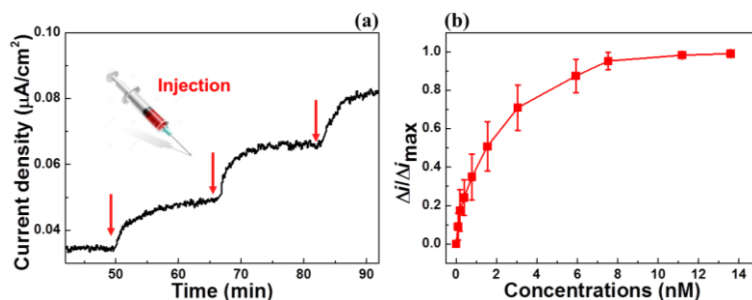


Figure 3.15 (a) Representative *in situ* real-time photocurrent response to different concentrations of STA-AuNP under irradiation with only 600 nm monochromatic light. (b) Normalized photocurrent enhancement as a function of different concentrations of STA-AuNP. The error bars indicate the standard deviation of five replicate measurements.

3.3.7 Proposed mechanism

The corresponding SEM images after modification with different concentrations of STA-AuNPs and the proposed schematic diagrams are shown in Figure 3.16. In comparison with only AuNIs as shown in Figure 3.16 (a), one-to-one bindings between TTB-AuNIs and STA-AuNPs were predominately observed at a STA-AuNPs concentration of 0.98 nM as shown in Figure 3.16 (b). Moreover, multi-STA-AuNPs

binding to one AuNI seems to be limited and rarely observed. However, at a STA-AuNPs concentration of 2.9 nM, multi-STA-AuNPs binding to one AuNI increased as shown in Figure 3.16 (c). The proposed mechanism can be summarized due to the results and described below. For the original AuNIs/TiO₂ photoelectrode, the LSPR-induced charge separation will be activated under visible light irradiation due to the plasmon-induced hot electron transfer. In this case, the water molecules act as electron donors, and the electrons from the AuNIs inject to the conduction band of TiO₂. After TTB modification, the AuNI surface was covered by layers of TTB molecules and the TTB molecules may prevent the water molecules from acting as electron donors for photocurrent generation. Therefore, the photocurrent decreases. The binding between TTB-AuNIs and STA-AuNPs primarily occurs in a one-to-one fashion at lower concentration region of STA-AuNPs modification and the photocurrent generation is enhanced by the introduced strong interparticle interactions between AuNPs and AuNIs. For the higher concentration region, multi-STA-AuNPs connect to one AuNI. When the bindings between TTB-AuNIs and STA-AuNPs reach a maximum, the photocurrent becomes saturated.

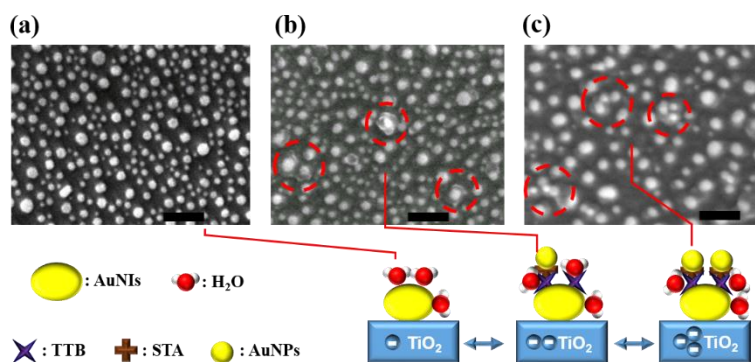


Figure 3.16. SEM images of AuNIs/TiO₂ photoelectrode without modification (a) and after TTB modification and subsequent 0.98 nM (b) and 2.9 nM (c) STA-AuNPs modifications. The scale bars represent 100 nm. The schematic diagrams show the proposed mechanism of binding modes that corresponds to the SEM image. The SEM images were processed by GIMP software (<https://www.gimp.org/>) to get greater

clarity and resolution because the original SEM images were blurred due to the organic molecules.

To verify the binding modes between AuNIs and AuNPs at various concentrations, the pristine STA-AuNPs solution with 98 nM concentration was utilized to modify the TTB-AuNIs/TiO₂. The SEM images of only AuNIs without and with 98 nM STA-AuNPs modifications are shown in Figure 3.17 (a) and Figure 3.17 (b), respectively. Figure 3.18 (b) shows lots of examples of multi-STA-AuNPs binding to one AuNI. Figure 3.17 (c) and Figure 3.17 (d) show the diameter distribution change. The apparent diameter increased a lot after STA-AuNPs modification due to the multi-STA-AuNPs bindings.

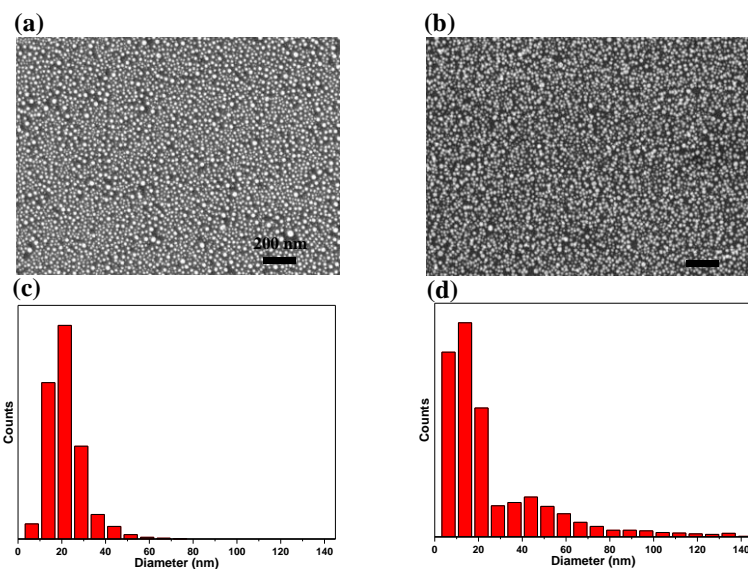
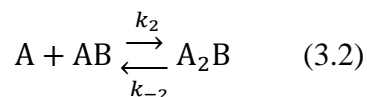
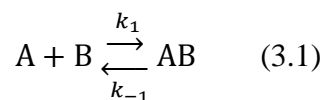


Figure 3.17. SEM images of only AuNIs without modification (a), after TTB and subsequent 98 nM STA-AuNPs modifications (b). (c) and (d) shows the corresponding diameters distributions of (a) and (b), respectively. The SEM images were processed by GIMP software (<https://www.gimp.org/>) to get greater clarity and resolution.

3.3.8 Binding kinetics analysis

A time-dependent model that represents the binding kinetics between TTB-AuNIs and STA-AuNPs was shown below:



where A, B, AB and A₂B represent the STA-AuNPs, TTB-AuNIs, newly formed complex at the first binding step (one STA-AuNP to one TTB-AuNI) and the complex second binding step (two STA-AuNPs to one TTB-AuNI), respectively. The relationship between the photocurrent enhancement and the newly formed AB and A₂B was assumed to be:

$$\Delta i = \alpha[AB] + \beta[A_2B] \quad (3.3)$$

where Δi is the photocurrent enhancement, α and β represent the contributions to the photocurrent enhancement of newly formed AB and A₂B, respectively, and [AB] and [A₂B] represent the concentrations of AB and A₂B, respectively. The coupled differential equations arising from Eqs. (3.1) and (3.2) were solved numerically using the SimFit software. The initial concentrations of A and B need to be known at each injection. The concentration of A can be easily known and calculated from the specification of STA-AuNPs. The density of B can be calculated from Figure 3.17 (a) to be 1520 particles / μm^2 .

During *in situ* photocurrent measurement, the TTB-AuNIs/TiO₂ working electrode was covered with an O-ring having a circular window with a diameter of 6 mm to permit the light irradiation.

The active number of B is: $1520 \times 3.14 \times 3000 \times 3000 = 4.3 \times 10^{10}$.

Therefore, the initial concentration of B is: $(4.3 \times 10^{10})/(6.02 \times 10^{23})/150 \mu\text{L} = 4.76 \times 10^{-10}$ M. The initial concentrations of the next injection are equal to the final concentrations of the previous injection for B, AB, A₂B and Δi. However, it is different for A due to the successive injection of A. The initial concentration of A of the next injection is determined by the addition of previous left A and the newly injected A.

Here shows the detailed for SimFit:

When using Simfit to simulate the signal change, y(1), y(2), y(3), y(4), y(5), p1, p2, p3, p4, p5 and p6 were defined as B, AB, A₂B, Δi, A, k1, k-1, k2, k-2, α and β, respectively. y(1), y(2), y(3), y(4) and y(5) should be the functions of time (x). From Eqs. 3.1, 3.2 and 3.3, the following coupled differential equations can be obtained:

$$dy(1)/dx = - p(1)y(1)y(5) + p(2)y(2);$$

$$dy(2)/dx = p(1)y(1)y(5) - [p(2)+p(3)y(5)]y(2) + p(4)y(3);$$

$$dy(3)/dx = p(3)y(2)y(5) - p(4)y(3);$$

$$dy(4)/dx = p(5)*(p(1)y(1)y(5) - [p(2)+p(3)y(5)]y(2) + p(4)y(3)) + p(6)*(p(3)y(2)y(5) - p(4)y(3));$$

$$dy(5)/dx = - p(1)y(1)y(5) + p(2)y(2) - p(3)y(5)y(2) + p(4)y(3).$$

The related jacobian:

$$j(1) = df(1)/dy(1) = - p(1)y(5);$$

$$j(2) = df(2)/dy(2) = - (p(2) + p(3)y(5));$$

$$j(3) = df(3)/dy(3) = - p(4);$$

$$j(4) = df(4)/dy(4) = 0;$$

$$j(5) = df(5)/dy(5) = - p(1)y(1) - p(3)y(2).$$

During the fitting process, the values of p1, p2, p3, p4, p5 and p6 are set to be in the range from low-limit to high-limit of $0 \sim 1 \times 10^{11}$, $0 \sim 1$, $0 \sim 1 \times 10^{11}$, $0 \sim 1$, $0 \sim 1 \times 10^{11}$, $0 \sim 1 \times 10^{11}$, respectively.

The experimental (red) and simulated (black) photocurrents as a function of time at different concentrations of STA-AuNPs are shown in Figure 3.18 (a), however, a few points at high concentration region are unavailable due to a lack of enhancement and not shown here. The experimental and simulated results are in good agreement. The corresponding evolutions of the reactant (B, red) and products (AB, blue and A₂B, black) at different concentrations of A are shown in Figure 3.18 (b), the evolution of A is not shown due to the successive injections. As shown in Figure 3.18 (b), for the first four concentrations of A (98.6 pM, 197 pM, 393 pM and 782 pM), the formation of AB product is predominately, and the A₂B product formation is negligibly small. One notable point is that AB always increases during each injection. The result demonstrates that the binding between TTB-AuNIs and STA-AuNPs was nearly one-to-one binding in the lower concentration region. However, for the last two concentrations (1.55 nM and 3.06 nM), the A₂B product increases to the same order as AB, demonstrating that binding between multi-STA-AuNPs and one AuNI is a competitive one-to-one binding in the higher concentration region. Moreover, AB increases at first and then decreases during each injection. These results are in good agreement with the SEM measurement and confirm my hypothesis (Figure 3.16).

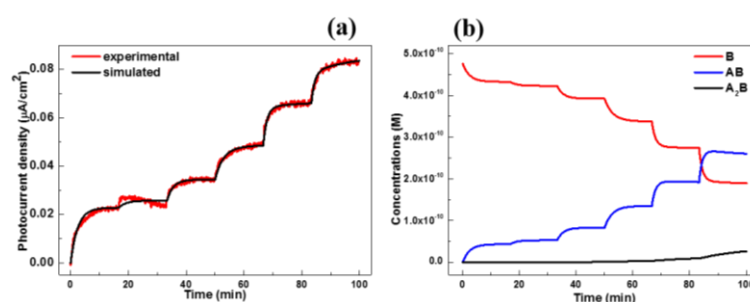


Figure 3.18 (a) Experimental and simulated photocurrents as a function of time at different concentrations of STA-AuNP. (b) The simulated evolutions of B, AB, and A₂B as a function of time at different concentrations of STA-AuNP.

The association and dissociation rate constants and other related kinetic parameters at different concentrations of STA-AuNP are shown in Table 2.1. The association rate constant of the first binding step (k_1) was two orders larger than that of the second binding step (k_2). There is one possible reason that the binding of the second STA-AuNP was retarded by steric hindrance due to initial binding between STA-AuNPs and TTB-AuNIs.^[133] It is important to note that both of the association rate constants of two binding steps, k_1 and k_2 exhibit a small concentration dependence on STA-AuNPs. This phenomenon is also a result of the steric hindrance of the STA-AuNP bound to the adjacent TTB-AuNI. The relative thermodynamic binding constants of two binding steps can be calculated as follows: $K_{a, surf1} = k_1/k_{-1} = (7.67 \pm 0.73) \times 10^8 \text{ M}^{-1}$, $K_{a, surf2} = k_2/k_{-2} = (5.54 \pm 0.14) \times 10^7 \text{ M}^{-1}$, and these values are smaller than that reported for biotin-STA association ($1 \times 10^{11} \text{ M}^{-1}$)^[5] but larger than another reported value $3 \times 10^6 \text{ M}^{-1}$.^[10] This demonstrates that my new analytical model is meaningful to determinate the binding affinities of specific binding molecules.

Table 2.1. Association and dissociation rate constants and related kinetic parameters at different concentrations of STA-AuNPs.

Concentration of STA-AuNPs (M)	9.86×10^{-11}	1.97×10^{-10}	3.93×10^{-10}	7.82×10^{-10}	1.553×10^{-9}	3.057×10^{-9}	Average
$k_1 (\text{M}^{-1}\text{s}^{-1})$	6.43×10^6	4.11×10^6	3.60×10^6	2.29×10^6	3.68×10^6	3.00×10^6	$(3.85 \pm 1.41) \times 10^6$
$k_{-1} (\text{s}^{-1})$	3.51×10^{-3}	4.70×10^{-3}	5.24×10^{-3}	3.65×10^{-3}	7.03×10^{-3}	5.96×10^{-3}	$(5.02 \pm 1.36) \times 10^{-3}$
$k_2 (\text{M}^{-1}\text{s}^{-1})$	5.42×10^4	5.42×10^4	5.42×10^4	5.91×10^4	5.13×10^4	5.09×10^4	$(5.40 \pm 0.29) \times 10^4$
$k_{-2} (\text{s}^{-1})$	9.75×10^{-4}	9.75×10^{-4}	9.75×10^{-4}	9.25×10^{-4}	9.99×10^{-4}	1.00×10^{-3}	$(9.75 \pm 0.27) \times 10^{-4}$
α	5.23×10^8	3.01×10^8	2.85×10^8	2.47×10^8	2.64×10^8	1.66×10^8	$(2.98 \pm 1.20) \times 10^8$
β	4.09×10^8	4.08×10^8	4.08×10^8	4.50×10^8	3.82×10^8	3.75×10^8	$(4.05 \pm 0.26) \times 10^8$

3.3.9 Interparticle coupling and near-field enhancement

The far-field extinction and near-field enhancement properties of AuNIs/TiO₂ system before and after TTB and STA-AuNPs modifications were calculated using the FDTD simulations. Figure 3.19 shows the schematic of FDTD simulation. The thicknesses of TTB and STA are assumed to be 0.5 and 1.5 nm as reported by Jung,^[11] respectively.

The refractive indexes of TTB and STA are assumed to be 1.45 as reported by Laborde et al.^[12] and Busse et al.,^[13] respectively. The optical constants of Au were obtained using the data from Johnson and Christy.^[14] A discrete, uniformly spaced mesh with a mesh size of 0.2 nm was performed during the FDTD simulations. The plane wave light source was injected onto AuNIs/TiO₂ structures from the structure side at normal incidence. The extinction spectra were obtained by a transmission power monitor below the TiO₂ surface. One power and profile monitor was performed and located on the interface of the AuNIs and TiO₂ (xy plane), another one was located at the gap between AuNIs and AuNPs (xz plane) to explore the near-field enhancement.

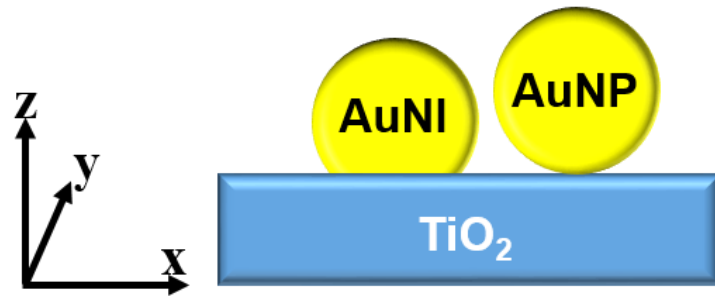


Figure 3.19 The schematic of FDTD simulation.

Figure 3.20 shows the calculated extinction spectra of AuNIs/TiO₂ before and after TTB, STA and AuNPs modifications. The resonance wavelength has a redshift and the extinction value increases after biomodification, which agrees well with the experimental data as shown in Figure 3.11 and 3.13.

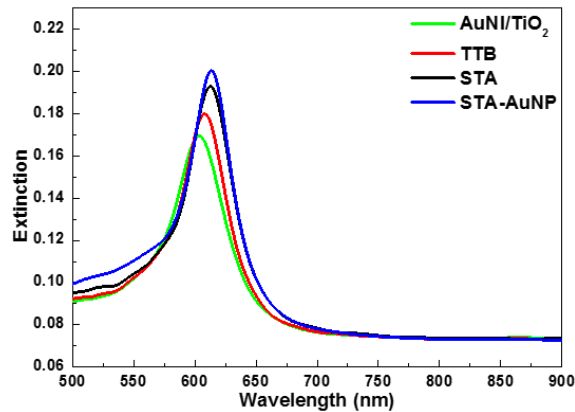


Figure 3.20 The calculated extinction spectra of AuNI/TiO₂ (green), after TTB (red), STA (black) and AuNPs (blue) modifications.

The plasmon-induced photocurrent generation deriving from water oxidation is relative to the near-field enhancement. To confirm the enhanced photocurrent generation, the electric field enhancement and distributions of AuNIs/TiO₂ at 600 nm wavelength of only AuNI, after TTB, STA and AuNP modifications are recorded and shown in Figure 3.21. There is no electric field enhancement after TTB and STA modifications. However, extremely large electric field enhancement can be observed after the binding of AuNPs especially at the gap between AuNI and AuNP. This demonstrates the significant effect of interparticle coupling induced near-field enhancement for the increased photocurrent generation.

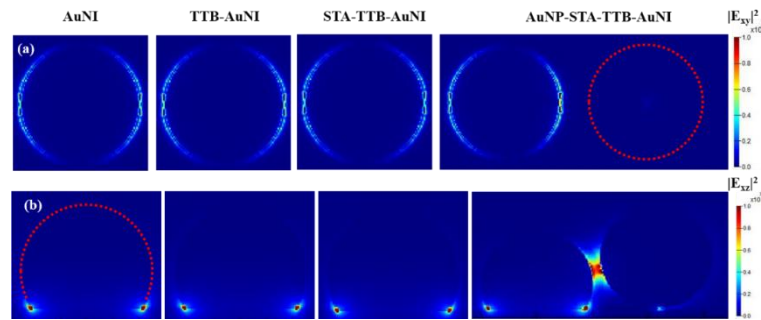


Figure 3.21. The electric field intensity distributions of AuNI, after TTB, STA and AuNP biomodifications at 600 nm in xy plane ($|E_{xy}|^2$) (a) and xz plane ($|E_{xz}|^2$) (b), respectively.

3.4 Conclusions

In this chapter, a surface plasmon-induced visible light-activated PEC biosensor using a TTB-modified AuNIs/TiO₂ photoelectrode for *in situ* real-time measurement of the biotin-STA binding kinetics by near-field coupling has been successfully developed. The interparticle interactions between the AuNIs and the introduced AuNPs enhanced the near-field and subsequent photocurrent generation. Good concentration dependence of the photocurrent response was observed under irradiation with 600 nm monochromatic light with high sensitivity, which prevents UV light-induced decomposition of organic molecules (i.e., both the receptors and targets). Moreover, direct investigation of the binding kinetics of the biotin-STA association can be achieved by real-time monitoring of the PEC sensing characteristics. The stepwise binding model between STA-AuNPs and TTB-AuNIs is consistent with the experimental results. The surface-confined thermodynamic binding constant can be calculated. The proposed biosensor based on plasmon-induced photocurrent generation is useful for both thermodynamic and kinetic analyses of various biomolecular interactions and expected to allow the miniaturization. This method opens a new avenue for the specific electrical detection of biomolecular interactions and real-time binding kinetic measurements.

3.5 References

- [1]. A. J. Haes, L. Chang, W. L. Klein, R. P. Van Duyne, Detection of a biomarker for Alzheimer's disease from synthetic and clinical samples using a nanoscale optical biosensor. *Journal of the American Chemical Society* **2005**, *127*, 2264–2271.
- [2]. K. M. Mayer, S. Lee, H. Liao, B. C. Rostro, A. Fuentes, P. T. Scully, C. L. Nehl, J. H. Hafner, A label-free immunoassay based upon localized surface plasmon resonance of gold nanorods. *ACS Nano* **2008**, *4*, 687–692.
- [3]. Y. L. Zhou, Z. N. Xu, M. Wang, B. Sun, H. S. Yin, S. Y. Ai, DNA methyltransferase activity assay based on visible light-activated photoelectrochemical biosensor. *Biosensors and Bioelectronics* **2014**, *53*, 263–267.
- [4]. W. W. Zhao, J. J. Xu, H. Y. Chen, Photoelectrochemical DNA biosensors. *Chemical Reviews* **2014**, *114*, 7421–7441.
- [5]. R. G. Nuzzo, B. R. Zegarski, L. H. Dubois, Fundamental studies of the chemisorption of organosulfur compounds on Au (111). Implications for molecular self-assembly on gold surfaces. *Journal of the American Chemical Society* **1987**, *109*, 733–740.
- [6]. C. D. Bain, E. B. Troughton, Y. T. Tao, J. Evall, G. M. Whitesides, R. G. Nuzzo, Formation of monolayer films by the spontaneous assembly of organic thiols from solution onto gold. *Journal of the American Chemical Society* **1989**, *111*, 321–335.
- [7]. H. Sellers, A. Ulman, Y. Shnidman, E. E. James, Structure and binding of alkanethiolates on gold and silver surfaces: implications for self-assembled monolayers. *Journal of the American Chemical Society* **1993**, *115*, 9389–9401.
- [8]. M. Brust, M. Walker, D. Bethell, D. J. Schiffrin, R. Whyman, Synthesis of thiol-derivatised gold nanoparticles in a two-phase liquid-liquid system. *Journal of the Chemical Society, Chemical Communications* **1994**, 801–802.

- [9]. T. Buranda, G. M. Jones, J. P. Nolan, J. Keij, G. P. Lopez, L. A. Sklar, Ligand receptor dynamics at streptavidin-coated particle surfaces: a flow cytometric and spectrofluorimetric study. *Journal of Physical Chemistry C* **1999**, *103*, 3399–3410.
- [10]. T. Arai, P. K. R. Kumar, C. Rockstuhl, K. Awazu, J. Tominaga, An optical biosensor based on localized surface plasmon resonance of silver nanostructured films. *Journal of Optics A: Pure and Applied Optics* **2007**, *9*, 699–703.
- [11]. Bong-Su Jung. Fabrication and Characterization of a Plasmonic Biosensor Using NonSpherical Metal Nanoparticles.
- [12]. H.M. Laborde, A.M.N. Lima, F.C.C.L. Loureiro, C. Thirstrup, H. Neff. Adsorption, kinetics and biochemical interaction of biotin at the gold–water interface. *Thin Solid Films* **2013**, *540*, 221-226.
- [13]. Busse, S. Scheumann, V. Menges, B. Mittler, S, Sensitivity studies for specific binding reactions using the biotin/streptavidin system by evanescent optical methods. *Biosensors and Bioelectronics* **2002**, *17*, 704–710.
- [14]. Johnson, P. B.; Christy, R. W. Optical Constants of Noble Metals. *Physical Review B* **1972**, *6*, 4370-4379.

Chapter 4

Summary and Future Perspectives

4.1 Summary

In this thesis, plasmon-induced photocurrent generation was pursued as an effective approach to explore the near-field properties of strongly coupled waveguide-plasmon modes. Periodic Au-NGs/TiO₂ structures, which can support both waveguide and plasmon modes and induce strong coupling of waveguide-LSPR modes with a large splitting energy of approximate 250 meV, were fabricated and utilized as photoelectrodes to measure the photocurrent generation. Moreover, under tuning and detuning conditions by changing the pitch size, it was clearly elucidated that the near-field coupling reflects the PEC response. Based on the near-field coupling enhanced photocurrent generation, a surface plasmon-induced visible light-activated PEC biosensor using a TTB-modified AuNIs/TiO₂ photoelectrode for *in situ* real-time measurement of the biotin-STA binding kinetics has been successfully developed. The interparticle interactions between the AuNIs and the introduced AuNPs enhanced the near-field and subsequent photocurrent generation. Good concentration dependence of the photocurrent response was observed under irradiation with 600 nm monochromatic light with high sensitivity, which prevents UV light-induced decomposition of organic molecules (i.e., both the receptors and targets). Moreover, direct investigation of the binding kinetics of the biotin-STA association can be achieved by real-time monitoring of the PEC sensing characteristics. The stepwise binding model between STA-AuNPs and TTB-AuNIs is consistent with the experimental results. The surface-confined thermodynamic binding constant can be calculated. The proposed biosensor based on plasmon-induced photocurrent generation is useful for both thermodynamic and kinetic analyses of various biomolecular interactions and expected to allow the miniaturization.

4.2 Future Perspectives

On the basis of the results obtained in present study, the plasmon-induced photocurrent generation is verified to be corresponding to the near-field coupling of Au nanostructured TiO₂ photoelectrodes. A highly sensitive PEC biosensor by utilizing near-field coupling enhanced photocurrent generation due to the interparticle interaction of AuNIs and AuNPs on TiO₂ photoelectrodes has been successively fabricated. Although such kind of PEC biosensors is able to measure the biotin-STA binding kinetics in real-time, some improvements are still demanded. Perspective outlook should be extended to:

(1) Higher sensitivity and lower detection limit: The near-field coupling has been proved to be able to increase the sensitivity of plasmonic PEC biosensor. Various coupled plasmonic systems show strong near-field coupling, therefore, higher sensitivity and lower detection limit are expected in the future by introducing plasmonic system with strong EM enhancement induced by near-field coupling.

(2) Label free detection: In this thesis, the TTB modified AuNIs/TiO₂ photoelectrodes are used to bind the analyte of AuNPs-labeled streptavidin to introduce near-field coupling. However, label-free detection is very important in clinical diagnostic. If the plasmonic PEC biosensor can bind the analyte without any label and induce near-field coupling between the analyte and metallic nanoparticles, high sensitivity and lower detection limit are also expected and such kind of PEC biosensor is promising for practical application.

(3) Integration and miniaturization: The plasmonic PEC biosensor reported in this thesis is only analyzed in laboratory. The light source and PEC analyzer are still demanded. Integration and miniaturization of such PEC biosensor to achieve compact and small biosensor chip are highly expected.

(4) Extended application: The PEC biosensor induced by near-field coupling enhanced photocurrent has been proved to be able to analyze the binding kinetics of biotin-streptavidin. However, biotin-streptavidin interaction has been explored for

many years. The association and dissociation rate constants have been known well. Incomputable biomolecular interactions exist in nature, such kind of PEC biosensor has the potential to be utilized to explore the binding affinity and kinetics of some other uncertain biomolecular interactions.

Biosensors have big markets and lots of institutions have developed new biosensors with highly accurate, sensitive, pain-free diagnostics. These biosensor developments have resulted in increasing adoption of biosensors into the health, environmental, process industry, and biodefense application markets. The author believes that the plasmonic PEC biosensors are expected to give important information for this research fields.

Acknowledgements

Studied abroad was really an unforgettable experience in my life. Firstly, I would like to express the sincere appreciation to my supervisor, Prof. Hiroaki Misawa, who guided me a lot in science. Thanks for all meaningful discussions when I met difficulties. He taught me not only how to do science but also the positive attitude to face and solve difficulties and problems. This is of great importance to me to do research. I would also like to thanks to Prof. Kosei Ueno for his meaningful advice to my research and presentation. His careful revisions and useful skills of how to prepare, write, and improve papers and presentations. I would also like to thank Prof. Tomoya Oshikiri. He helped me so much during my PHD period. When I met some problems that I cannot solve by myself, he always gave me the best advice. His attitude and passing for scientific research give me the deepest impression on my mind, which I think is the strongest weapon to scale the heights of science. I also appreciate to Prof. Quan Sun, who worked the longest time in Japan and helped every Chinese that been in Japan. And my great thanks to Prof. Xu Shi, who taught and guided me so much in the photoelectrochemistry field. Thanks again for their guidance. It is really a so unbelievable experience to work together with them in comparison with the research in China. That is also my motivation and purpose to study in Japan, now I accomplish my dream. I will be always thankful to my previous supervisor, Prof. Hongbo Sun. He guided me to know what is scientific research, how to find the interest of research, how to deal with the research. I still remember his advices when we met for the first time. He recommended me to apply for the doctoral program in Hokkaido University. I learned a lot from him.

I am also very grateful to Ms. Yumiko Yamaguchi, Ms. Yukiko Sugawara, Ms. Keiko Anzai and Ms. Rumiko Kobayashi, who gave me lots of help for application procedures. I would also thanks to Dr. Yuqing Zhong. When I first came to my laboratory, I studied carbon dioxide fixation, which is very similar to his research of water splitting. Every meaningful discussion and experiment that he showed me tell me

the magic of research. I would also express my special thanks to Dr. Olivier Lecarme, I learned the fabrication technique of aluminum nanostructures from him and he taught me the whole process step-by-step very carefully. He is really an outstanding scientific researcher. We share our new idea to research. Special thanks should go to Dr. Han Yu. When I first came to Japan, I knew nothing about the life in Japan, while Dr. Han Yu helped me so much not only in experiment but also in daily life. I would also thanks to Mr. Xiaolong Yang, we always drunk and relaxed together after busy research. Many thanks to Mr. Jinghuan Yang, who gave me useful advice for simulation.

I would also like to express gratitude to Dr. Hiyori Uehara, Dr. Jie Li, Mr. Hanfa song, Ms. Yanfeng Cao, Ms. Xiaoqian Zang, Dr. Qidai Chen, Dr. Shuyan Gao, Dr. Kuang-Li Lee, Dr. Asuka Maruyama, Dr. Ahamed Shalan, Ms. Yuko Mori, Ms. Wakako Nakano, Ms. Hiroko Itoh, Mr. Yuki Matsuzuka, Mr. Yoshiomi Kamata, Mr. Takaya Tokiwa, Mr. Sho Nozawa, Mr. Keisuke Nakamura, Mr. Hiroki Sawayanagi, Ms. Ririka Masunaga, Mr. Ryohei Takakura, Mr. Tsuyoshi Mikami, Mr. Yamashita Shohei, Ms. Hana Nakamura, Mr. Mr. Hiroaki Yamada, Akira Murayama, Mr. Haruki Jo, Mr. Fuki Shimizu and Mr. Ryota Tatsumi. Thank you all guys that make my life here not boring.

I would also like to thanks to China Scholarship Council (CSC) and Japanese Government (MEXT) Scholarship to make me concentrate my research.

Finally, my deepest gratitude goes to my parents and sister for their support. Actually, my mother did not like me to study abroad but she understands me and let me do what I want. Also my love to my girlfriend, you always stand behind me. The luckiest thing is to meet you in Japan, thank you.

List of Publications

1. **J. Guo**, K. Ueno, J. Yang, X. Shi, J. Li, Q. Sun, T. Oshikiri, H. Misawa,
“Exploring the Near-Field of Strongly Coupled Waveguide-Plasmon Modes by
Plasmon-Induced Photocurrent Generation Using a Gold Nanograting-Loaded
Titanium Dioxide Photoelectrode”
J. Phys. Chem. C **2017**, 121, 21627-21633.
2. **J. Guo**, T. Oshikiri, K. Ueno, X. Shi, H. Misawa,
“Plasmon-Induced Photoelectrochemical Biosensor for *in situ* Real-Time
Measurement of Biotin-Streptavidin Binding Kinetics under Visible Light
Irradiation” Anal. Chim. Acta, **2017**, 957, 70–75.
3. J. Li, K. Ueno, H. Uehara, **J. Guo**, T. Oshikiri, H. Misawa,
“Dual Strong Couplings Between TPPS J-Aggregates and Aluminum Plasmonic
States”
J. Phys. Chem. Lett. **2016**, 7, 2786–2791.